Tests of general relativity with binary black holes from the second LIGO-Virgo gravitational-wave transient catalog

R. Abbott *et al.*[*]

(LIGO Scientific Collaboration and Virgo Collaboration)

Gravitational waves enable tests of general relativity in the highly dynamical and strong-field regime. Using events detected by LIGO-Virgo up to 1 October 2019, we evaluate the consistency of the data with predictions from the theory. We first establish that residuals from the best-fit waveform are consistent with detector noise, and that the low- and high-frequency parts of the signals are in agreement. We then consider parametrized modifications to the waveform by varying post-Newtonian and phenomenological coefficients, improving past constraints by factors of ~ 2; we also find consistency with Kerr black holes when we specifically target signatures of the spin-induced quadrupole moment. Looking for gravitational-wave dispersion, we tighten constraints on Lorentz-violating coefficients by a factor of ~ 2.6 and bound the mass of the graviton to $m_g \leq 1.76 \times 10^{-23}$ eV/c^2 with 90% credibility. We also analyze the properties of the merger remnants by measuring ringdown frequencies and damping times, constraining fractional deviations away from the Kerr frequency to $\delta \hat{f}_{220} = 0.03^{+0.38}_{-0.35}$ for the fundamental quadrupolar mode, and $\delta \hat{f}_{221} = 0.04^{+0.27}_{-0.32}$ for the first overtone; additionally, we find no evidence for postmerger echoes. Finally, we determine that our data are consistent with tensorial polarizations through a template-independent method. When possible, we assess the validity of general relativity based on collections of events analyzed jointly. We find no evidence for new physics beyond general relativity, for black hole mimickers, or for any unaccounted systematics.

I. INTRODUCTION

General relativity (GR) remains our most accurate theory of gravity, having withstood many experimental tests in the Solar System [1] as well as binary pulsar [1,2], cosmological [3,4] and gravitational-wave (GW) observations [5–15]. Many of these tests probe regimes where gravitational fields are weak, spacetime curvature is small, and characteristic velocities are not comparable to the speed of light. Observations of compact binary coalescences enable us to test GR in extreme environments of strong gravitational fields, large spacetime curvature, and velocities comparable to the speed of light; high post-Newtonian (PN) order calculations and numerical relativity (NR) simulations are required to accurately model the emitted GW signal [5,6,14,15].

We report results from tests of GR on binary black hole (BBH) signals using the second gravitational-wave transient catalog (GWTC-2) [16]. The GWTC-2 catalog includes all observations reported in the first catalog (GWTC-1) [17], covering the first (O1) and second (O2) observing runs, as well as new events identified in the first half of the third observing run (O3a) of the Advanced LIGO and Advanced Virgo detectors [16]. We focus on the most significant signals, requiring them to have been detected with a false-alarm rate (FAR) $< 10^{-3}$ yr^{-1}.

A current limitation on tests of beyond-GR physics with compact binary coalescences is the lack of understanding of the strong-field merger regime in nearly all modified theories of gravity. This restricts our analysis to testing the null hypothesis, taken to be GR, using model-independent or parametrized tests of GR [5,14,15,18–29]. An important goal in constraining beyond-GR theories is the development of model-dependent tests, requiring analytical waveforms and NR simulations in alternative theories of gravity across the binary parameter space. Unfortunately, there is still a lack of alternative theories of gravity that are mathematically well-posed, physically viable, and provide sufficiently well-defined alternative predictions for the GW signal emitted by two coalescing compact objects. Recent NR studies have begun to model astrophysically relevant binary black hole mergers in beyond-GR theories [30–34] and numerous advances have been made deriving the analytical equations of motion and gravitational waveforms in such theories [35–48]. However, it is often unknown whether the full theories are well-posed, and a significant amount of work is required before the results can be used in the context of GW data analysis.

The approach taken here is therefore to (i) check the consistency of GR predictions with the data, and (ii) introduce parametrized modifications to GR waveforms in order to constrain the degree to which the deviations from the GR predictions agree with the data. As in [15], the results in this

---

[*]Full author list given at end of the article.

paper should be treated as observational constraints on deviations from GR. Such limits are a quantitative indication of the degree to which the data are described by GR but can also be reinterpreted in the context of a given modified theory of gravity to produce constraints, subject to a number of assumptions [7,49]. Our analyses do not reveal any inconsistency with GR, and the results improve on the previous tests of GR using the BBHs observed in O1 and O2 [5,6,8,13–15].

The analyses performed in this paper can be broken down into four broad categories. In order to test the consistency of the GR predictions in a generic way, we look for residual power after subtracting the best-fit GR waveform from the data. We also separately study the low-frequency and high-frequency portions of an observed signal, and evaluate the agreement of the inferred parameters. To constrain specific deviations from GR, we perform parametrized tests targeting the generation of GWs and the propagation of the GW signal. All these approaches were already implemented in [15] for GWTC-1 signals. In addition, we introduce a new suite of analyses: an extension of the parametrized test considering terms from the spin-induced quadrupole moment of the binary components, dedicated studies of the remnant properties (ringdown and echoes), and a new method for probing the geometry of GW polarizations.

The tests considered here are not all independent and will have some degree of overlap or redundancy. Whilst a detailed discussion and study of the complex relationships between the tests is beyond the scope of this paper, it is important to highlight potential complementarity between the analyses. For example, any physics that modifies the generation of GWs would also likely lead to modifications to their propagation. Similarly, physics that modifies the nature of the remnant object might also predict modifications to the earlier inspiral dynamics. Furthermore, several types of deviations from GR may be picked up simultaneously by multiple analyses.

The rapid increase in the number of observed binary coalescences has driven interest in how we can best combine information from a set of measurements. In order to address this question, we employ hierarchical inference on a subset of our analyses to parametrize and constrain the distribution of observed beyond-GR parameters for different sources [50,51]. This allows us to make quantitative statements about the overall agreement of our observations with the null hypothesis that GR is correct and that no strong systematics are present. Such measurements are qualitatively more general than combined constraints previously presented in [15]. In Sec. III we discuss parameter inference for individual events and detail how the hierarchical analysis is performed on the full set of measurements.

Our constraints on deviations from GR are currently dominated by statistical uncertainty induced by detector noise [5,15,52]. Yet, the statistical uncertainty can be reduced by combining the results from multiple events. Additional uncertainty will arise from systematic error in the calibration of the detectors and power spectral density (PSD) estimation, as well as errors in the modeling of GW waveforms in GR; unlike uncertainty induced by detector noise, such errors do not improve when combining multiple events and therefore will dominate the uncertainty budget for sufficiently large catalogs of merger events. Most of the tests in this paper are sensitive to such systematics, which could mimic a deviation from GR. However, we do not find any evidence of GR violations that cannot be accounted for by possible systematics.

This paper is organized as follows. Section II provides an overview of the data used in the analysis. It also defines the event selection criteria and discusses which GW events are used to produce the individual and combined results presented in this paper. We provide details about gravitational waveforms and data analysis methods in Sec. III. In Sec. IV we present the residuals test, and the inspiral-merger-ringdown (IMR) consistency test. In Sec. V we outline tests of GW generation, including generic parametrized modifications and a test of the spin-induced quadrupole moment. In Sec. VI we describe tests of GW propagation using a modified dispersion relation. We present tests of the remnant properties in Sec. VII and study GW polarizations in Sec. VIII. Finally, we conclude with Sec. IX.

Data products associated with the results of analyses in this paper can be found in [53]. The GW strain data for all events are available at the Gravitational Wave Open Science Center [54,55].

II. DATA, EVENTS, AND SIGNIFICANCE

The analyses presented here use data taken during O3a by Advanced LIGO [56] and Advanced Virgo [57]. O3a extended from 1 April 2019 to 1 October 2019. All three detectors achieved sensitivities significantly better than those in the previous observing run [17]. Calibration [58–61] accuracy of a few percent in amplitude and a few degrees in phase was achieved at all sites. To improve the precision of parameter estimation, various noise subtraction methods [62–65] were applied to some of the events used here (see Table V in [16] for the list of events requiring such mitigation). See [16] for detailed discussion of instrument performance and data quality for O3a.

We present results for the detections of possible BBH events in O3a with FAR $< 10^{-3}$ per year, as reported by any of the pipelines featured in [16]. This threshold is stricter than the one in [15] to accommodate the increased number of events within computational constraints. The 24 selected events, and some of their key properties, are listed in Table I. Out of those, GW190814 is the only one to have been identified as a possible neutron star-black hole (NSBH) system based on the inferred component masses, although the true nature of the secondary object

TABLE I. List of O3a events considered in this paper. The first block of columns gives the names of the events and lists the instruments (Inst.) involved in each detection, as well as some relevant properties obtained assuming GR: luminosity distance D_L, redshifted total mass $(1+z)M$, redshifted chirp mass $(1+z)\mathcal{M}$, redshifted final mass $(1+z)M_f$, dimensionless final spin $\chi_f = c|\vec{S}_f|/(GM_f^2)$ in [16], and signal-to-noise ratio SNR. Reported quantities correspond to the median and 90% symmetric credible intervals, as computed in Table VI. The last block of columns indicates which analyses are performed on a given event according to the selection criteria in Sec. II: RT = residuals test (Sec. IV A); IMR = inspiral-merger-ringdown consistency test (Sec. IV B); PAR = parametrized tests of GW generation (Sec. V A); SIM = spin-induced moments (Sec. V B); MDR = modified GW dispersion relation (Sec. VI); RD = ringdown (Sec. VII A); ECH = echoes searches (Sec. VII B); POL = polarization content (Sec. VIII).

| Event | Inst. | Properties | | | | | | Tests performed | | | | | | | |
		D_L [Gpc]	$(1+z)M$ [$M_\odot$]	$(1+z)\mathcal{M}$ [$M_\odot$]	$(1+z)M_f$ [$M_\odot$]	χ_f	SNR	RT	IMR	PAR	SIM	MDR	RD	ECH	POL
GW190408_181802	HLV	$1.55^{+0.40}_{-0.60}$	$55.5^{+3.5}_{-3.8}$	$23.7^{+1.4}_{-1.7}$	$53.0^{+3.2}_{-3.4}$	$0.67^{+0.06}_{-0.07}$	$15.3^{+0.2}_{-0.3}$	✓	✓	✓	✓	✓	✓	✓	✓
GW190412	HLV	$0.74^{+0.14}_{-0.17}$	$44.2^{+4.5}_{-4.6}$	$15.2^{+0.2}_{-0.2}$	$42.9^{+4.6}_{-4.7}$	$0.67^{+0.05}_{-0.06}$	$18.9^{+0.2}_{-0.3}$	✓	⋯	✓	✓	✓	⋯	✓	✓
GW190421_213856	HL	$2.88^{+1.37}_{-1.38}$	$108.7^{+15.3}_{-12.4}$	$46.6^{+6.6}_{-6.0}$	$103.9^{+14.1}_{-11.13}$	$0.67^{+0.10}_{-0.11}$	$10.7^{+0.2}_{-0.4}$	✓	✓	✓	⋯	✓	✓	✓	⋯
GW190503_185404	HLV	$1.45^{+0.69}_{-0.63}$	$91.6^{+11.2}_{-11.8}$	$38.6^{+5.3}_{-6.0}$	$87.6^{+10.2}_{-10.8}$	$0.66^{+0.09}_{-0.12}$	$12.4^{+0.2}_{-0.3}$	✓	✓	✓	⋯	✓	✓	✓	✓
GW190512_180714	HLV	$1.43^{+0.55}_{-0.55}$	$45.3^{+3.9}_{-2.8}$	$18.6^{+0.9}_{-0.8}$	$43.5^{+4.0}_{-2.8}$	$0.65^{+0.07}_{-0.07}$	$12.2^{+0.2}_{-0.4}$	✓	✓	✓	✓	✓	⋯	✓	✓
GW190513_205428	HLV	$2.06^{+0.88}_{-0.80}$	$73.6^{+12.7}_{-6.7}$	$29.5^{+5.6}_{-2.5}$	$70.6^{+11.5}_{-6.7}$	$0.68^{+0.14}_{-0.12}$	$12.9^{+0.3}_{-0.4}$	✓	✓	✓	✓	✓	✓	✓	✓
GW190517_055101	HLV	$1.86^{+1.62}_{-0.84}$	$85.4^{+9.6}_{-7.3}$	$35.9^{+4.0}_{-3.4}$	$79.8^{+8.8}_{-6.4}$	$0.87^{+0.05}_{-0.07}$	$10.7^{+0.4}_{-0.6}$	✓	✓	✓	✓	✓	✓	✓	✓
GW190519_153544	HLV	$2.53^{+1.83}_{-0.92}$	$155.1^{+16.7}_{-17.9}$	$65.1^{+7.7}_{-10.3}$	$146.8^{+14.7}_{-15.4}$	$0.79^{+0.07}_{-0.13}$	$15.6^{+0.2}_{-0.3}$	✓	✓	✓	✓	✓	✓	✓	✓
GW190521	HLV	$3.92^{+2.19}_{-1.95}$	$269.4^{+39.8}_{-34.6}$	$114.8^{+15.2}_{-17.6}$	$256.6^{+36.6}_{-30.4}$	$0.71^{+0.12}_{-0.16}$	$14.2^{+0.3}_{-0.3}$	✓	✓	✓	⋯	⋯	✓	✓	✓
GW190521_074359	HL	$1.24^{+0.40}_{-0.57}$	$92.6^{+4.8}_{-5.4}$	$39.8^{+2.2}_{-3.0}$	$88.0^{+4.3}_{-4.8}$	$0.72^{+0.05}_{-0.07}$	$25.8^{+0.1}_{-0.2}$	✓	✓	✓	✓	✓	✓	✓	✓
GW190602_175927	HLV	$2.69^{+1.79}_{-1.12}$	$171.8^{+23.2}_{-20.6}$	$72.9^{+10.8}_{-13.7}$	$163.8^{+20.7}_{-18.3}$	$0.70^{+0.18}_{-0.14}$	$12.8^{+0.2}_{-0.3}$	✓	✓	✓	⋯	✓	✓	✓	✓
GW190630_185205	LV	$0.89^{+0.56}_{-0.37}$	$69.6^{+4.2}_{-3.5}$	$29.4^{+1.6}_{-1.5}$	$66.3^{+4.2}_{-3.3}$	$0.70^{+0.05}_{-0.07}$	$15.6^{+0.2}_{-0.3}$	✓	✓	✓	✓	✓	✓	✓	✓
GW190706_222641	HLV	$4.42^{+2.59}_{-1.93}$	$180.3^{+23.3}_{-27.7}$	$75.1^{+11.0}_{-17.5}$	$171.1^{+20.0}_{-23.7}$	$0.78^{+0.09}_{-0.18}$	$12.6^{+0.2}_{-0.4}$	✓	✓	✓	⋯	✓	✓	✓	✓
GW190707_093326	HL	$0.77^{+0.38}_{-0.37}$	$23.1^{+1.8}_{-0.5}$	$9.89^{+0.1}_{-0.09}$	$22.1^{+1.9}_{-0.5}$	$0.66^{+0.03}_{-0.04}$	$13.3^{+0.2}_{-0.4}$	✓	⋯	✓	✓	✓	⋯	✓	✓
GW190708_232457	LV	$0.88^{+0.33}_{-0.39}$	$36.1^{+2.5}_{-0.8}$	$15.5^{+0.3}_{-0.2}$	$34.4^{+2.7}_{-0.7}$	$0.69^{+0.04}_{-0.04}$	$13.3^{+0.2}_{-0.4}$	✓	✓	✓	✓	✓	⋯	✓	✓
GW190720_000836	HLV	$0.79^{+0.69}_{-0.32}$	$24.9^{+5.0}_{-1.2}$	$10.4^{+0.2}_{-0.1}$	$23.7^{+5.2}_{-1.2}$	$0.72^{+0.06}_{-0.05}$	$11.0^{+0.3}_{-0.7}$	✓	✓	✓	✓	✓	✓	✓	✓
GW190727_060333	HLV	$3.03^{+1.54}_{-1.50}$	$104.4^{+11.9}_{-10.9}$	$44.7^{+5.3}_{-5.7}$	$99.2^{+10.7}_{-9.8}$	$0.73^{+0.10}_{-0.10}$	$11.9^{+0.3}_{-0.5}$	✓	✓	✓	⋯	✓	✓	✓	✓
GW190728_064510	HLV	$0.87^{+0.26}_{-0.37}$	$23.9^{+5.3}_{-0.7}$	$10.1^{+0.09}_{-0.08}$	$22.7^{+5.5}_{-0.7}$	$0.71^{+0.04}_{-0.04}$	$13.0^{+0.2}_{-0.4}$	✓	✓	✓	✓	✓	⋯	✓	✓
GW190814	LV[a]	$0.24^{+0.04}_{-0.05}$	$27.1^{+1.1}_{-1.0}$	$6.41^{+0.09}_{-0.02}$	$26.9^{+1.1}_{-1.0}$	$0.28^{+0.02}_{-0.02}$	$24.9^{+0.1}_{-0.2}$	✓	✓	✓	✓	✓	✓	✓	⋯
GW190828_063405	HLV	$2.13^{+0.66}_{-0.93}$	$79.9^{+6.9}_{-5.9}$	$34.5^{+2.9}_{-2.8}$	$75.7^{+6.0}_{-5.2}$	$0.75^{+0.06}_{-0.07}$	$16.2^{+0.2}_{-0.3}$	✓	✓	✓	✓	✓	✓	✓	✓
GW190828_065509	HLV	$1.60^{+0.62}_{-0.60}$	$44.4^{+6.4}_{-4.0}$	$17.4^{+0.6}_{-0.7}$	$42.7^{+6.6}_{-4.2}$	$0.65^{+0.08}_{-0.08}$	$10.0^{+0.3}_{-0.5}$	✓	⋯	✓	⋯	✓	⋯	✓	⋯
GW190910_112807	LV	$1.46^{+1.03}_{-0.58}$	$101.9^{+10.4}_{-7.8}$	$43.9^{+4.6}_{-3.6}$	$97.0^{+9.3}_{-7.1}$	$0.70^{+0.08}_{-0.07}$	$14.1^{+0.3}_{-0.3}$	✓	✓	✓	✓	✓	✓	✓	✓
GW190915_235702	HLV	$1.62^{+0.71}_{-0.61}$	$78.3^{+8.4}_{-8.1}$	$33.1^{+3.3}_{-3.9}$	$74.8^{+7.9}_{-7.4}$	$0.70^{+0.09}_{-0.11}$	$13.6^{+0.2}_{-0.3}$	✓	✓	✓	✓	✓	✓	✓	✓
GW190924_021846	HLV	$0.57^{+0.22}_{-0.22}$	$15.5^{+5.7}_{-0.7}$	$6.44^{+0.04}_{-0.03}$	$14.8^{+5.9}_{-0.8}$	$0.67^{+0.05}_{-0.04}$	$11.5^{+0.3}_{-0.4}$	✓	⋯	✓	⋯	✓	⋯	✓	✓

[a]Parameter estimation for GW190814 made use of data from the three instruments, HLV, although search pipelines only considered LV [66].

remains unknown [66]. In this paper, we start from the null hypothesis that all signals analyzed (including GW190814) correspond to BBHs as described by GR, and proceed to seek evidence in the data to challenge this (we find none). We do not study the likely binary neutron star signal GW190425 [67].

Detection significance is provided by two pipelines that rely on GR templates (PYCBC [68–70] and GSTLAL [71,72], both relying on the waveform models described in [73–76] and [77]), and by one pipeline that does not (COHERENT WAVEBURST, henceforth CWB [78–80]). Making use of a measure of significance that assumes the validity of GR could potentially lead to biases in the selection of events to be tested, systematically disfavoring signals in which a GR violation would be most evident (e.g., [81]). CWB would detect at least some of the conceivable chirplike signals with sufficient departures from GR that they would be missed by the templated searches. Nonetheless, we cannot fully discard the existence of a hidden population of signals exhibiting large deviations from GR, which could escape both modeled and unmodeled searches.

Out of all the events reported in [16], only the massive event GW190521 was identified with greater significance by the unmodeled search. This can be explained as a consequence of the system's high mass, which led to a short signal with only ~4 cycles visible in our detectors [82,83]. This fact makes it more difficult to evaluate consistency with GR for this event than for other (less massive) systems which remain in the sensitive band of our detectors for a longer period. This is especially true for tests targeting the inspiral, since there is little signal-to-noise ratio (SNR) before the merger (SNR $\approx$ 4.7, computed as in Sec. IV B); on the other hand, this signal is highly suitable for studies of black hole (BH) ringdown [83].

We consider each of the GW events individually, carrying out different analyses depending on the properties of each signal. Some of the tests presented here, such as the IMR consistency test in Sec. IV B and the parametrized tests in Sec. V, distinguish between the inspiral and the postinspiral regimes of the signal. The remnant-focused analyses of Sec. VII are only meaningful for systems massive enough for the postinspiral signal to be detectable by LIGO-Virgo. Finally, studies of polarization content are only feasible for detections involving the full three-detector network. We choose which analyses to apply in each case following preestablished selection criteria based on the signal power recovered in different frequency regimes or the number of involved detectors. Table I indicates which events have met the selection criteria for each analysis; further details are provided in the sections below.

Having a large number of detections also allows us to make statements about the validity of GR from the set of measurements as a whole. Ideally, we would like to constrain the properties of the true population of signals that exist in nature—for example, if GR is correct, the population distribution of parametrized deviations from GR would be a δ function at the point corresponding to no deviation. However, this would require an understanding of our detection efficiency as a function of these deviations [84,85], as well as a joint model for the distribution of individual event properties and deviations from GR [86]. Because no such comprehensive modeling is available, we do not attempt to make any statements about possible intrinsic populations, but rather measure the distribution of deviations from GR across *observed* signals. Our strategies for doing so are outlined in Sec. III B.

Given the increased significance threshold for inclusion in this paper, we dispense with the two-tiered selection criterion applied in [15]. Instead, we make combined statements using all events in our selection. When possible, we also combine our results for O3a with those from preceding observation runs that satisfy our selection criterion. That includes all events analyzed in [15] except GW151012 and GW170729; that is: GW150914, GW151226, GW170104, GW170608, GW170809, GW170814, GW170818, and GW170823.[1] This is done for tests already presented in [15] (residuals test, IMR consistency, parametrized tests, and modified dispersion relations), as well as for new analyses for which pre-O3a results are presented here for the first time (spin-induced moments, ringdown, and polarizations).

In some cases we perform tests on events that yield uninformative results, so that the posterior distribution extends across the full extent of the prior. This means that upper limits in such cases are determined by the prior and thus are arbitrary. However, this is not a problem when considering the set of measurements as a whole using the techniques described in Sec. III B.

III. PARAMETER INFERENCE

A. Individual events

The foundation for almost all of the tests presented in this paper are the waveform models that describe the GW signal emitted from a coalescing compact binary. The only exception is the polarization analysis (Sec. VIII), which relies on null-stream projections of the data [87,88]. In GR, the GW signal from a BBH on a quasicircular orbit is fully characterized by 15 parameters [89]. These include the intrinsic parameters (the masses $m_{1,2}$ and spin angular momenta $\vec{S}_{1,2}$ of the binary components) and extrinsic ones (the luminosity distance, the location of the binary in the sky, the orientation of its orbit with respect to observer's line of sight, its polarization angle, and the reference time and orbital phase). The dominant effects of the BHs' spin angular momenta on the waveform comes from the spin components along the orbital axis. However, the other

---

[1]Unlike in this paper, combined results in [15] did not include GW170818 because it was only detected by a single pipeline.

components of the spins lead to precession of the spin vectors and the binary's orbital plane, introducing modulations into the GW amplitude and phase [90,91]. We find that aligned-spin waveform models are sufficient for many events in this paper, but we analyze all events with at least one precessing waveform model, to take these effects into account.

The working null hypothesis throughout the paper is that all events are quasicircular BBHs in GR, with no measurable systematics. In principle, a BBH waveform could be affected by the presence of eccentricity, which is not included in any of the waveform models we use. The presence of significant eccentricity could result in systematic errors mimicking a deviation from GR [92–94]. If evidence for such a deviation was found, extra work would be required to discard eccentricity, matter effects (for less massive systems), or other systematics.

For a majority of the tests we employ two waveform families to model signals from BBHs in GR. One is the nonprecessing effective-one-body (EOB) waveform family SEOBNRV4 [77], an analytical model that takes inputs from post-Newtonian theory, BH perturbation theory, the gravitational self-force formalism, and NR simulations. For computational efficiency in the analyses, we use a frequency-domain reduced-order model for SEOBNRV4 known as SEOBNRV4_ROM [77]. There exists a precessing EOB waveform model SEOBNRV4P [95–97], which has been employed in [16], but we do not use it here due to its high computational cost. The other waveform family is the precessing phenomenological waveform family IMRPHENOMPV2 [98–100], a frequency-domain model that describes the spin precession effects in terms of two effective parameters by twisting up the underlying aligned-spin model [101–103]. The aligned-spin model is itself calibrated to hybrid waveforms, which are constructed by stitching together waveforms from the inspiral part (modeled using the SEOBNRv2 [104] model without calibration from NR) and the merger–ringdown part (modeled using NR simulations) of the coalescence. The two waveform models, IMRPHENOMPV2 and SEOBNRV4_ROM, are employed to help gauge systematics, as discussed in detail in Sec. VA. Although a detailed study of waveform systematics is beyond the scope of this paper, relevant studies can be found in [77,97,99,105–110].

During O3a, we observed a number of events for which higher-order (nonquadrupole) multipole moments of the radiation were shown to affect parameter estimation; this includes GW190412 [111], GW190521 [82,83], and GW190814 [66]. Where possible and appropriate, we employ one of three waveform models incorporating higher moments (HMs): IMRPHENOMPV3HM [112,113], SEOBNRV4HM_ROM [105,107], or NRSUR7DQ4 [114]. IMRPHENOMPV3HM is a successor of IMRPHENOMPV2 that includes two-spin precession [115] and the $(\ell, |m|) = (2, 2), (2, 1), (3, 3), (3, 2), (4, 4), (4, 3)$ multipoles;

SEOBNRV4HM_ROM is built upon SEOBNRV4HM which incorporates $(\ell, |m|) = (2, 2), (2, 1), (3, 3), (4, 4), (5, 5)$; finally, NRSUR7DQ4 is a surrogate model that is built by directly interpolating NR simulations, accounting for all spin degrees of freedom and all multipoles with $\ell \leq 4$, in the coprecessing frame. When we use IMRPHENOMPV2, IMRPHENOMPV3HM, and NRSUR7DQ4, we impose a prior $m_2/m_1 \geq 1/18, 1/18, 1/6$, respectively, on the mass ratio, as these waveform families are not known to be valid for lower m_2/m_1. Whenever we make use of a waveform other than IMRPHENOMPV2 or SEOBNRV4_ROM, we state so explicitly in the text.

A majority of the tests presented in this paper are performed using the LALINFERENCE code [116] in the LIGO Scientific Collaboration Algorithm Library Suite (LALSUITE) [117]. This code is designed to carry out Bayesian inference using two possible sampling algorithms: Markov-chain Monte Carlo (MCMC), and nested sampling. More detail on how the binary parameters are estimated can be found in Sec. V of [16]. In LALINFERENCE analyses, the PSD used was either estimated at the time of each event using the BAYESWAVE code [65,118] or estimated near the time of an event using Welch's method [119]. Unless otherwise specified, the prior distributions of various GR parameters (intrinsic and extrinsic) for each event are the same as in [16]. The priors on non-GR parameters specific to each test are discussed in their respective sections below. Other quantities such as the frequency range (over which the matched-filter output is computed) for each event is kept the same as in [16], unless otherwise specified.

Exceptions to the use of LALINFERENCE include the residuals test of Sec. IV A, the IMR consistency test of Sec. IV B, one of the ringdown studies in Sec. VII A, and the polarization analysis of Sec. VIII. The residuals test uses BAYESWAVE directly to carry out inference on the residual data. Additional to LALINFERENCE, the IMR consistency test also employs a parallelized nested sampling pipeline PBILBY [89,120,121]. The damped-sinusoid ringdown analysis is carried out with the PYRING pipeline [122,123]. The polarization analysis is carried out with the BANTAM pipeline [88].

Finally, we assumed the same cosmology for all the events in this paper to infer their unredshifted masses and the proper distances (as required in Sec. VI). Specifically, we take $H_0 = 67.90 \text{ km s}^{-1} \text{ Mpc}^{-1}$ for the Hubble constant, and $\Omega_m = 0.3065$ and $\Omega_\Lambda = 0.6935$ for the matter and dark energy density parameters ("TT + lowP + lensing + ext" values from [124]).

B. Sets of measurements

There are multiple statistical strategies for drawing inferences from a set of events, each carrying its own set of assumptions about the nature of potential deviations from GR and how they may manifest in our signals. For simplicity, [15] reported constraints assuming that

deviations from GR would manifest equally across events, independent of source properties. This is only strictly justifiable when the deviation parameters are known by construction to be the same for all detected events (or some known function of the source properties). This is the case for probes of the propagation of GWs (e.g., dispersion), where the propagation effects can reasonably be assumed to affect all sources equally (barring a known dependence on the luminosity distance, which is explicitly factored out of the analysis). However, it is generally not the case for parametrized tests of GW generation, wherein waveforms are allowed to deviate in arbitrary (albeit controlled) ways from the GR prediction.

To relax the assumption of shared deviations across events, in this paper we apply the hierarchical inference technique proposed and implemented for GWTC-1 events in [50,51]. We apply this procedure to the IMR consistency test (Sec. IV B), the waveform generation tests (Sec. V), and the ringdown analyses (Sec. VII A). The strategy consists of modeling non-GR parameters for each event in our pool as drawn from a common underlying distribution, whose properties we infer coherently from the data for all events as whole [84,125]. The nature of such unknown distribution would be determined by the true theory of gravity and the population of sources (e.g., the magnitude of the departure from GR could be a function of the total mass of the binary), convolved with any biases affecting our selection of events. By comparing the inferred distribution to the GR prediction (no deviation for any of the events), we obtain a null test of GR from our whole set of observations.

Unlike other contexts in which hierarchical techniques are used (notably, the study of astrophysical populations [86,126]), the goal here is always to characterize the distribution of measured quantities for the events in our set, not to make inferences about underlying astrophysical distributions that are not directly accessible (as discussed in Sec. II). This simplifies our hierarchical model, which does not attempt to deconvolve selection biases. However, it limits the kinds of conclusions we may draw from our observations, since they will necessarily pertain strictly to the signals that we have detected and analyzed.

Although the true nature of the hyperdistribution could be arbitrarily complex, we may always capture its essential features by means of a moment expansion. To achieve this, we model the true values of each beyond-GR parameter in our pool of events as drawn from a Gaussian of unknown mean μ and standard deviation σ [51]. This is a suitable choice because the Gaussian is the least informative distribution (i.e., it has maximum entropy conditional on the first two moments) [127]. GR is recovered for $\sigma = 0$ and $\mu = x_{GR}$, where x_{GR} is the GR prediction for the parameter at hand (e.g., $x_{GR} = 0$ for parameters defined as a fractional deviation away from GR). As the number of detections increases in the future, we may enhance

flexibility by including additional moments in our model (akin to adding further terms in a series expansion). In spite of its simplicity, the Gaussian parametrization has been shown to work effectively even when the true distribution presents highly nontrivial features, like correlations across the beyond-GR parameters [51]. A set of measurements not conforming to GR would be identified through posteriors on μ and σ that are inconsistent with the GR values at the 90% credible level.

We obtain posteriors on the hyperparameters μ and σ through a joint analysis of the set of detections, using the STAN-based [128] infrastructure developed in [51]. We summarize the results from that hierarchical analysis through the population-marginalized distribution for the beyond-GR parameters, also known as the *observed population predictive distribution* [86]. For a given beyond-GR parameter x, this distribution $p(x|d)$ is the expectation for x after marginalizing over the hyperparameters μ and σ,

$$p(x|d) = \int p(x|\mu, \sigma) p(\mu, \sigma|d) \mathrm{d}\mu \mathrm{d}\sigma, \qquad (1)$$

where d represents the data for *all* detected events, and $p(x|\mu, \sigma) \sim \mathcal{N}(\mu, \sigma)$ by construction [51]. Since we are characterizing a group of observations, not an astrophysical distribution, there is no factor in Eq. (1) accounting for selection biases. A posterior expectation $p(x|d)$ that supports $x = x_{GR}$ is a necessary, but insufficient, condition for establishing agreement with GR—since we must also have σ consistent with zero. If GR is correct and in the absence of systematics, $p(x|d)$ should approach a Dirac δ function at x_{GR} with increasing number of observations. Assuming x_{GR} is supported by $p(x|d)$, the width of this distribution is a measure of our uncertainty about deviations from GR in this parameter after combining all events.

Requiring that all events share the same value of the beyond-GR parameter is equivalent to demanding $\sigma = 0$. Fixing $\sigma = 0$, the hierarchical method reduces to the approach of multiplying likelihoods from individual events [50], as done in [15]. Equation (1) may then be interpreted as a posterior on the value of x, and is identical to the combined posteriors as computed in [15]. In the sections below, we present both types of combined results (inferred σ, and fixed $\sigma = 0$), facilitating comparisons to previously reported constraints. For a concrete demonstration of the usefulness of the hierarchical approach see Sec. IV B (and the related Appendix B), where we show how this technique successfully identifies a subset of signals not conforming to the null hypothesis (due to known systematics, in this case), while the multiplied-likelihood approach does not.

Finally, under certain circumstances, statements from the set of measurements may be obtained by studying the empirical distribution of some detection statistic for a frequentist null test of the hypothesis that GR is a good

description of the data. As for the residuals test (Sec. IV A), this may be done if the analysis yields a distribution of p-values, obtained by comparing some detection statistic against an empirical background distribution for each event. If the null hypothesis holds, we expect the resulting p-values to be uniformly distributed in the interval [0, 1]. Agreement with this expectation can be quantified through a meta p-value obtained through Fisher's method [129]. It can also be represented visually through a probability-probability (PP) plot displaying the fraction of events yielding p-values smaller than or equal to any given number: under the null hypothesis, the PP plot should be diagonal (see also Appendix A).

IV. CONSISTENCY TESTS

A. Residuals test

A generic way of quantifying the success of our GR waveforms in describing the data is to study the residual strain after subtracting the best-fit template for each event [130]. Residual analyses are sensitive to any sort of modeling systematics, whether they arise from a deviation from GR or more prosaic reasons. Results from similar studies were previously presented in [5,15,66,83].

We follow the procedure described in [15]. For each event in our set, we subtract the maximum likelihood (best-fit) GR-based waveform from the data to obtain residuals for a 1 s window centered on the trigger time reported in [16]. Except for the three events detailed in Table II, we obtain the GR prediction using the IMRPHENOMPV2 waveform family.[2] We then use BAYESWAVE to place a 90%-credible upper-limit on the leftover coherent signal-to-noise ratio (SNR). To evaluate whether this value, SNR_{90}, is consistent with instrumental noise fluctuations, we measure the coherent power in 193 sets of noise-only detector data around each event. This yields a p-value for noise-producing coherent power with SNR_{90}^{n} greater than or equal to the residual value SNR_{90}, i.e., $p = P(SNR_{90}^{n} \geq SNR_{90}|noise)$.

Our results for O3a events are summarized in Table III (see Table II in [15] for O1 and O2 events). For each event, we present the values of the residual SNR_{90}, as well as the corresponding fitting factor $FF_{90} = SNR_{GR}/(SNR_{res}^{2} + SNR_{GR}^{2})^{1/2}$, where SNR_{res} is the coherent residual SNR and SNR_{GR} is the SNR of the best-fit template. This quantifies agreement between the best-fit template and the data as being better than $FF_{90} \times 100\%$ [5,15]. Table III also shows the SNR_{90} p-values.

Figure 1 displays the SNR_{90} values reported in Table III as a function of the SNR of the best-fit template, with SNR_{90} p-values encoded in the marker colors; events preceding O3 are identified by an empty marker (see Table II in [15]). If the GR model is a good fit for the

---

[2]For GW190814, we also used SEOBNRV4PHM, which yielded results consistent with IMRPHENOMPV3HM [66].

TABLE II. Waveforms subtracted to study residuals in Sec. IV A.

Event	Ref.	Approximant	Ref.
GW190412	[111]	IMRPHENOMPV3HM	[112,113]
GW190521	[82,83]	NRSUR7DQ4	[106]
GW190814	[66]	IMRPHENOMPV3HM	[112,113]
All others	[16]	IMRPHENOMPV2	[98–100]

data, the magnitude of SNR_{90} should depend only on the state of the instruments at the time of each event, not on the amplitude of the subtracted template. This is consistent with Fig. 1, which reveals no sign of such a trend.

The variation in SNR_{90} is linked to the distribution of the corresponding p-values, as suggested by Fig. 1. The O3a event yielding the highest (lowest) p-value is GW190727_060333 (GW190421_213856) with $SNR_{90} = 4.88$ and $p = 0.97$ ($SNR_{90} = 7.52$ and $p = 0.07$) and is highlighted in Fig. 1 by a red (blue) diamond. Although GW190408_181802 is the O3a event with the highest residual power ($SNR_{90} = 8.48$), the p-value of 0.15 indicates that this is not inconsistent with the background distribution. Two pre-O3a events, GW170814 and GW170818, yielded higher SNR_{90} than GW190408_181802 [15], as seen in Fig. 1.

TABLE III. Results of the residuals analysis (Sec. IV A). For each event, we present the SNR of the subtracted GR waveform (SNR_{GR}), the 90%-credible upper limit on the residual network SNR (SNR_{90}), a corresponding lower limit on the fitting factor (FF_{90}), and the p-value.

| Events	SNR_{GR}	Residual SNR_{90}	FF_{90}	p-value
GW190408_181802	16.06	8.48	0.88	0.15
GW190412	18.23	6.67	0.94	0.30
GW190421_213856	10.47	7.52	0.81	0.07
GW190503_185404	13.21	5.78	0.92	0.83
GW190512_180714	12.81	5.92	0.91	0.44
GW190513_205428	12.85	6.44	0.89	0.70
GW190517_055101	11.52	6.40	0.87	0.69
GW190519_153544	15.34	6.38	0.92	0.65
GW190521	14.23	6.34	0.91	0.28
GW190521_074359	25.71	6.15	0.97	0.35
GW190602_175927	13.22	5.46	0.92	0.86
GW190630_185205	16.13	5.13	0.95	0.52
GW190706_222641	13.39	7.80	0.86	0.18
GW190707_093326	13.55	5.89	0.92	0.25
GW190708_232457	13.97	6.00	0.92	0.19
GW190720_000836	10.56	7.30	0.82	0.18
GW190727_060333	11.62	4.88	0.92	0.97
GW190728_064510	13.47	5.98	0.91	0.53
GW190814	25.06	6.43	0.97	0.84
GW190828_063405	16.13	8.47	0.89	0.12
GW190828_065509	9.67	6.30	0.84	0.41
GW190910_112807	14.32	5.60	0.93	0.65
GW190915_235702	13.82	8.30	0.86	0.09
GW190924_021846	12.21	5.91	0.90	0.57
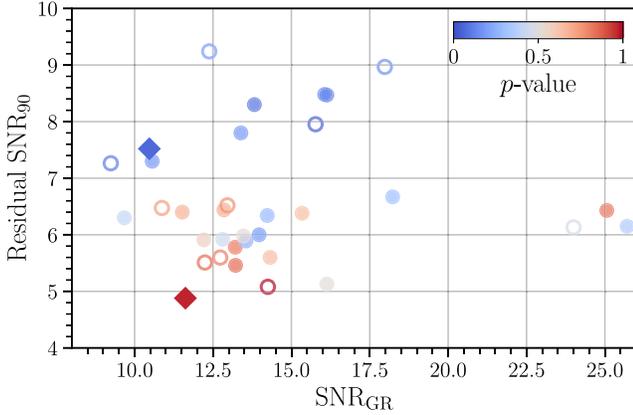
FIG. 1. Upper limit on the residual network SNR (SNR_{90}) for each event, as a function of SNR recovered by the maximum-likelihood template (SNR_{GR}), with the corresponding p-value shown in color (see Table III). Solid (empty) markers indicate events detected in O3a (O1 or O2). Diamonds highlight the O3a events yielding the highest (GW190727_060333) and lowest (GW190421_213856) p-values, $p = 0.97$ and $p = 0.07$ respectively.

The set of p-values shown in Table III is consistent with all coherent residual power being due to instrumental noise. Assuming that this is indeed the case, we expect the p-values to be uniformly distributed over [0, 1]. Agreement with a uniform distribution is represented via the PP plot in Fig. 2, which shows that the measurement agrees with the null hypothesis (diagonal line) within 90% credibility (computed as detailed in Appendix A). We also compute a meta p-value for a uniform distribution of 0.39 (see Sec. III B). This demonstrates no statistically significant deviations between the observed residual power and the detector noise around the set of events.

B. Inspiral-merger-ringdown consistency test

GR predicts that the final state of the coalescence of two BHs will be a single perturbed Kerr BH [131–134]. Assuming that GR is valid, the mass and spin of the remnant BH inferred from the low-frequency portion of the signal should be consistent with those measured from the high-frequency part [135–137], where the low- and high-frequency regimes roughly correspond to the inspiral and postinspiral, respectively, when considering the dominant mode [137]. This provides a consistency test for GR, related to the remnant-focused studies we present in Sec. VII and the postinspiral coefficients in Sec. V A.

We take the cutoff frequency f_c^{IMR} between the inspiral and postinspiral regimes to be the $m = 2$ mode GW frequency of the innermost stable circular orbit of a Kerr BH, with mass M_f and dimensionless spin magnitude χ_f estimated from the full BBH signal assuming GR. The final mass and spin are calculated by averaging NR-calibrated final-state fits [138–140], where the aligned-spin final spin fits are augmented by a contribution from the in-plane spins
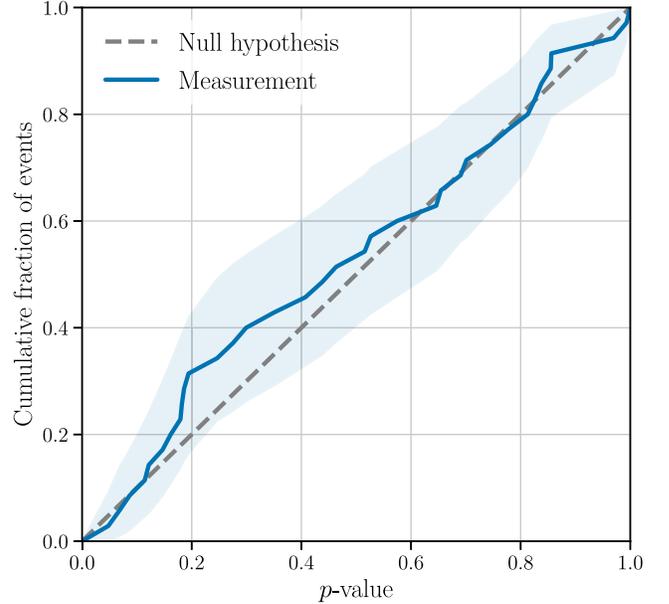

FIG. 2. Fraction of events yielding a residuals-test p-value less than or equal to the abscissa. The light-blue band marks the 90%-credible region for our measurement, factoring in the uncertainty due to a finite number of both events and background instantiations (Appendix A). The meta p-value for a uniform distribution is 0.39.

[141,142]. We compute f_c^{IMR} from augmented NR-calibrated fits applied to the posterior median values for the masses and spins of the binary components. We then independently estimate the binary's parameters from the low- (high-) frequency portion of the signal, restricting the Fourier-domain likelihood calculation to frequencies below (above) the cutoff frequency f_c^{IMR}. The two independent estimates of the source parameters are used to infer the posterior distributions of M_f and χ_f using the augmented NR-calibrated final-state fits. For the signal to be consistent with GR, the two estimates must be consistent with each other.

For this test, we require the inspiral and postinspiral portions of the signal to be informative. As a proxy for the amount of information that can be extracted from each part of the signal, we calculate the SNR of the inspiral and postinspiral part of the signal using the preferred waveform model for each event (Table II), evaluated at the maximum *a posteriori* parameters for the complete IMR posterior distributions [16]. As in [15], we only apply the IMR consistency test to events that have SNR > 6 in both regions. When studying the set of measurements as a whole (cf. Sec III B), we impose an additional criterion on the median redshifted total mass such that $(1 + z)M < 100\,M_\odot$. This additional cut further ensures that the binary contains sufficient information in the inspiral regime because the test would be strongly biased for heavy BBHs. A criterion based on mass was not applied in [15] because most GWTC-1 events automatically satisfied

TABLE IV. Results from the IMR consistency test (Sec. IV B). $f_c^{\rm IMR}$ denotes the cutoff frequency between the inspiral and postinspiral regimes; $\rho_{\rm IMR}$, $\rho_{\rm insp}$, and $\rho_{\rm postinsp}$ are the SNR in the full signal, the inspiral part, and the postinspiral part respectively; and the GR quantile $\mathcal{Q}_{\rm GR}$ denotes the fraction of the likelihood enclosed by the isoprobability contour that passes through the GR value, with smaller values indicating better consistency with GR. For lower SNRs, the likelihood is typically broader and $\mathcal{Q}_{\rm GR}$ is generally higher. An asterisk denotes events with median $(1+z)M > 100\,M_\odot$, for which we expect strong systematics. We highlight GW190412 with a dagger as we show results for comparison to [111], but the event is not used in the joint likelihood as the postinspiral SNR is below the threshold for inclusion. The difference in the results for GWTC-1 events compared to [15] is due to the change in priors.

Event	$f_c^{\rm IMR}$ [Hz]	$\rho_{\rm IMR}$	$\rho_{\rm insp}$	$\rho_{\rm postinsp}$	$\mathcal{Q}_{\rm GR}$ [%]
GW150914	132	25.3	19.4	16.1	55.7
GW170104	143	13.7	10.9	8.5	29.0
GW170809	136	12.7	10.6	7.1	26.6
GW170814	161	16.8	15.3	7.2	22.9
GW170818	128	12.0	9.3	7.2	26.8
GW170823	102	11.9	7.9	8.5	93.3
GW190408_181802	164	15.0	13.6	6.4	11.4
GW190412	213	19.1	18.2	5.9	69.0†
GW190421_213856	82	10.4	8.1	6.6	78.7*
GW190503_185404	99	13.7	115	7.5	53.2
GW190513_205428	125	13.3	11.2	7.2	35.0
GW190519_153544	78	15.0	10.0	11.2	85.6*
GW190521_074359	105	25.4	23.4	9.9	0.0
GW190630_185205	135	16.3	14.0	8.2	58.8
GW190706_222641	67	12.7	7.8	10.1	96.5*
GW190727_060333	96	12.3	10.0	7.2	98.7*
GW190814	207	24.8	23.9	6.9	99.9
GW190828_063405	132	16.2	13.8	8.5	21.5
GW190910_112807	92	14.4	9.6	10.7	29.3*

it. The cutoff frequency and SNRs for all events used in this analysis are detailed in Table IV.[3]

In order to constrain possible departures from GR, we introduce two dimensionless parameters that quantify the fractional difference between the two estimates,

$$\frac{\Delta M_{\rm f}}{\bar{M}_{\rm f}} = 2\frac{M_{\rm f}^{\rm insp} - M_{\rm f}^{\rm postinsp}}{M_{\rm f}^{\rm insp} + M_{\rm f}^{\rm postinsp}}, \qquad (2)$$

$$\frac{\Delta \chi_{\rm f}}{\bar{\chi}_{\rm f}} = 2\frac{\chi_{\rm f}^{\rm insp} - \chi_{\rm f}^{\rm postinsp}}{\chi_{\rm f}^{\rm insp} + \chi_{\rm f}^{\rm postinsp}}, \qquad (3)$$

where the superscripts denote the estimate of the mass or the spin from the inspiral and postinspiral portions of the

---

[3]The frequency $f_c^{\rm IMR}$ was determined using preliminary parameter inference results and the values in Table IV may slightly differ to those obtained using the posterior samples in GWTC-2. However, the test is robust against small changes to the cutoff frequency [137].

signal [136]. As in [15], we perform parameter estimation using uniform priors for the component masses and spin magnitudes and an isotropic prior on the spin orientations; this choice induces a highly nonuniform effective prior in $\Delta M_{\rm f}/\bar{M}_{\rm f}$ and $\Delta \chi_{\rm f}/\bar{\chi}_{\rm f}$. In order to alleviate this, and in contrast with [15], we reweight the posteriors to work with a uniform prior for the deviation parameters. This eliminates confounding factors and has the advantage of more clearly conveying the information gained from the data. For example, binary configurations with comparable mass ratios and $\chi_{\rm eff} \sim 0$ will lead to a remnant spin ~ 0.7 [138–140], which means that the $\chi_{\rm f}$ prior is concentrated around this value and that, consequently, the $\Delta \chi_{\rm f}$ is concentrated around 0; this leads to artificially narrow $\Delta \chi_{\rm f}$ posteriors that should not be interpreted as a strong constraint from the data on deviations from GR.

We summarize our results in Fig. 3, where we represent the two-dimensional posteriors for all GWTC-2 events analyzed by means of their 90% credible level. The contours are colored as a function of the median redshifted total binary mass $(1+z)M$, as inferred from the full waveform assuming GR, and we only include events with $(1+z)M < 100\,M_\odot$. Events preceding O3a are identified with a dot–dashed trace and were already analyzed in [15]. However, distributions in Fig. 3 here are generally broader than Fig. 2 of that paper because our results represent posteriors using a uniform prior. Although GW190412 does not meet the SNR threshold for this test, we highlight the posteriors for this event in Fig. 3 for comparison to previously published results [111].

We find that the GW190412 and GW190814 postinspiral distance posteriors are cut off by the upper prior bounds on the distance, 3 Gpc and 2 Gpc, respectively. Due to the low SNR in the postinspiral, the distance posterior is cut off by the prior even when increasing the upper bound on the volumetric distance prior $p(D_{\rm L}) \propto D_{\rm L}^2$. The IMR consistency results for these events are therefore unavoidably dependent on the choice of priors. To mitigate such issues, we have chosen upper bounds that lead to a small probability density near the cutoff. For future applications of the test we will consider ways to impose *a priori* selection cuts to exclude such cases from consideration.

The fraction of the posterior enclosed by the isoprobability contours that pass through the GR value, i.e., the two-dimensional GR quantile $\mathcal{Q}_{\rm GR}$, for each event is given in Table IV, where smaller values indicate better consistency with GR. For low (high) SNRs, the posteriors will be broader (narrower) and $\mathcal{Q}_{\rm GR}$ will be higher (lower) if GR is the correct hypothesis. The binary with the smallest $\mathcal{Q}_{\rm GR}$ is GW190521_074359, which has a small but nonzero quantile that is rounded to zero in Table IV. For binaries with masses $(1+z)M > 100\,M_\odot$ we typically observe $\mathcal{Q}_{\rm GR} > 50\%$, which can be explained by the known systematics mentioned above. See Appendix B for a more detailed exposition of mass-related systematics. Of the
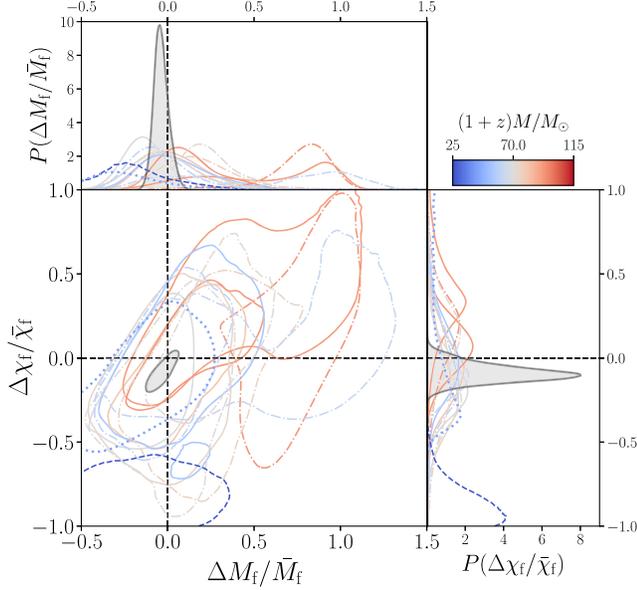
FIG. 3. Results of the IMR consistency test for the selected BBH events with median $(1+z)M < 100\ M_\odot$ (see Table IV). The main panel shows the 90% credible regions of the posteriors for $(\Delta M_f/\bar{M}_f, \Delta\chi_f/\bar{\chi}_f)$ assuming a uniform prior, with the cross marking the expected value for GR. The side panels show the marginalized posterior for $\Delta M_f/\bar{M}_f$ and $\Delta\chi_f/\bar{\chi}_f$. The gray distribution correspond to the product of all the individual posteriors. O3a (pre-O3a) events are plotted with solid (dot–dashed) traces. Color encodes the redshifted total mass in solar masses, with a turnover between blue and red around the median of the $(1+z)M/M_\odot$ distribution for the plotted events. The results for GW190412 and GW190814 are identified by dotted and dashed contours, respectively. The two events with contours that do not enclose the origin are GW170823 (dot–dashed) and GW190814 (dashed). GW190408_181802 has a multimodal posterior that results in the small contour (blue) away from zero.

binaries below the mass threshold, GW190814 has the highest quantile, $\mathcal{Q}_{GR} = 99.9\%$, but has a relatively low SNR in the postinspiral regime and a relatively low redshifted mass; the other notable outlier is GW170823, $\mathcal{Q}_{GR} = 93.3\%$, which has the lowest SNR and a relatively high redshifted mass, $(1+z)M \approx 93\ M_\odot$. For GW190814, the likelihood for the final spin fractional deviation shows a notable departure from the GR value.[4] However, GW190814 was a higher mass ratio event with very small spins, resulting in an inferred final spin of $\chi_f \sim 0.28$ [66]. As a consequence of the low SNR, the postinspiral regime is uninformative, and the posterior is dominated by the prior which peaks at $\chi_f \sim 0.7$. In contrast, the masses and spins are very accurately measured in the inspiral regime and a final spin of $\chi_f \sim 0.28$ is recovered. The apparent departure from GR can be explained by the mismatch in the information recovered between the two regimes.

---

[4]The GW190814 posterior was truncated at $\Delta\chi_f/\bar{\chi}_f = -1$ in this analysis, but we have confirmed this has no effect on $\mathcal{Q}_{GR}$.

We may interpret results from our set of observations collectively through hierarchical models for the mass and spin deviations, as described in Sec. III B. Here we treat $\Delta M_f/\bar{M}_f$ and $\Delta\chi_f/\bar{\chi}_f$ as independent parameters; future implementations may consider them jointly. With 90% credibility, we constrain the population hyperparameters (μ, σ) to be $(0.02^{+0.11}_{-0.09}, <0.17)$ and $(-0.06^{+0.15}_{-0.16}, <0.34)$ for $\Delta M_f/\bar{M}_f$ and $\Delta\chi_f/\bar{\chi}_f$ respectively, consistent with GR ($\mu = \sigma = 0$) for both parameters (posteriors provided in Appendix B). In Fig. 4, we represent the result through the population-marginalized expectation for $\Delta M_f/\bar{M}_f$ (blue) and $\Delta\chi_f/\bar{\chi}_f$ (red), as defined in Eq. (1). This measurement constrains $\Delta M_f/\bar{M}_f = 0.02^{+0.20}_{-0.17}$ and $\Delta\chi_f/\bar{\chi}_f = -0.05^{+0.36}_{-0.41}$, quite consistent with the expectation from GR.

If we assume that the fractional deviations take the same value for all events, then we obtain the less-conservative combined posterior shown in gray in Fig. 3. We find $\Delta M_f/\bar{M}_f = -0.04^{+0.08}_{-0.06}$ and $\Delta\chi_f/\bar{\chi}_f = -0.09^{+0.11}_{-0.08}$, also consistent with the GR values.

Had we included the high-mass events discussed above in the analysis, for which IMR tests are known to exhibit systematic offsets, the hierarchical method would have resulted in modest tension with GR, as discussed more fully in Appendix B. The hierarchical method with $\sigma = 0$ (assuming all events have the same deviation parameters) does not find any inconsistency when high-mass events are included, so we conclude that in this case the full hierarchical method is more sensitive to these (systematics-induced) deviations from GR.

This analysis used IMRPHENOMPV2 or IMRPHENOMPV3HM waveforms for the same events for which they were used for the residuals analysis, given in Table II. In order to gauge
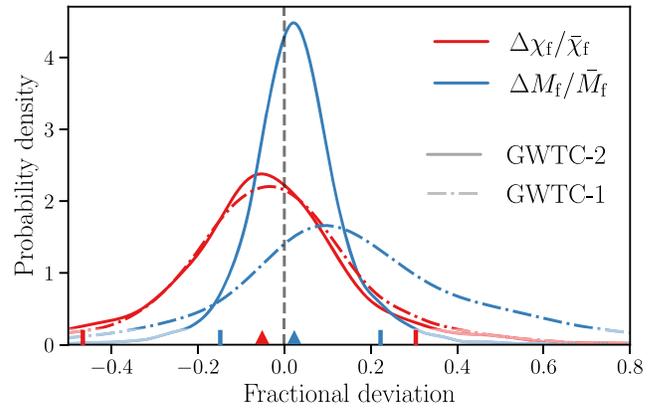

FIG. 4. Distributions for the remnant mass (blue) and spin (red) fractional deviations, as obtained by hierarchically combining the results in Fig. 3 (solid trace). For comparison, we also show the result obtained using only GWTC-1 events (dot dashed trace). The probability densities summarize our expectation for the fraction of observed events with a given value of $\Delta M_f/\bar{M}_f$ and $\Delta\chi_f/\bar{\chi}_f$, as defined in Eq. (1). GR predicts no deviation on either parameter (vertical dashed line). Triangles mark the GWTC-2 medians, and vertical bars the symmetric 90%-credible intervals.

systematic errors arising from imperfect waveform modeling, we also produce results using the nonprecessing SEOBNRV4_ROM model, but these results exclude GW190412 and GW190814 due to the relative importance of HMs. Despite the differences between the two waveform approximants, the posteriors are in broad agreement, and we find no qualitative difference in the results (see Appendix B). This is in agreement with the expectation that systematic errors will be subdominant to statistical errors for the typical SNRs reported in GWTC-2 [137].

V. TESTS OF GRAVITATIONAL WAVE GENERATION

A. Generic modifications

Parametrized tests of GW generation allow us to quantify generic deviations from GR predictions. Such corrections could arise as modifications to the binding energy and angular momentum of the source, or as modifications to the energy and angular momentum flux, both leading to modified equations of motion. In this section, we focus on constraining deviations from GR by introducing parametric deformations to an underlying GR waveform model.

The early inspiral of compact binaries is well described by the PN approximation [74,75,91,143–151], a perturbative approach to solving the Einstein field equations in which we perform an expansion in terms of a small velocity parameter v/c. Once the intrinsic parameters of the binary are fixed, the coefficients at different orders of v/c in the PN series are uniquely determined. A consistency test of GR using the PN phase coefficients was first proposed in [18–21,23], and a general model independent parametrization was introduced in [22]. A Bayesian framework based on the general parametrization was introduced in [24–26], with subsequent extensions to the late-inspiral and post-inspiral coefficients being introduced in [27].

In order to constrain GR violations, we adopt two approaches. In the first approach, we directly constrain the analytical coefficients that describe the phase evolution of the IMRPHENOMPV2 waveform model [98–100]. The frequency-domain GW phase $\varphi(f)$ of IMRPHENOMPV2 can be broken down into three key regions: inspiral, intermediate, and merger–ringdown. The inspiral in IMRPHENOMPV2 is described by a PN expansion augmented with higher order pseudo-PN coefficients calibrated against EOB–NR hybrid waveforms. The PN phase evolution is written as a closed-form frequency domain expression by employing the stationary phase approximation. The intermediate and merger–ringdown regimes are described by analytical phenomenological expressions. The cutoff frequency f_c^{PAR} between the inspiral and intermediate region in IMRPHENOMPV2 is defined to be $GM(1+z)f_c^{\mathrm{PAR}}/c^3 = 0.018$, where z is the redshift and f_c^{PAR} is independent of the intrinsic parameters of the binary. We use p_i to collectively denote all of the inspiral $\{\varphi_i\}$ and postinspiral $\{\alpha_i, \beta_i\}$ parameters. The deviations from GR are expressed in terms of relative shifts $\delta\hat{p}_i$ in the waveform coefficients $p_i \rightarrow (1 + \delta\hat{p}_i)p_i$, which are introduced as additional free parameters to be constrained by the data.

The second approach [14] can apply modifications to the inspiral of any underlying waveform model, analytical or nonanalytical, by adding corrections that correspond to deformations of a given inspiral coefficient $\delta\hat{\varphi}_i$ at low frequencies and tapering the corrections to 0 at the cutoff frequency f_c^{PAR}. The second approach is applied to the nonanalytical model SEOBNRV4_ROM [152], a frequency-domain reduced-order model for the SEOBNRV4 waveform approximant [77]. There is a subtle difference in the way in which deviations from GR are introduced and parametrized in the two approaches. In the first approach, we directly constrain the fractional deviations in the non-spinning portion of the phase whereas in the second approach the fractional deviations are also applied to the spin sector. As in [15], the posteriors in the second approach are mapped post-hoc to the parametrization used in the first approach, consistent with previously presented results. See Sec. VII A for an SEOB-based analysis of the postmerger signal, interpreted in the context of studies of the remnant properties.

We constrain deviations from the PN phase coefficients predicted by GR using deviation parameters $\delta\hat{\varphi}_i$. Here i denotes the power of v/c beyond the leading order Newtonian contribution to the phase $\varphi(f)$. The frequency dependence of the phase coefficients is given by $f^{(i-5)/3}$, so that $\delta\hat{\varphi}_i$ quantifies deviations to the $i/2$ PN order. We constrain coefficients up to 3.5PN ($i = 7$), including terms that have a logarithmic dependence occurring at 2.5 and 3PN order. The nonlogarithmic term at 2.5PN ($i = 5$) cannot be constrained as it is degenerate with the coalescence phase. The coefficients describing deviations from GR were introduced in Eq. (19) of [24]. In addition, we include a coefficient at $i = -2$ corresponding to an effective -1PN term that, in some circumstances, can be interpreted as arising from the emission of dipolar radiation. The full set of inspiral parameters that we constrain is therefore

$$\{\delta\hat{\varphi}_{-2}, \delta\hat{\varphi}_0, \delta\hat{\varphi}_1, \delta\hat{\varphi}_2, \delta\hat{\varphi}_3, \delta\hat{\varphi}_4, \delta\hat{\varphi}_{5l}, \delta\hat{\varphi}_6, \delta\hat{\varphi}_{6l}, \delta\hat{\varphi}_7\}. \quad (4)$$

The inspiral deviations are expressed as shifts to the part of the PN coefficients with no spin dependence, φ_i^{NS}, i.e., $\varphi_i \rightarrow (1 + \delta\hat{\varphi}_i)\varphi_i^{\mathrm{NS}} + \varphi_i^{\mathrm{S}}$, where φ_i^{S} denotes the spin-dependent part of the aligned-spin PN coefficients. This is the same parametrization that has been previously used [5,6,13–15] and circumvents the potential singular behavior observed when the spin-dependent terms cancel with the non-spinning term. In GR, the coefficients occurring at -1PN and 0.5PN vanish, so we parametrize $\delta\hat{\varphi}_{-2}$ and $\delta\hat{\varphi}_1$ as *absolute* deviations, with a prefactor equal to the 0PN coefficient; all other coefficients represent *fractional*

deviations around the GR value. We derive constraints on the inspiral coefficients using the IMRPHENOMPV2 and SEOBNRV4_ROM analyses.

Besides the inspiral, the intermediate and merger–ringdown model in IMRPHENOMPV2 is analytic and allows for parametrized deviations of the phenomenological coefficients that describe these regimes, denoted by $\{\delta\hat{\beta}_2, \delta\hat{\beta}_3\}$ and $\{\delta\hat{\alpha}_2, \delta\hat{\alpha}_3, \delta\hat{\alpha}_4\}$ respectively. The parameters $\delta\hat{\beta}_i$ explicitly capture deformations in the NR calibrated coefficients β_i in the intermediate regime, whereas the parameters $\delta\hat{\alpha}_i$ describe deformations of the merger–ringdown coefficients α_i obtained from a mix of BH perturbation theory and calibration to NR [98,99]. We omit $\delta\hat{\alpha}_5$ as this occurs in the same term as $\delta\hat{\alpha}_4$, see Eq. (13) of [99], meaning that there will be a degree of degeneracy between the two coefficients.

As detailed in Sec. I, we consider all binaries that meet the significance threshold of FAR $< 10^{-3}$ yr^{-1} and impose the additional requirement that the SNR > 6 in the inspiral regime ($\delta\hat{\varphi}_i$) or postinspiral regime ($\delta\hat{\beta}_i$ and $\delta\hat{\alpha}_i$) respectively for an event to be included in the analyses, as data below these SNR thresholds fails to provide meaningful constraints. In contrast to the selection criteria used in [15], GW170818 meets the FAR threshold applied in this analysis and is included in the joint constraints. The SNRs and cutoff frequencies for all events are detailed in Table V.

For three of the events considered in this analysis, HMs have a nontrivial impact on parameter estimation and must be taken into account. This is the case for GW190412 and GW190814, which show evidence of detectable HM power [66,111], and for GW190521, which does not [82,83]. We perform the parametrized tests using IMRPHENOMPV3HM and, for GW190814, SEOBNRV4HM_ROM. By construction, parametrized deformations in IMRPHENOMPV3HM are propagated to the HMs through approximate rescalings of the (2, 2) mode with no new coefficients being introduced. The framework used for the SEOBNRV4HM_ROM analysis is extended to HMs in an analogous way. We show the posterior distributions for GW190412 and GW190814, the two events that show measurable HM power, in Appendix C.

We use LALINFERENCE to calculate the posterior probability distributions of the parameters characterizing the waveform [116]. The parametrization used here recovers GR in the limit $\delta\hat{p}_i \to 0$, enabling us to verify consistency with GR if the posteriors of $\delta\hat{p}_i$ have support at 0. As in previous analyses, we only allow the coefficients $\delta\hat{p}_i$ to vary one at a time. Despite the lack of generality, this approach is effective at detecting deviations from GR that do not just modify a single coefficient [27,153,154]. In particular, the coefficients will be sensitive to corrections that occur at generic PN orders even when varying a coefficient that corresponds to some fixed PN order [27,154]. Allowing the test to vary multiple coefficients simultaneously can often lead to posteriors that are less

TABLE V. Parametrized test event selection for all binaries meeting the FAR $< 10^{-3}$ yr^{-1} threshold. Here f_c^{PAR} denotes the cutoff frequency used to demarcate the division between the inspiral, and postinspiral regimes; ρ_{IMR}, ρ_{insp}, and ρ_{postinsp} are the *optimal* SNRs of the full signal, the inspiral, and postinspiral regions respectively. The last two columns denote if the event is included in parametrized tests on the inspiral (PI) and postinspiral (PPI) respectively. GW190814 is excluded due to the impact of HMs, see Appendix C.

Event	f_c^{PAR} [Hz]	ρ_{IMR}	ρ_{insp}	ρ_{postinsp}	PI	PPI
GW150914	50	24.7	9.6	22.8	✓	✓
GW151226	153	12.3	11.1	5.3	✓	⋯
GW170104	60	13.4	7.9	11.3	✓	✓
GW170608	179	15.8	14.8	6.3	✓	✓
GW170809	54	12.0	5.8	10.9	⋯	✓
GW170814	58	16.3	9.1	13.6	✓	✓
GW170818	48	10.8	4.5	10.1	⋯	✓
GW170823	40	11.5	4.2	11.1	⋯	✓
GW190408_181802	68	15.0	8.3	12.5	✓	✓
GW190412	83	19.1	15.1	11.8	✓	✓
GW190421_213856	36	10.4	2.9	10.0	⋯	✓
GW190503_185404	39	13.7	4.3	13.0	⋯	✓
GW190512_180714	87	12.8	10.5	7.4	✓	✓
GW190513_205428	48	13.3	5.1	12.2	⋯	✓
GW190517_055101	41	11.1	3.4	10.5	⋯	✓
GW190519_153544	23	15.0	0.0	15.0	⋯	✓
GW190521	14	13.9	0.0	13.9	⋯	✓
GW190521_074359	40	25.4	9.7	23.5	✓	✓
GW190602_175927	22	13.1	0.0	13.1	⋯	✓
GW190630_185205	50	16.3	8.1	14.1	✓	✓
GW190706_222641	19	12.7	0.0	12.7	⋯	✓
GW190707_093326	161	13.4	12.2	5.5	✓	⋯
GW190708_232457	103	13.7	11.1	8.0	✓	✓
GW190720_000836	126	10.5	9.2	5.2	✓	⋯
GW190727_060333	35	12.3	2.0	12.0	⋯	✓
GW190728_064510	157	12.6	11.4	5.3	✓	⋯
GW190814	137	24.8	22.3	10.9	✓	✓
GW190828_063405	45	16.2	6.0	15.1	✓	✓
GW190828_065509	80	9.9	6.3	7.6	✓	✓
GW190910_112807	35	14.4	3.3	14.0	⋯	✓
GW190915_235702	46	13.1	3.7	12.6	⋯	✓
GW190924_021846	239	12.2	11.8	3.4	✓	⋯

informative, with the single-coefficient templates often being preferred to the templates with multiple parameters in the context of Bayesian model selection [153]. Varying multiple coefficients simultaneously would therefore not improve the efficiency of detecting violations of GR [153]. On the other hand, nontrivial multicoefficient deviations may be detected even when only one $\delta\hat{p}_i$ is allowed to vary at a time [51]. We adopt uniform priors on $\delta\hat{p}_i$ that are symmetric about zero. Due to the way in which parametrized deformations are implemented, evaluating a model in certain regions of the parameter space can lead to pathologies and unphysical effects. This can result in multimodal posterior distributions or other systematic errors; see the discussion in Appendix C.
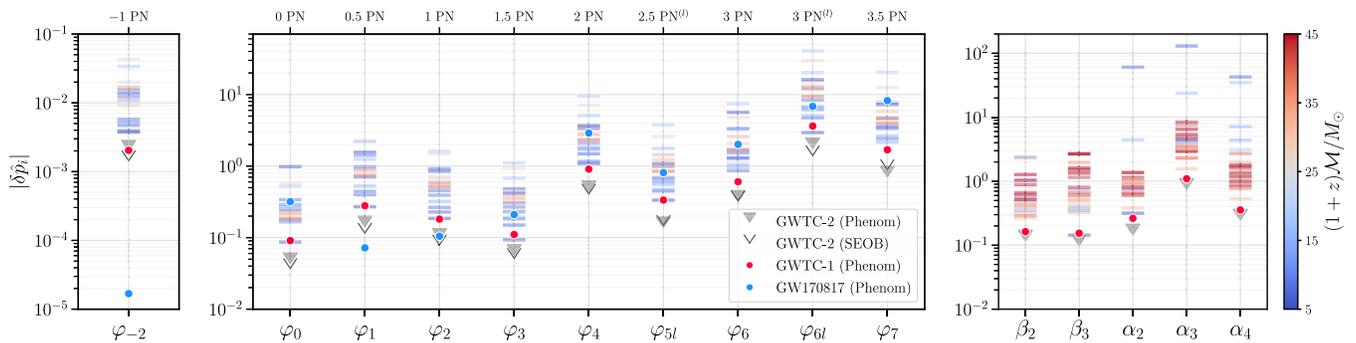
FIG. 5. 90% upper bounds on the absolute magnitude of the GR violating parameters $\delta\hat{p}_i$. The left and middle panels show the -1PN through 3.5PN inspiral coefficients, while the right panel shows the postinspiral coefficients $\{\delta\hat{\beta}_i, \delta\hat{\alpha}_i\}$. Constraints obtained from individual events with IMRPHENOMPV2 are represented by horizontal stripes, colored by the median redshifted chirp mass $(1+z)\mathcal{M}$, inferred assuming GR. Gray triangles (black wedges) mark the constraints obtained with IMRPHENOMPV2 (SEOBNRV4_ROM) when all GWTC-2 events are combined assuming a shared deviation from GR. For reference, we show the equivalent results for GWTC-1 (IMRPHENOMPV2) and the individual constraints from GW170817 (IMRPHENOMPV2_NRTIDAL), as red and blue circles respectively.

In Fig. 5 we show the 90% upper bounds on the absolute magnitude of the GR violating coefficients, $|\delta\hat{p}_i|$. The individual bounds are colored by the mean redshifted chirp mass, $(1+z)\mathcal{M}$, as inferred assuming GR (Table I). The results for GWTC-2 include all new BBHs reported in [16] plus the BBHs reported in GWTC-1 [17], combined by assuming a shared value of the coefficient across events (i.e., by multiplying the individual likelihoods). Whilst the combined results for GWTC-1 and GWTC-2 do not include the two BNS events, GW170817 and GW190425, in Fig. 5 we show the results for GW170817 separately for comparison to previously published results [14].

We broadly see that lighter binaries contribute prominently to our constraint on the inspiral coefficients and heavier binaries drive the constraints on the postinspiral coefficients. This is to be expected as more (less) of the inspiral moves into the sensitivity of the detectors as we decrease (increase) the mass and we suppress (enhance) the SNR in the postinspiral. For all coefficients, bar the -1PN and 0.5PN terms, the joint-likelihood bounds determined using GWTC-1 and GWTC-2 BBHs improve on all previous constraints [14,15]. The tightest bounds on the -1PN and 0.5PN coefficients come from GW170817, which improves on the GWTC-2 BBH constraints by a factor of 120 and 2.2 respectively. We find that the combined GWTC-2 results improve on the GWTC-1 constraints by a factor ~1.9 for the inspiral coefficients and ~1.4 for the postinspiral coefficients respectively. This improvement is broadly consistent with the factor expected from the increased number of events, $\sqrt{17/5} \approx 1.8$ for the inspiral and $\sqrt{26/7} \approx 1.9$ for the postinspiral respectively. Neglecting the -1PN coefficient, we find that the 0PN term is the best constrained parameter, $|\delta\hat{\varphi}_0| \lesssim 4.4 \times 10^{-2}$. However, this bound is weaker than the 90% upper bound inferred from the orbital-period derivative $\dot{P}_{orb}$ of the double pulsar J0737–3039 by a factor ~3 [2,155].

Although all results from individual events offer support for the GR value, a small fraction of them contain $\delta\hat{p}_i = 0$ only in the tails. This is the case for some of the coefficients for GW190519_153544, GW190521_074359, GW190814, GW190828_065509, and GW190924_021846. Yet, given the large number of events and coefficients analyzed, this is not surprising: for GR signals in Gaussian noise, we would expect on average approximately 1 out of 10 independent trials to return $\delta\hat{p}_i = 0$ outside the 90%-credible level just from statistical fluctuations.

To evaluate the set of measurements holistically, we produce the population-marginalized distributions for each parameter $\delta\hat{p}_i$ following the method described in Sec. III B; the result is the filled distributions in Fig. 6. These distributions represent our best knowledge of the possible values of the $\delta\hat{p}_i$'s from all LIGO–Virgo BBHs with FAR $< 10^{-3}$ yr^{-1} to date. For comparison, Fig. 6 also shows the joint likelihoods obtained by restricting the deviation to be the same for all events (unfilled black distributions), which were used to derive the combined GWTC-2 constraints in Fig. 5.

All population-marginalized distributions are consistent with GR, with $\delta\hat{p}_i = 0$ lying close to the median for most parameters, and always within the 90% credible symmetric interval. The medians, 90% credible intervals, and GR quantiles $Q_{GR} = P(\delta\hat{p}_i < 0)$ of these distributions are presented in Table VI, together with equivalent quantities for the joint-likelihood approach. A value of Q_{GR} significantly different from 50% indicates that the null hypothesis falls in the tails of the distribution. The quantiles may also be directly translated into z-scores defined by $z_{GR} = \Phi^{-1}(Q_{GR})$, where Φ^{-1} is the inverse cumulative distribution function for a standard normal random variable. The z-score encodes the distance of the posterior mean away from zero in units of standard deviation (discussed below).
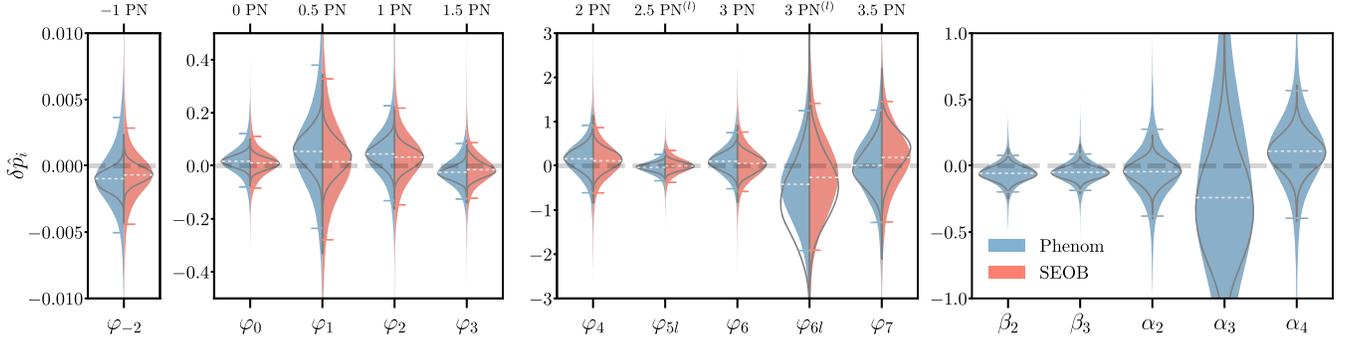
FIG. 6. Combined GWTC-2 BBH results for parametrized violations of GR obtained from the designated events in Table V, for each deviation parameter $\delta\hat{p}_i$ (abscissa). The probability densities shown in color represent the population-marginalized expectation, Eq. (1), obtained from a hierarchical analysis allowing independent GR deviations for each event. In contrast, the unfilled black distributions result from restricting all events to share a common value of each parameter. Phenom (SEOB) results were obtained with IMRPHENOMPV2 (SEOBNRV4_ROM) and are shown in blue (red); the $\{\beta_i, \alpha_i\}$ coefficients are not probed with SEOB, as they are intrinsic to Phenom waveforms. For the hierarchical results, error bars denote symmetric 90%-credible intervals and a white dashed line marks the median. The dashed horizontal line at $\delta\hat{p}_i = 0$ highlights the expected GR value.

TABLE VI. Results from parametrized tests of GW generation (Sec. V A). Combined constraints on each deviation parameter $\delta\hat{p}_i$ from the full set of GWTC-2 BBH measurements using the IMRPHENOMPV2 or SEOBNRV4_ROM waveforms, as indicated by P or S respectively in the second column. The general constraints do not assume the deviation takes the same value for all events and are summarized by the hyperdistribution mean μ and standard deviation σ, as well as the inferred direct constraint on $\delta\hat{p}_i$ (defined in Sec. III B). The restricted constraints assume a common value of the parameter shared by all events and are summarized by the constraint on $\delta\hat{p}_i$. All quantities represent the median and 90%-credible intervals excepting σ, for which we provide an upper limit. For both general and restricted results, Q_{GR} is the GR quantile associated with Fig. 6.

$\hat{p}_i$	WF	General				Restricted	
		μ	σ	$\delta\hat{p}_i$	Q_{GR}	$\delta\hat{p}_i$	Q_{GR}
φ_{-2} $_{[\times 20]}$	P	$-0.02^{+0.04}_{-0.03}$	<0.08	$-0.02^{+0.09}_{-0.08}$	68%	$-0.02^{+0.02}_{-0.02}$	93%
	S	$-0.01^{+0.03}_{-0.03}$	<0.07	$-0.01^{+0.07}_{-0.07}$	67%	$-0.01^{+0.02}_{-0.02}$	85%
φ_0	P	$0.02^{+0.05}_{-0.04}$	<0.09	$0.02^{+0.10}_{-0.10}$	33%	$0.02^{+0.04}_{-0.03}$	20%
	S	$0.01^{+0.04}_{-0.04}$	<0.09	$0.01^{+0.10}_{-0.09}$	40%	$0.01^{+0.04}_{-0.03}$	35%
φ_1	P	$0.06^{+0.14}_{-0.13}$	<0.27	$0.05^{+0.32}_{-0.29}$	33%	$0.07^{+0.10}_{-0.11}$	15%
	S	$0.02^{+0.14}_{-0.13}$	<0.28	$0.02^{+0.31}_{-0.29}$	45%	$0.03^{+0.11}_{-0.10}$	29%
φ_2	P	$0.05^{+0.09}_{-0.09}$	<0.17	$0.04^{+0.18}_{-0.18}$	28%	$0.04^{+0.07}_{-0.07}$	14%
	S	$0.03^{+0.08}_{-0.08}$	<0.17	$0.03^{+0.18}_{-0.18}$	34%	$0.03^{+0.06}_{-0.06}$	22%
φ_3	P	$-0.02^{+0.05}_{-0.05}$	<0.10	$-0.02^{+0.11}_{-0.10}$	69%	$-0.03^{+0.04}_{-0.04}$	90%
	S	$-0.02^{+0.05}_{-0.05}$	<0.09	$-0.01^{+0.10}_{-0.11}$	62%	$-0.02^{+0.05}_{-0.04}$	71%
φ_4	P	$0.14^{+0.44}_{-0.41}$	<0.72	$0.16^{+0.76}_{-0.77}$	33%	$0.17^{+0.36}_{-0.36}$	22%
	S	$0.11^{+0.38}_{-0.38}$	<0.66	$0.11^{+0.75}_{-0.73}$	37%	$0.14^{+0.33}_{-0.36}$	26%
φ_{5l}	P	$-0.03^{+0.15}_{-0.15}$	<0.27	$-0.04^{+0.29}_{-0.30}$	61%	$-0.02^{+0.12}_{-0.15}$	65%
	S	$-0.01^{+0.16}_{-0.18}$	<0.33	$-0.00^{+0.35}_{-0.37}$	50%	$-0.02^{+0.15}_{-0.15}$	52%
φ_6	P	$0.10^{+0.32}_{-0.32}$	<0.56	$0.10^{+0.64}_{-0.62}$	36%	$0.08^{+0.30}_{-0.27}$	30%
	S	$0.06^{+0.34}_{-0.31}$	<0.59	$0.05^{+0.71}_{-0.63}$	43%	$0.05^{+0.30}_{-0.33}$	41%
φ_{6l}	P	$-0.41^{+1.07}_{-1.01}$	<1.27	$-0.42^{+1.67}_{-1.50}$	69%	$-0.80^{+1.32}_{-1.29}$	84%
	S	$-0.28^{+1.04}_{-1.08}$	<1.39	$-0.26^{+1.68}_{-1.65}$	62%	$-0.47^{+1.17}_{-1.14}$	75%
φ_7	P	$0.02^{+0.70}_{-0.75}$	<1.09	$0.01^{+1.25}_{-1.29}$	49%	$-0.08^{+0.75}_{-0.66}$	56%
	S	$0.18^{+0.68}_{-0.69}$	<1.25	$0.19^{+1.27}_{-1.46}$	37%	$0.38^{+0.63}_{-0.81}$	21%
β_2	P	$-0.06^{+0.07}_{-0.08}$	<0.12	$-0.06^{+0.14}_{-0.14}$	79%	$-0.07^{+0.08}_{-0.07}$	90%
β_3	P	$-0.05^{+0.08}_{-0.08}$	<0.12	$-0.05^{+0.14}_{-0.14}$	76%	$-0.05^{+0.07}_{-0.06}$	90%
α_2	P	$-0.04^{+0.13}_{-0.15}$	<0.30	$-0.04^{+0.32}_{-0.33}$	61%	$-0.04^{+0.11}_{-0.13}$	73%
α_3	P	$-0.23^{+0.65}_{-0.56}$	<1.10	$-0.24^{+1.36}_{-1.19}$	64%	$-0.32^{+0.62}_{-0.55}$	80%
α_4	P	$0.11^{+0.22}_{-0.23}$	<0.44	$0.11^{+0.46}_{-0.51}$	30%	$0.10^{+0.19}_{-0.22}$	21%

In terms of the overall magnitude of the allowed fractional deviations, the parameter constrained most tightly by the hierarchical analysis is $\delta\hat{\varphi}_{-2} = -0.97^{+4.62}_{-4.07} \times 10^{-3}$, within 90% credibility. On the other hand, the loosest constraint comes from $\delta\hat{\varphi}_{6l} = -0.42^{+1.67}_{-1.50}$, also within 90% credibility. In both cases, however, the null-hypothesis lies close to the median, with $\mathcal{Q}_{\mathrm{GR}} = 68\%$ and $\mathcal{Q}_{\mathrm{GR}} = 69\%$ respectively. The magnitude of the constraint, however, is parametrization-dependent and may not be meaningful outside the context of a specific theory [7,22,156].

Agreement with GR requires not only that the distributions in Fig. 6 support $\delta\hat{p}_i = 0$, but also that the measured hyperparameters be consistent with $\mu = \sigma = 0$ (see Sec. III B). This is indeed the case, as can be inferred from the 90% credible measurements shown in Fig. 7, and summarized in the third and fourth columns of Table VI. The implications of the hyperparameter measurement are concisely captured by the two-dimensional GR quantile $\mathcal{Q}_{\mathrm{GR}}$, defined as the isoprobability contour passing through $\mu = \sigma = 0$: a posterior with $\mathcal{Q}_{\mathrm{GR}} = 0$ peaks at the GR expectation, with larger values indicating reduced support.
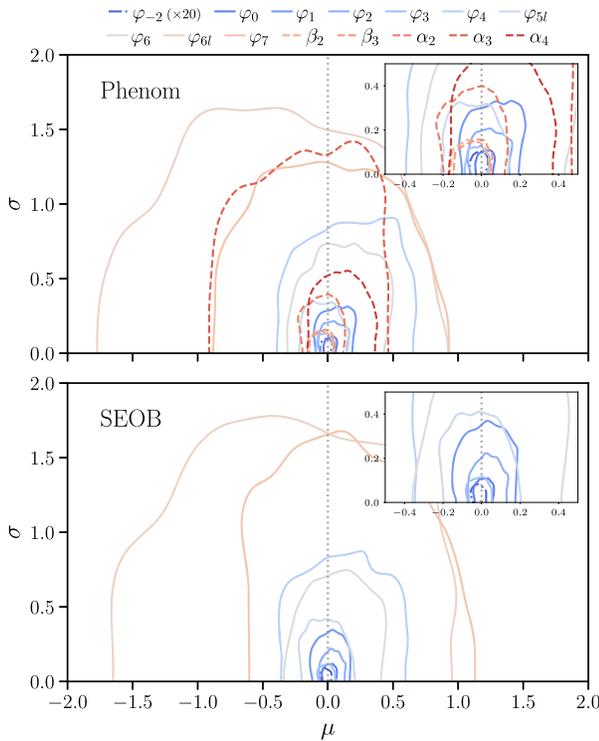
FIG. 7. Hyperparameter measurements for the parametrized-deviation coefficients. Contours enclose 90% of the posterior probability for the μ and σ hyperparameters corresponding to each of the $\delta\hat{p}_i$ coefficients, as indicated by the legend. The top (bottom) panel shows IMRPHENOMPV2 (SEOBNRV4_ROM) results, corresponding to the blue (red) distributions in Fig. 6. The insets provides a closer look around $\mu = \sigma = 0$, our baseline expectation in the absence of GR violations or measurement systematics; all contours enclose this point. As in Table VI, the values for φ_{-2} have been rescaled by a factor of 20 for ease of display.

Figure 8 summarizes the main conclusions from this section through a visualization of z_{GR} and $\mathcal{Q}_{\mathrm{GR}}$ from the hierarchical analysis (top and middle), and of z_{GR} from the joint-likelihood analysis (bottom). Each $\delta\hat{p}_i$ is represented by a vertical stripe, with the postmerger $\{\delta\hat{\beta}_i, \delta\hat{\alpha}_i\}$ coefficients identified by an additional circle. The figure suggests that the postmerger parameters may behave distinctly from the rest, tending to show more pronounced excursions away from the baseline expectation ($z_{\mathrm{GR}} \approx 0$). In any case, because 1σ outliers are not unlikely and the null hypothesis lies well within the 90% credible regions for all coefficients (Table VI), we conclude that there is no statistically significant evidence for GR violations.

The results from this section can be used to place constraints on individual theories by reinterpreting the coefficients $\delta\hat{\varphi}_i$ within the parametrized post-Einstein (ppE) framework given a theory-dependent mapping [7,22]. Recently, [49] used the coefficients $\delta\hat{\varphi}_i$ to place constraints on higher-curvature theories in the small-coupling approximation, focusing on two specific examples: Einstein-dilaton-Gauss–Bonnet and dynamical Chern-Simons gravity. The improved constraints on the coefficients $\delta\hat{\varphi}_i$ provided here will allow for tighter constraints on the coupling constants in such theories under similar (non-trivial) assumptions.

B. Spin-induced quadrupole moment

The leading order spin-induced multipole moment, the spin-induced quadrupole moment, is a measure of the degree of an object's oblateness due to its spin, specifically of its effect on the surrounding gravitational field [157–159]. If the object is in an inspiraling binary, this effect will become imprinted in the GW waveform at specific PN orders,
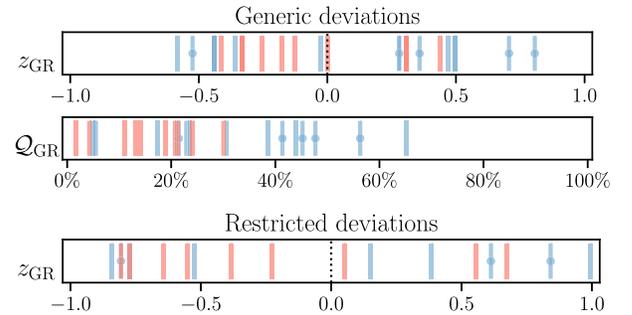

FIG. 8. Figures of merit for the GWTC-2 parametrized tests results. Each vertical stripe corresponds to a given $\delta\hat{p}_i$ as estimated using IMRPHENOMPV2 (blue) or SEOBNRV4_ROM (red); circles identify the postmerger coefficients $\{\delta\hat{\alpha}_i, \delta\hat{\beta}_i\}$. The top two strips summarize the hierarchical results for generic deviations across events: the z-score for $\delta\hat{p}_i = 0$, z_{GR}, and the two-dimensional quantile for the hyperparameters $\mu = \sigma = 0$, $\mathcal{Q}_{\mathrm{GR}}$. The bottom strip shows an equivalent z-score obtained by restricting to identical deviations across events. The generic (restricted) z-scores correspond to the filled (unfilled) distributions in Fig. 6, and $\mathcal{Q}_{\mathrm{GR}}$ to those in Fig. 7.

helping us identify the object's nature and composition [160]. For a compact object with mass m and spin χ, the spin-induced quadrupole moment is given by

$$Q = -\kappa\chi^2 m^3, \tag{5}$$

where κ is the spin-induced quadrupole moment coefficient, which depends on the equation of state, mass, and spin of the compact object. Due to the no-hair conjecture [161–163], κ is unity for BHs in GR, while it may take a range of values for neutron stars or BH mimickers [157–159,164]. For example, depending upon the equation of state, the value of κ can vary between ~ 2 and ~ 14 for a spinning neutron star [165–167], and between ~ 10 and ~ 150 for slowly spinning boson stars [81,168–170]. The spin-induced quadrupole moments first appear along with the self-spin terms in the GW phasing formula as a 2PN leading-order effect [157]. In this paper, we also incorporate 3PN corrections to the GW phase due to the spin-induced quadrupole moment of binary components [145,171]. As shown in [172], the measurement accuracy of these parameters is largely correlated with masses and spins of the binary system. Despite the degeneracy, the presence of spin terms at other PN orders as well as the nonspinning PN coefficients help to break the correlations of κ with spins and mass parameters, permitting its measurement for spinning binary systems. It has been demonstrated in the past that it is possible to measure spin-induced multipole moments for intermediate mass-ratio [173,174] and extreme mass-ratio inspirals [175,176]. This parameter can also be constrained through electromagnetic observations of active galactic nuclei (see [177] for a recent measurement) and supermassive BHs [178].

In principle, the BH nature of the binary components can be probed by measuring their individual spin-induced quadrupole moment coefficients κ_1 and κ_2, parametrized as deviations away from unity $\delta\kappa_1$ and $\delta\kappa_2$. However, for the stellar-mass compact binaries accessible to LIGO and Virgo, it is often difficult to simultaneously constrain $\delta\kappa_1$ and $\delta\kappa_2$ due to the strong degeneracies between these and other binary parameters, like the spins and masses [160,179]. We define the symmetric and antisymmetric combinations of the individual deviation parameters as $\delta\kappa_s = (\delta\kappa_1 + \delta\kappa_2)/2$ and $\delta\kappa_a = (\delta\kappa_1 - \delta\kappa_2)/2$, but in this analysis we restrict $\delta\kappa_a = 0$, implying $\delta\kappa_1 = \delta\kappa_2 = \delta\kappa_s$. The assumption $\delta\kappa_a = 0$ also demands that the two compact objects be of the same kind which holds well when both the objects are BHs. For non-BH binaries, this restriction leads to stronger implications, requiring the two compact objects to have similar masses and equation of state as $\delta\kappa_1$ and $\delta\kappa_2$ are functions of these. Having a non-BH compact object in the binary will violate these restrictions, which could lead to systematic biases in the estimation of $\delta\kappa_s$. For non-BBH signals, the value of $\delta\kappa_s$ would be offset from zero, given the definition, and it is

unlikely for such offsets to be completely compensated by the aforementioned systematics. Therefore, the posteriors of $\delta\kappa_s$ for non-BBH signals will tend to peak away from zero, hinting at the presence of an exotic compact object.

For a more general test of BBH nature, one might also include effects such as the tidal deformations that arise due to the object's binary companion [180–182] and tidal heating [183–188] along with the spin-induced deformations. The present test does not consider these effects but focuses only on spin-induced deformations.

We perform this analysis on the compact binaries observed in O1, O2 and O3a. Though the spin-induced effects for non-BH compact objects are not modeled beyond the inspiral phase, as a null test of BBH nature, the analysis was performed by including the full inspiral, merger, and ringdown phases, using a waveform model built on IMRPHENOMPV2. In this model, only the inspiral phase of the waveform (defined as in Sec. V A) is modified in terms of $\delta\kappa_1$ and $\delta\kappa_2$. For GW190412, which showed evidence of HMs [111], we employed a waveform model built on IMRPHENOMPV3HM with the same modifications in terms of $\delta\kappa_1$ and $\delta\kappa_2$ as for the model based on IMRPHENOMPV2. We apply this test only to the events in Table I that have SNR of 6 or more in the inspiral phase under the GR BBH assumption (same threshold as in Table V); we apply the same criteria to the GWTC-1 events. In this paper, we do not apply this test on GW190814 as the outcome of the test on GW190814 has already been discussed in [66], and we have not gained any new insights since then.

We employ a uniform prior on $\delta\kappa_s$ in the range $[-500, 500]$. The prior limits at ± 500 were chosen so they safely encompass the known models of BH mimickers, including gravastars and other exotic objects that may have $\delta\kappa_s < 0$ [164]. As elsewhere in this paper, the $\delta\kappa_s$ constraints apply exclusively to the set of events analyzed and do not preclude the existence of objects with $|\delta\kappa_s|$ high enough to be missed by our search pipelines [81].

Figure 9 shows the measurement of $\delta\kappa_s$ from individual events. We find that $\delta\kappa_s$ is poorly constrained for the majority of events, which can be attributed to the low spin of these events [16]. From Eq. (5), it is clear that the quadrupole moment vanishes when the spins are zero, irrespective of the value of κ. Therefore, any meaningful upper limit on κ would require the lower limit on at least one of the spin magnitudes to exclude zero. If this condition is not met, the posteriors of $\delta\kappa_s$ would rail against the priors in this analysis. The dependence of the upper limit of κ on the spin magnitudes was studied in [172]. In Fig. 9, we highlight the events with the most concentrated $\delta\kappa_s$ posteriors, with a sample standard deviation $\sigma_{\delta\kappa_s} < 150$: GW151226, GW190412, GW190720_000836, and GW190728_064510. We do not quote symmetric credible intervals from individual events, since all of the posteriors
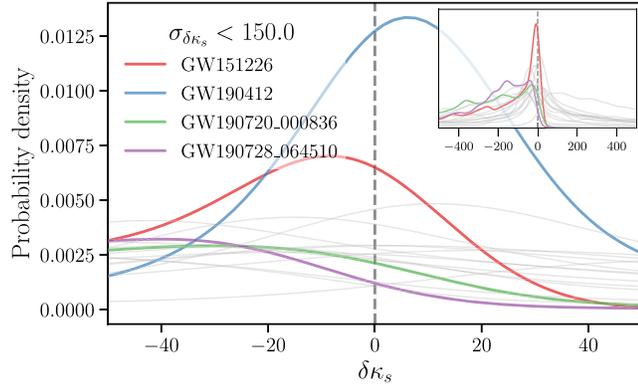
FIG. 9. Posterior probability distribution on the spin-induced quadrupole moment parameter $\delta\kappa_s$ from the GWTC-2 events listed in the SIM column of Table I. We highlight GW151226, GW190412, GW190720_000836, and GW190728_064510, as they yield the tightest distributions (with standard deviation $\sigma_{\delta\kappa_s} < 150$); other events are shown in gray. The inset expands the plot range to the full range of the prior, removing GW190412 to facilitate display of the other events. The vertical dashed line at $\delta\kappa_s = 0$ marks the Kerr BBH expectation.

FIG. 10. Combined measurement on the spin-induced quadrupole moment parameter $\delta\kappa_s$ from the set of all of events in Fig. 9. The red curve (restricted) represents the posterior obtained assuming $\delta\kappa_s$ takes the same value for all events. The blue histogram (generic) was obtained by hierarchically combining events without that assumption, as in Eq. (1). Dotted lines bound symmetric 90%-credible intervals, $\delta\kappa_s = -23.2^{+52.2}_{-62.4}$ ($\delta\kappa_s = -15.2^{+15.9}_{-19.0}$) for the generic (restricted) case. The Kerr BBH value ($\delta\kappa_s = 0$) is marked by a dashed line.

present tails reaching the edge of the prior on at least one side.

We may narrow down the scope of the test by focusing on the $\delta\kappa_s > 0$ region of our prior, which is well constrained by a subset of the events. Doing so is well motivated in the context of neutron stars [158,165,166] and specific BH mimickers such as boson stars [168] for which $\kappa_s > 1$. Restricting to positive $\delta\kappa_s$, the two events providing the tightest upper limits are GW151226 and GW190412, with 90% credible bounds of $\delta\kappa_s < 11.33$ and $\delta\kappa_s < 110.89$ respectively.

Figure 10 shows the distributions on $\delta\kappa_s$ obtained by considering all the events collectively. Though most of the individual signals yielded poor constraints, the set is not completely uninformative: as can be seen from Fig. 9, most of the posteriors have markedly stronger support in regions close to zero, even though they extend to the edge of the prior. This is reflected by the combined results of Fig. 10, which disfavor large values of $|\delta\kappa_s|$. The blue histogram represents the population-marginalized posterior obtained without assuming a unique value of $\delta\kappa_s$ across events, using the hierarchical approach of Sec. III B. With 90% credibility, this analysis determines $\delta\kappa_s = -23.2^{+52.2}_{-62.4}$, which indicates that the events considered are consistent with a population dominated by Kerr BBHs (within the given uncertainty). The distribution hyperparameters are also consistent with the null-hypothesis ($\mu = \sigma = 0$), with $\mu = -24.6^{+30.7}_{-35.3}$ and $\sigma < 52.7$. Both μ and the population-marginalized posterior of Fig. 10 inherit the asymmetry of the individual events, which tend to be skewed towards $\delta\kappa_s < 0$ (cf. inset in Fig. 9); this suggests that negative values of $\delta\kappa_s$ are harder to constrain. Conditional on

positive values, the generic population results constrain $\delta\kappa_s < 59.97$.

The red curve in Fig. 10 represents the joint-likelihood posterior obtained by restricting κ_s to take the same value for all the events. Under that assumption, we find $\delta\kappa_s = -15.2^{+15.9}_{-19.0}$ and, conditional on positive values, $\delta\kappa_s < 9.01$. The hypothesis that all of the events considered are Kerr BBHs ($\delta\kappa_s = 0$) is preferred over an alternative proposal that all of them are not with a shared $\delta\kappa_s \neq 0$, with a log Bayes factor of $\log_{10}\mathcal{B}^{\text{Kerr}}_{\delta\kappa_s \neq 0} = 1.1$, or log Bayes factor of $\log_{10}\mathcal{B}^{\text{Kerr}}_{\delta\kappa_s \geq 0} = 2.0$ if only allowing $\delta\kappa_s \geq 0$.

VI. TESTS OF GRAVITATIONAL WAVE PROPAGATION

In GR, GWs far from their source propagate along null geodesics, with energy E and momentum p related by the dispersion relation $E^2 = p^2c^2$, where c is the speed of light. Extensions to GR may violate this in several ways, e.g., by endowing the graviton with a mass. To probe generalized dispersion relations, we adopt the common phenomenological modification to GR introduced in [189] and applied to LIGO and Virgo data in [8,15],

$$E^2 = p^2c^2 + A_\alpha p^\alpha c^\alpha, \qquad (6)$$

where A_α and α are phenomenological parameters, and GR is recovered if $A_\alpha = 0$ for all α. To leading order, Eq. (6) may encompass a variety of predictions from different extensions to GR [7,189–195]; this includes massive gravity for $\alpha = 0$ and $A_\alpha > 0$, with a graviton mass $m_g = A_0^{1/2}c^{-2}$ [190]. As in [15], we consider α values from 0 to 4

TABLE VII.   Results for the modified dispersion analysis (Sec. VI). The table shows 90%-credible upper bounds on the graviton mass m_g and the absolute value of the modified dispersion relation parameter A_α, as well as the GR quantiles Q_{GR}. The $<$ and $>$ labels denote the upper bound on $|A_\alpha|$ when assuming $A_\alpha < 0$ and > 0, respectively, and $\bar{A}_\alpha = A_\alpha/eV^{2-\alpha}$ is dimensionless. Rows compare the GWTC-1 results from [15] to the GWTC-2 results.

m_g	$\|\bar{A}_0\|$			$\|\bar{A}_{0.5}\|$			$\|\bar{A}_1\|$			$\|\bar{A}_{1.5}\|$			$\|\bar{A}_{2.5}\|$			$\|\bar{A}_3\|$			$\|\bar{A}_{3.5}\|$			$\|\bar{A}_4\|$		
	$<$	$>$	Q_{GR}	$<$	$>$	Q_{GR}	$<$	$>$	Q_{GR}	$<$	$>$	Q_{GR}	$<$	$>$	Q_{GR}	$<$	$>$	Q_{GR}	$<$	$>$	Q_{GR}	$<$	$>$	Q_{GR}
[10^{-23} eV/c^2]	[10^{-45}]		[%]	[10^{-38}]		[%]	[10^{-32}]		[%]	[10^{-26}]		[%]	[10^{-14}]		[%]	[10^{-8}]		[%]	[10^{-2}]		[%]	[10^4]		[%]
GWTC-1 4.70	7.99	3.39	79	1.17	0.70	73	2.51	1.21	70	6.96	3.70	86	5.05	8.01	28	2.94	3.66	25	2.01	3.73	35	1.44	2.34	34
GWTC-2 1.76	1.75	1.37	66	0.46	0.28	66	1.00	0.52	79	3.35	1.47	83	1.74	2.43	31	1.08	2.17	17	0.76	1.57	12	0.64	0.88	25

in steps of 0.5, excluding $\alpha = 2$, which is degenerate with an overall time delay. A nonzero A_α manifests itself in the data as a frequency-dependent dephasing of the GW signal, which builds up as the wave propagates towards Earth and hence increases with the source comoving distance, potentially enhancing weak GR deviations. The analysis makes use of a modified version of the IMRPHENOMPV2 waveform (checks for systematics using SEOBNRV4HM_ROM were presented in [15]). We use Eq. (3) of [15] to compute the dephasing for a given A_α.[5] This expression was derived in [189] by treating waves emitted at a given time as particles that travel at the particle velocity $v_p = pc^2/E$ associated with the wave's instantaneous frequency. Different dephasings can arise from different prescriptions, e.g., using the group velocity instead, but the corresponding bound on A_α can be obtained by rescaling with an appropriate factor in most cases. See discussions after Eq. (5) in [15] for details.

We assume priors flat in A_α except when reporting the mass of the graviton, where we use a prior flat in that quantity. We analyze 31 events from GWTC-2 satisfying our FAR threshold (see Sec. II and Table I).[6] Since we can take A_α and m_g to be universal parameters, results from different events can be easily combined by multiplying the individual likelihoods. Although we only discuss the overall combined results here, individual-event posteriors are available in [53], as for other tests.

We show our results in Table VII and Figs. 11 and 12. Table VII and Fig. 11 present constraints on the allowed amount of dispersion through the 90%-credible upper limits on $|A_\alpha|$, computed separately for $A_\alpha > 0$ and $A_\alpha < 0$. There is noticeable improvement when combining

GWTC-2 results with respect to the previous result in [15]. This is the case for both positive and negative amplitudes, meaning that we are more tightly constraining these quantities closer to the nondispersive, GR prediction ($A_\alpha = 0$). The average improvement in the $|A_\alpha|$ upper limits relative to [15] is a factor 2.6, although this fluctuates slightly across choices of α. Overall, this is consistent with the factor of $\sqrt{31/7} \approx 2.1$ naively expected from the increase in the number of events analyzed.[7]

Upper limits on the A_α parameters can be uncertain due to the difficulty in accurately sampling the long tails of the posteriors. To quantify this uncertainty, we follow a Bayesian bootstrapping procedure [196], as done previously in [8,15], with 2000 bootstrap realizations for each value of α and sign of A_α. We find that the average width of the 90%-credible interval of the individual-event upper limits is a factor of 0.12 of the reported upper limit itself; i.e., the average uncertainty in the upper limit is 0.12. Out of all upper limits, nine carry fractional uncertainties larger than 0.5. The most uncertain upper limit is that for GW190828_065509 and $A_4 < 0$, with a fractional uncertainty of 1.7.

Figure 12 shows the overall posterior obtained for negative and positive values of A_α. The enhanced stringency of our measurements relative to our previous GWTC-1 results is also visible here, as seen in the smaller size of the blue violins with respect to the gray, and the fact that the medians (blue circles) are generally closer to the GR value. The latter is also manifested in the GR quantiles $Q_{GR} = P(A_\alpha < 0)$ in Table VII, which tend to be closer to 50% ($Q_{GR} = 50\%$ implies the distribution is centered on the GR value).

From our combined GWTC-2 data, we bound the graviton mass to be $m_g \leq 1.76 \times 10^{-23}$ eV/c^2, with 90% credibility (Table VII). This represents an improvement of a factor of 2.7 relative to [15]. The new measurement is 1.8 times more stringent than the most recent Solar System bound of 3.16×10^{-23} eV/c^2, also with 90% credibility [197].

---

[5]There was a typographic error in Eq. (4) of Ref. [15]: the $1/(\alpha - 2)$ exponent should instead be $1/(2 - \alpha)$.

[6]We do not consider GW190521 because we were unable to obtain well-converged results for that event without using HMs, which are not yet implemented for this test. We have analyzed GW190412 and GW190814 without HMs, despite evidence that HMs contribute to those signals. However, we have checked that this does not bias the results through an injection study for GW190412 and $\alpha = 0$. We have also confirmed that excluding GW190412 and GW190814 would affect the combined results in Table I by only $\sim$5% on average (12% in the worst case).

[7]We have analyzed eight events from GWTC-1, one more than for the combined results in [15] because those excluded GW170818.
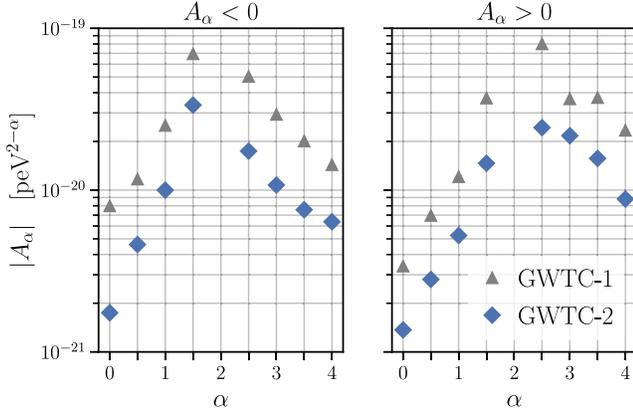
FIG. 11.   90% credible upper bounds on the absolute value of the modified dispersion relation parameter A_α. The upper limits are derived from the distributions in Fig. 12, treating the positive and negative values of A_α separately. Picoelectronvolts provide a convenient scale because 1 peV $\simeq h \times 250$ Hz, where 250 Hz is close to the most sensitive frequencies of the LIGO and Virgo instruments. Marker style distinguishes the new GWTC-2 results from the previous GWTC-1 results in [15].
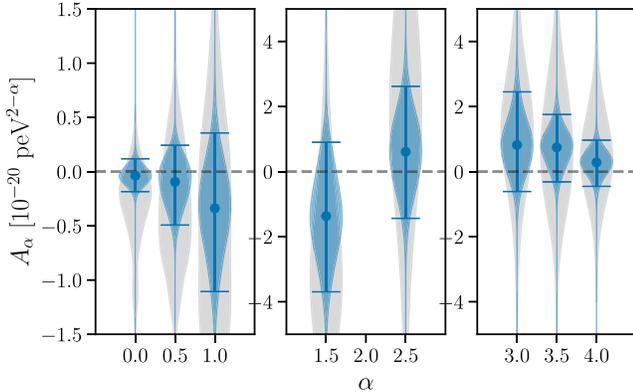

FIG. 12.   Violin plots of the full posteriors on the modified dispersion relation parameter A_α calculated from the GWTC-2 events (blue), with the 90% credible interval around the median indicated. For comparison, we also show the GWTC-1 previous measurement (gray), reported in [15].

VII. REMNANT PROPERTIES

A. Ringdown

In GR, the remnant object resulting from the coalescence of two astrophysical BHs is a perturbed Kerr BH. This remnant BH will gradually relax to its Kerr stationary state by emitting GWs corresponding to a specific set of characteristic quasinormal modes (QNMs), whose frequency f and damping time τ depend solely on the BH mass M_f and the dimensionless spin χ_f. This last stage of the coalescence is known as *ringdown*. The description of the ringdown stage is based on the final state conjecture [198–201] stating that the physical spectrum of QNMs is

exclusively determined by the final BH mass and spin (the no-hair conjecture [162,202–208]) and that the Kerr solution is an attractor of BH spacetimes in astrophysical scenarios.[8]

By analyzing the postmerger signal from a BBH coalescence independently of the preceding inspiral, we can verify the final state conjecture, test the nature of the remnant object (complementary to the searches for GW echoes discussed in Sec. VII B), and estimate directly the remnant mass and spin assuming it is a Kerr BH—which, in turn, allows us to test GR's prediction for the energy and angular momentum emitted during the coalescence (complementary to the IMR consistency test discussed in Sec. IV B, and the postinspiral parameters in Sec. V A). This set of analyses is referred to as *BH spectroscopy* [122,123,212–221]. Unlike the IMR consistency test, a ringdown-only analysis is not contaminated by frequency mixing with other phases of the signal, and it does not require a large amount of SNR in the inspiral regime (the lack of such SNR is why the IMR consistency test was unable to be applied to GW190521 [82,83], for instance).

The complex-valued GW waveform during ringdown can be expressed as a superposition of damped sinusoids,

$$
\begin{aligned}
h_+(t) - ih_\times(t) = \sum_{\ell=2}^{+\infty} \sum_{m=-\ell}^{+\ell} \sum_{n=0}^{+\infty} \mathcal{A}_{\ell mn} \exp\left[-\frac{t - t_0}{(1 + z)\tau_{\ell mn}}\right] \\
\times \exp\left[\frac{2\pi i f_{\ell mn}(t - t_0)}{1 + z}\right]_{-2}S_{\ell mn}(\theta, \phi, \chi_f),
\end{aligned}
\tag{7}
$$

where z is the cosmological redshift, and the (ℓ, m, n) indices label the QNMs. The angular multipoles are denoted by ℓ and m, while n orders modes of a given (ℓ, m) by decreasing damping time. The frequency and the damping time for each ringdown mode can be computed for a perturbed isolated BH as a function of its mass M_f and spin χ_f [222–225]. For each (ℓ, m, n), there are in principle two associated frequencies and damping times: those for a *prograde* mode, with $\mathrm{sgn}(f_{\ell mn}) = \mathrm{sgn}(m)$, and those for a *retrograde* mode, with $\mathrm{sgn}(f_{\ell mn}) \neq \mathrm{sgn}(m)$—retrograde modes are not expected to be relevant [214], so we do not include them in Eq. (7). The frequency and damping time of the $+|m|$ mode are related to those of the $-|m|$ mode by $f_{\ell mn} = -f_{\ell-mn}$ and $\tau_{\ell mn} = \tau_{\ell-mn}$ for $m \neq 0$. The complex amplitudes $\mathcal{A}_{\ell mn}$ characterize the excitation and the phase of each ringdown mode at a reference time t_0, which for a BBH merger can be predicted from numerical simulations [226–228]. In general, $\mathcal{A}_{\ell mn}$ is independent of $\mathcal{A}_{\ell-mn}$.

---

[8]In principle such frequencies and damping times would also depend on the electric charge of the remnant BH. However, for astrophysically relevant scenarios the BH charge is expected to be negligible [209–211].

The angular dependence of the GW waveform is contained in the spin-weighted spheroidal harmonics $_{-2}S_{\ell mn}(\theta, \phi, \chi_{\mathrm{f}})$, where θ, ϕ are the polar and azimuthal angles in a frame centered on the remnant BH and aligned with its angular momentum. We approximate these functions through the spin-weighted spherical harmonics $_{-2}Y_{\ell m}(\theta, \phi)$, which introduces mode-mixing between QNMs with the same m index but different ℓ indices [229–231]. Except in one case, as indicated below, models in this section do not account for this effect. However, mode-mixing is expected to be negligible for the modes we consider, in particular for the dominant $\ell = |m| = 2$ moments of the radiation [229–231].

We present results from two approaches: a time-domain ringdown analysis PYRING [122,123] and a parametrized version of an aligned-spin EOB waveform model with HMs called PSEOBNRV4HM [105,218].

1. The PYRING analysis

The PYRING analysis infers the remnant BH parameters based on the ringdown part of a signal alone. The analysis is completely formulated in the time domain [122,123] for both the likelihood function and waveform templates, hence avoiding spectral leakage from previous stages of the coalescence as would arise in a frequency-domain analysis when Fourier transforming a template with an abrupt start [122,123,232]. We employ four different waveform templates, each constructed with different sets of assumptions in order to obtain agnostic measurements of the QNM frequencies and damping times, and to explore the contribution of modes other than the least damped mode ($n = 0$).

The Kerr$_{220}$ template corresponds to the $\ell = |m| = 2, n = 0$ contribution (i.e., the 220 mode) of Eq. (7), where the frequencies and damping times are predicted as a function of $(M_{\mathrm{f}}, \chi_{\mathrm{f}})$ by GR, while the complex amplitudes are kept as free parameters. The remnant mass and spin were sampled with uniform priors. The Kerr$_{221}$ template is similar to Kerr$_{220}$ but incorporates the first overtone ($n = 1$) for $\ell = |m| = 2$ in addition to the fundamental mode. We do not consider a higher number of overtones since they are not expected to be relevant at current sensitivity [123,233–235]. Uniform priors on the remnant mass and spin were also adopted.

The Kerr$_{\mathrm{HM}}$ template includes all fundamental prograde modes with $\ell \leq 4$, with the angular dependence parametrized using spin-weighted spherical harmonics, taking into account mode-mixing [228]. NR fits are used to compute amplitudes as a function of the initial binary parameters, and frequencies and damping times as a function of the remnant parameters where both the initial binary parameters and the remnant parameters are sampled independently with uniform priors.

We use as a reference time t_0, which is chosen based on an estimate of the peak of the strain $(h_+^2 + h_\times^2)$ from the full

IMR analyses assuming GR.[9] When overtones ($n > 0$) are included in a template, we fit the data starting at t_0 itself [123,233], while in all other cases we start the fit $10GM_{\mathrm{f}}(1 + z)/c^3$ after t_0, which is when the least damped mode is expected to dominate the signal. The sky locations and start times at each detector are released in [53].

We analyze all the GWTC-2 BBHs and report results for those events where the remnant parameters were constrained compared to the adopted prior bounds, and for which the Bayesian evidence favors the presence of a signal over pure Gaussian noise when using our most sensitive template (Kerr$_{221}$). Estimates of the remnant parameters obtained through the three waveform templates (Kerr$_{220}$, Kerr$_{221}$, and Kerr$_{\mathrm{HM}}$) are reported in Table VIII. Fitting the data at an earlier time increases the SNR available when using this template, which is reflected in tighter constraints of the remnant parameters as shown in Table VIII for the Kerr$_{221}$ template. In all cases the estimated remnant quantities from the three waveform templates agree with the corresponding GR predictions coming from the full IMR analyses [16]. For GW190521, the results reported in [82,83] are not identical to the ones reported here as the previous analyses did not include the negative-m mode, and we have updated to use a more precise value for the reference time. The lower frequency cutoff for this event was also changed from 20 Hz to 11 Hz. None of the conclusions previously reported for GW190521 are affected by these small changes.

We use log Bayes factors to quantify the contribution of overtones or HMs during ringdown. In Table VIII, we report the log Bayes factors $\log_{10} \mathcal{B}_{220}^{\mathrm{HM}}$ comparing a fit with all modes in Kerr$_{\mathrm{HM}}$, versus one with only the $\ell = |m| = 2$, $n = 0$ mode; this computation provides no strong evidence for the presence of HMs. We also present the log Bayes factors $\log_{10} \mathcal{B}_{220}^{221}$ comparing the results obtained when fitting the full postmerger signal using the $n = 0, 1$ modes against the template including the $n = 0$ mode only, with both templates starting at the reference time t_0. The data show evidence for the presence of overtones only for loud signals (for example GW190521_074359 shows such evidence), although in all cases estimates of the remnant parameters tend to get closer to the full IMR waveform estimates when including overtones.

To achieve a test of the final state conjecture and quantify the level of agreement with GR, we modify the Kerr$_{221}$ template to allow for fractional deviations in the frequency and damping time with respect to their GR predictions for the 221 mode (the first overtone). Meanwhile, the frequency and the damping time of the better-measured 220

---

[9]For events in O1 and O2, the waveform approximant used in the full IMR analyses was SEOBNRV4_ROM. As for events in O3a, the waveform approximant used in the full IMR analyses was IMRPHENOMPV2, except for GW190521, where NRSUR7DQ4 was used instead.

TABLE VIII. The median, and symmetric 90%-credible intervals, of the redshifted final mass and final spin, inferred from the full IMR analysis (IMR) and the PYRING analysis with three different waveform models (Kerr$_{220}$, Kerr$_{221}$, and Kerr$_{HM}$). The estimates using different models are consistent with each other within 90% credibility. We quantify the contribution of the HMs using log Bayes factors $\log_{10} \mathcal{B}^{HM}_{220}$, where a positive value reflects the presence of HMs in the data. Similarly, we quantify the contribution of the first overtone using log Bayes factors $\log_{10} \mathcal{B}^{221}_{220}$, where a positive value reflects the presence of the first overtone in the data. We also quantify the level of agreement with GR for each event using log odds ratios $\log_{10} \mathcal{O}^{modGR}_{GR}$ comparing the generic modified-GR hypothesis with GR. The catalog-combined log odds ratio is slightly negative (−0.70), and the log odds ratios for individual events are also inconclusive, showing no evidence that the Kerr metric is insufficient.

| Event | Redshifted final mass $(1+z)M_f [M_\odot]$ | | | | Final spin χ_f | | | | Higher modes | Overtones | |
	IMR	Kerr$_{220}$	Kerr$_{221}$	Kerr$_{HM}$	IMR	Kerr$_{220}$	Kerr$_{221}$	Kerr$_{HM}$	$\log_{10} \mathcal{B}^{HM}_{220}$	$\log_{10} \mathcal{B}^{221}_{220}$	$\log_{10} \mathcal{O}^{modGR}_{GR}$
GW150914	$68.8^{+3.6}_{-3.1}$	$62.7^{+19.0}_{-12.1}$	$71.7^{+13.2}_{-12.5}$	$80.3^{+20.1}_{-21.7}$	$0.69^{+0.05}_{-0.04}$	$0.52^{+0.33}_{-0.44}$	$0.69^{+0.18}_{-0.36}$	$0.83^{+0.13}_{-0.45}$	0.03	0.63	−0.34
GW170104	$58.5^{+4.6}_{-4.1}$	$56.2^{+19.1}_{-11.6}$	$61.3^{+16.7}_{-13.2}$	$104.3^{+207.7}_{-43.1}$	$0.66^{+0.08}_{-0.11}$	$0.26^{+0.42}_{-0.24}$	$0.51^{+0.34}_{-0.44}$	$0.59^{+0.34}_{-0.51}$	0.26	−0.20	−0.23
GW170814	$59.7^{+3.0}_{-2.3}$	$46.1^{+133.0}_{-33.6}$	$56.6^{+20.9}_{-11.1}$	$171.2^{+268.7}_{-143.5}$	$0.72^{+0.05}_{-0.07}$	$0.52^{+0.42}_{-0.47}$	$0.47^{+0.40}_{-0.42}$	$0.54^{+0.41}_{-0.48}$	0.04	−0.19	−0.11
GW170823	$88.8^{+11.2}_{-10.2}$	$73.8^{+26.8}_{-23.7}$	$79.0^{+21.3}_{-13.2}$	$103.0^{+133.1}_{-46.7}$	$0.72^{+0.09}_{-0.12}$	$0.46^{+0.40}_{-0.41}$	$0.36^{+0.38}_{-0.32}$	$0.74^{+0.22}_{-0.61}$	0.02	−0.98	−0.07
GW190408_181802	$53.0^{+3.2}_{-3.4}$	$22.4^{+253.0}_{-11.1}$	$46.6^{+18.8}_{-10.9}$	$127.4^{+327.7}_{-107.6}$	$0.67^{+0.06}_{-0.07}$	$0.45^{+0.45}_{-0.40}$	$0.36^{+0.46}_{-0.33}$	$0.46^{+0.47}_{-0.41}$	−0.05	−1.02	−0.02
GW190512_180714	$43.5^{+4.0}_{-2.8}$	$37.6^{+48.9}_{-22.4}$	$36.7^{+19.3}_{-24.8}$	$99.4^{+247.6}_{-66.5}$	$0.65^{+0.07}_{-0.07}$	$0.41^{+0.47}_{-0.37}$	$0.45^{+0.40}_{-0.39}$	$0.77^{+0.20}_{-0.66}$	0.09	−0.42	0.03
GW190513_205428	$70.6^{+11.5}_{-6.7}$	$55.5^{+31.5}_{-42.1}$	$68.5^{+28.2}_{-11.8}$	$88.7^{+250.0}_{-41.9}$	$0.68^{+0.14}_{-0.12}$	$0.38^{+0.48}_{-0.34}$	$0.31^{+0.53}_{-0.28}$	$0.59^{+0.34}_{-0.52}$	0.09	−0.54	−0.05
GW190519_153544	$146.8^{+14.7}_{-15.4}$	$120.7^{+39.7}_{-21.5}$	$125.9^{+24.3}_{-21.7}$	$155.4^{+84.4}_{-42.5}$	$0.79^{+0.07}_{-0.13}$	$0.42^{+0.41}_{-0.36}$	$0.52^{+0.25}_{-0.40}$	$0.70^{+0.21}_{-0.50}$	0.21	−0.00	−0.11
GW190521	$256.6^{+36.6}_{-30.4}$	$282.2^{+50.0}_{-61.9}$	$284.0^{+40.4}_{-43.9}$	$299.3^{+57.7}_{-62.4}$	$0.71^{+0.12}_{-0.16}$	$0.76^{+0.14}_{-0.38}$	$0.78^{+0.10}_{-0.22}$	$0.80^{+0.13}_{-0.30}$	0.12	−0.86	−0.50
GW190521_074359	$88.0^{+4.3}_{-4.8}$	$83.0^{+24.0}_{-17.2}$	$86.4^{+14.1}_{-14.8}$	$105.9^{+20.8}_{-26.4}$	$0.72^{+0.05}_{-0.07}$	$0.57^{+0.31}_{-0.49}$	$0.67^{+0.17}_{-0.34}$	$0.87^{+0.09}_{-0.39}$	−0.04	1.29	−0.27
GW190602_175927	$163.8^{+20.7}_{-18.3}$	$156.4^{+71.4}_{-30.6}$	$160.0^{+37.4}_{-31.2}$	$261.7^{+84.4}_{-91.5}$	$0.70^{+0.10}_{-0.14}$	$0.34^{+0.41}_{-0.31}$	$0.46^{+0.39}_{-0.49}$	$0.79^{+0.14}_{-0.49}$	0.61	−1.56	0.32
GW190706_222641	$171.1^{+20.0}_{-23.7}$	$136.0^{+52.0}_{-29.3}$	$152.5^{+37.8}_{-28.4}$	$184.0^{+139.2}_{-55.8}$	$0.78^{+0.09}_{-0.18}$	$0.41^{+0.42}_{-0.37}$	$0.55^{+0.31}_{-0.45}$	$0.68^{+0.26}_{-0.54}$	−0.06	−0.64	−0.45
GW190708_232457	$34.4^{+2.7}_{-0.7}$	$28.9^{+285.4}_{-17.9}$	$32.3^{+15.0}_{-12.2}$	$171.9^{+307.6}_{-147.8}$	$0.69^{+0.04}_{-0.04}$	$0.47^{+0.45}_{-0.42}$	$0.34^{+0.44}_{-0.31}$	$0.43^{+0.51}_{-0.39}$	−0.11	−0.17	−0.02
GW190727_060333	$99.2^{+10.7}_{-9.8}$	$78.7^{+45.7}_{-66.4}$	$88.8^{+25.7}_{-16.0}$	$107.4^{+112.1}_{-42.7}$	$0.73^{+0.10}_{-0.10}$	$0.53^{+0.42}_{-0.47}$	$0.45^{+0.39}_{-0.41}$	$0.71^{+0.24}_{-0.59}$	−0.02	−1.65	−0.40
GW190828_063405	$75.7^{+6.0}_{-5.2}$	$71.2^{+35.8}_{-55.5}$	$69.6^{+22.0}_{-17.3}$	$99.0^{+166.0}_{-49.1}$	$0.75^{+0.06}_{-0.07}$	$0.72^{+0.25}_{-0.62}$	$0.65^{+0.27}_{-0.55}$	$0.92^{+0.06}_{-0.74}$	0.05	−0.72	−0.05
GW190910_112807	$97.0^{+9.3}_{-7.1}$	$112.2^{+32.0}_{-31.7}$	$107.7^{+28.6}_{-27.4}$	$137.1^{+59.5}_{-31.4}$	$0.70^{+0.08}_{-0.07}$	$0.76^{+0.18}_{-0.55}$	$0.75^{+0.17}_{-0.46}$	$0.91^{+0.07}_{-0.27}$	−0.10	−0.64	−0.40
GW190915_235702	$74.8^{+7.9}_{-7.4}$	$38.3^{+335.1}_{-27.4}$	$63.0^{+19.1}_{-9.9}$	$137.3^{+324.1}_{-96.2}$	$0.70^{+0.09}_{-0.11}$	$0.52^{+0.43}_{-0.46}$	$0.27^{+0.40}_{-0.24}$	$0.55^{+0.39}_{-0.49}$	0.06	−0.37	−0.04

mode remain the same as their GR predictions as functions of the remnant mass M_f and spin χ_f to help constrain the remnant properties. This approach, compared to allowing for deviations in the fundamental mode, has the advantage of lowering the impact of priors on the remnant mass and spin recovery, as well as the impact of correlations among the deviation parameters and the remnant parameters. We sample over the regular Kerr parameters and the fractional deviations with uniform priors in the $[-1, 1]$ range for the frequency $\delta\hat{f}_{221}$ and in the $[-0.9, 1]$ range for the damping time $\delta\hat{\tau}_{221}$.[10] The posteriors on the fractional deviations quantify the agreement of the 221 mode with the Kerr prediction.

Additionally, we may follow [24,25,216] to compute a log odds ratio $\log_{10}\mathcal{O}_{\mathrm{GR}}^{\mathrm{modGR}}$ for deviations from the Kerr ringdown. We define the baseline GR hypothesis $\mathcal{H}_{\mathrm{GR}}$ to be the proposition that both the fractional deviation parameters vanish, i.e., $\delta\hat{f}_{221} = \delta\hat{\tau}_{221} = 0$. Similarly, we define the modified GR hypothesis $\mathcal{H}_{\mathrm{modGR}}$ to be the proposition that *at least one* of the fractional deviation parameters is nonzero, with the priors above. We may construct $\mathcal{H}_{\mathrm{modGR}}$ from three subhypotheses, which we label $\mathcal{H}_{\delta\hat{f}_{221}}$, $\mathcal{H}_{\delta\hat{\tau}_{221}}$, and $\mathcal{H}_{\delta\hat{f}_{221},\delta\hat{\tau}_{221}}$. For $\mathcal{H}_{\delta\hat{f}_{221}}$, we write the frequencies and damping times for the 220 and the 221 mode as

$$\mathcal{H}_{\delta\hat{f}_{221}} \equiv \begin{cases} f_{220} = f_{220}^{\mathrm{GR}}(M_f,\chi_f) \\ \tau_{220} = \tau_{220}^{\mathrm{GR}}(M_f,\chi_f) \\ f_{221} = f_{221}^{\mathrm{GR}}(M_f,\chi_f)(1+\delta\hat{f}_{221}) \\ \tau_{221} = \tau_{221}^{\mathrm{GR}}(M_f,\chi_f) \end{cases}, \quad (8)$$

where the "GR" superscript indicates the Kerr value corresponding to a given M_f and χ_f. Similarly, for $\mathcal{H}_{\delta\hat{\tau}_{221}}$, we write the frequencies and damping times for the 220 and the 221 mode as

$$\mathcal{H}_{\delta\hat{\tau}_{221}} \equiv \begin{cases} f_{220} = f_{220}^{\mathrm{GR}}(M_f,\chi_f) \\ \tau_{220} = \tau_{220}^{\mathrm{GR}}(M_f,\chi_f) \\ f_{221} = f_{221}^{\mathrm{GR}}(M_f,\chi_f) \\ \tau_{221} = \tau_{221}^{\mathrm{GR}}(M_f,\chi_f)(1+\delta\hat{\tau}_{221}) \end{cases}. \quad (9)$$

Finally, for $\mathcal{H}_{\delta\hat{f}_{221},\delta\hat{\tau}_{221}}$, we again write the frequencies and damping times as

$$\mathcal{H}_{\delta\hat{f}_{221},\delta\hat{\tau}_{221}} \equiv \begin{cases} f_{220} = f_{220}^{\mathrm{GR}}(M_f,\chi_f) \\ \tau_{220} = \tau_{220}^{\mathrm{GR}}(M_f,\chi_f) \\ f_{221} = f_{221}^{\mathrm{GR}}(M_f,\chi_f)(1+\delta\hat{f}_{221}) \\ \tau_{221} = \tau_{221}^{\mathrm{GR}}(M_f,\chi_f)(1+\delta\hat{\tau}_{221}) \end{cases}, \quad (10)$$

allowing deviations in both frequency and damping time of the 221 mode simultaneously.

If we assign equal prior weight to both the GR and modified-GR hypotheses, then the odds ratio is

$$\mathcal{O}_{\mathrm{GR}}^{\mathrm{modGR}} = \frac{1}{3}(\mathcal{B}_{\mathrm{GR}}^{\delta\hat{f}_{221}} + \mathcal{B}_{\mathrm{GR}}^{\delta\hat{\tau}_{221}} + \mathcal{B}_{\mathrm{GR}}^{\delta\hat{f}_{221},\delta\hat{\tau}_{221}}). \quad (11)$$

The log odds ratios $\log_{10}\mathcal{O}_{\mathrm{GR}}^{\mathrm{modGR}}$ are reported in Table VIII for each event. Among all the events considered, GW190602_175927 has the highest $\log_{10}\mathcal{O}_{\mathrm{GR}}^{\mathrm{modGR}}$ with a value of 0.32, which is not statistically significant. We also find a catalog-combined log odds ratio of -0.70, in favor of the GR hypothesis that the Kerr metric is sufficient to describe the observed ringdown signals.

Figure 13 shows both the 1D marginal and the joint posterior distributions for $\delta\hat{f}_{221}$ and $\delta\hat{\tau}_{221}$ obtained from individual GW events where we allow both the frequency and the damping time of the 221 mode to deviate from the GR predictions (i.e., the $\mathcal{H}_{\delta\hat{f}_{221},\delta\hat{\tau}_{221}}$ hypothesis). We only show results from GW events where the data prefer the waveform model with both the fundamental and the first overtone ($n = 0, 1$) modes over the model with only the $n = 0$ fundamental mode with $\log_{10}\mathcal{B}_{220}^{221} > 0$. The measurements show consistency with GR for the frequency. As for the damping time, it is essentially unconstrained, except for events with low SNR in the ringdown (such as GW190727_060333) where the posterior distribution of $\delta\hat{\tau}_{221}$ rails towards the lower prior bound -0.9, as the data show little evidence of the first overtone. The results broadly agree with previous analyses for GW150914 [123], although the truncation time chosen here ($t_0 = 1126259462.42335$ GPS in Hanford) is slightly later than in [5,123]. A hierarchical analysis of the set of measurements using all 17 events constrains the frequency deviations to $\delta\hat{f}_{221} = 0.04_{-0.32}^{+0.27}$, in agreement with the Kerr hypothesis. The hierarchical analysis is uninformative for $\delta\hat{\tau}_{221}$ within the prior bounds considered.

Finally, as another test of the consistency of the ringdown signals with GR, we use a template which consists of a single damped sinusoid to fit the data, where the frequency, damping time, and complex amplitude are considered as free parameters without imposing any predictions from GR. This means that, for this template, we assume neither that the remnant object is a Kerr BH, nor that it originated from a BBH coalescence. We place uniform priors on the frequency, damping time, log of the magnitude, and the phase of the complex amplitude. The frequency and damping time obtained by fitting this

---

[10]The lower prior bound on the damping time deviation is set by the discrete analysis time resolution.
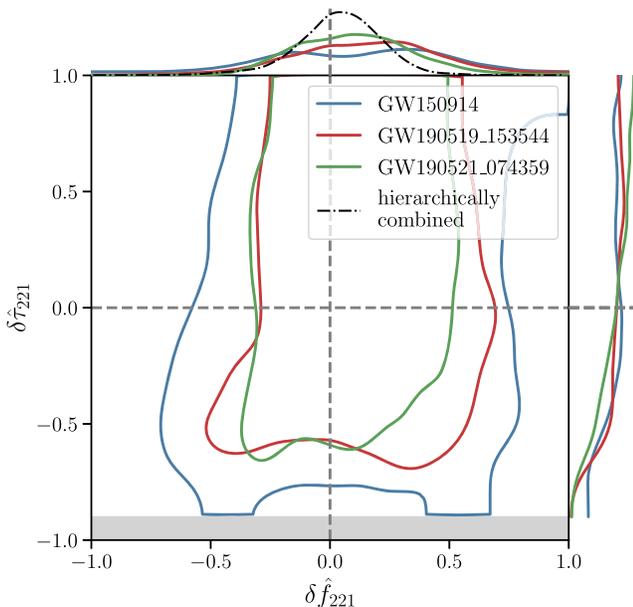
FIG. 13. The 90% credible region of the joint posterior distribution of the fractional deviations of the frequency $\delta\hat{f}_{221}$ and the damping time $\delta\hat{\tau}_{221}$, and their marginalized posterior distributions, for the $\ell = |m| = 2, n = 1$ mode from the PYRING analysis, where we allow both the frequency and the damping time of the 221 mode to deviate from the GR predictions. Here we show measurements from individual events where the data prefer the waveform model with both the fundamental and the first overtone ($n = 0, 1$) modes over the model with only the $n = 0$ fundamental mode. The measurements of the fractional deviation of the frequency from individual events, and as a set of measurements (using all 17 events), both show consistency with GR. The fractional deviation of the damping time is mostly unconstrained.

template to the data are shown in Table IX, where we report 90% credible intervals from the marginalized posteriors for each of these two parameters. The values show good agreement with the results from full IMR analyses where GR is assumed, except for GW170814, GW190512_180714, GW190828_063405, and GW190910_112807, where the estimates of the damping time from the PYRING analysis are higher than the estimates from the full IMR analyses. Nevertheless, in all these cases the contours of the 90% credible region in the frequency-damping time space from the two analyses actually do overlap. We observed that events with low SNR in the ringdown often show overestimations of the damping time with respect to the median value obtained using the full IMR waveform. To assess whether the overestimation is caused by detector noise fluctuations, we injected simulated IMR waveforms with parameters consistent with GW190828_063405, close to the coalescence time of the event. The injections show a similar behavior to what was observed in the actual event, with three out of ten injections having the injected

value lying outside the 90% credible interval of the damping time. The same injections performed in a zero noise configuration instead always have the posterior distributions of the damping time peaking at the injected value, suggesting that the overestimation of the damping time is associated with the detector noise fluctuations.

2. The PSEOBNRV4HM *analysis*

The PSEOBNRV4HM ringdown analysis uses a parametrized version of a spinning EOB waveform model with HMs, calibrated on nonprecessing binaries [105,218]. The analysis uses the frequency-domain likelihood function while the waveform model is constructed in the time domain. In this model the effective frequency and damping time of the 220 mode are written in terms of fractional deviations from their nominal GR values: $f_{220} = f_{220}^{\mathrm{GR}}(1 + \delta\hat{f}_{220})$ and $\tau_{220} = \tau_{220}^{\mathrm{GR}}(1 + \delta\hat{\tau}_{220})$ [218], where $\delta\hat{f}_{220}$ and $\delta\hat{\tau}_{220}$ are estimated directly from the data using the parameter inference techniques described in Sec. III, and $f_{220}^{\mathrm{GR}}, \tau_{220}^{\mathrm{GR}}$ are computed using the mass and spin of the BH remnant as determined by NR fits reported in [105].

We performed this analysis only on O3a events with a median redshifted total mass $> 90\, M_{\odot}$ since this analysis is computationally expensive, and we expect these events to give the best measurements among all the O3a events. Table IX shows the redshifted effective frequency f_{220} and the redshifted effective damping time τ_{220} of the 220 mode inferred from this analysis.

The frequency and the damping time inferred from the PSEOB analysis are also in good agreement with the full IMR measurements that assume GR, except for GW190521, GW190727_060333, and GW190910_112807 where the estimates of the damping time from the PSEOB analysis are higher than the estimates from the full IMR analyses. Nevertheless, in all these cases the 2D 90% credible regions do overlap. In order to better understand this issue, we investigated possible biases due to properties of the detector noise. We injected a set of simulated numerical relativity signals with parameters consistent with GW190521 into real data immediately adjacent to the event, and ran the PSEOB analysis on them. For three out of five injections around the event we recover posteriors that overestimate the damping time and for which the injected GR value lies outside the 90% credible interval, suggesting that the overestimation of the damping time for GW190521 is a possible artifact of noise fluctuations. A similar study was conducted with PYRING using the damped sinusoid model for GW190828_063405, and we also observed overestimations of the damping time. This suggests that the overestimation of the damping time is a common systematic error for low-SNR signals.

In Fig. 14, we show the 90% credible region of the joint posterior distribution of the frequency and damping time deviations, as well as their respective marginalized

TABLE IX. The median value and symmetric 90% credible interval of the redshifted frequency and damping time estimated using the full IMR analysis (IMR), the PYRING analysis with a single damped sinusoid (DS), and the PSEOBNRV4HM analysis (pSEOB).

Event	Redshifted frequency [Hz]			Redshifted damping time [ms]		
	IMR	DS	pSEOB	IMR	DS	pSEOB
GW150914	248^{+8}_{-7}	247^{+14}_{-16}	$\cdots$	$4.2^{+0.3}_{-0.2}$	$4.8^{+3.7}_{-1.9}$	$\cdots$
GW170104	287^{+15}_{-25}	228^{+71}_{-102}	$\cdots$	$3.5^{+0.4}_{-0.3}$	$3.6^{+36.2}_{-2.1}$	$\cdots$
GW170814	293^{+11}_{-14}	527^{+340}_{-332}	$\cdots$	$3.7^{+0.3}_{-0.2}$	$25.1^{+22.2}_{-19.0}$	$\cdots$
GW170823	197^{+17}_{-17}	222^{+664}_{-62}	$\cdots$	$5.5^{+1.0}_{-0.8}$	$13.4^{+31.8}_{-9.8}$	$\cdots$
GW190408_181802	319^{+11}_{-20}	504^{+479}_{-459}	$\cdots$	$3.2^{+0.3}_{-0.3}$	$10.0^{+32.5}_{-8.9}$	$\cdots$
GW190421_213856	162^{+14}_{-14}	$\cdots$	171^{+50}_{-16}	$6.3^{+1.2}_{-0.8}$	$\cdots$	$8.5^{+5.3}_{-4.2}$
GW190503_185404	191^{+17}_{-15}	$\cdots$	265^{+501}_{-79}	$5.3^{+0.8}_{-0.8}$	$\cdots$	$3.5^{+3.4}_{-1.8}$
GW190512_180714	381^{+33}_{-42}	220^{+686}_{-42}	$\cdots$	$2.6^{+0.2}_{-0.2}$	$26.1^{+21.3}_{-22.9}$	$\cdots$
GW190513_205428	241^{+26}_{-28}	250^{+493}_{-88}	$\cdots$	$4.3^{+1.1}_{-0.4}$	$5.3^{+19.2}_{-3.8}$	$\cdots$
GW190519_153544	127^{+9}_{-9}	123^{+11}_{-19}	124^{+12}_{-13}	$9.5^{+1.7}_{-1.5}$	$9.7^{+9.0}_{-3.8}$	$10.3^{+3.6}_{-3.1}$
GW190521	68^{+4}_{-4}	65^{+3}_{-3}	67^{+2}_{-2}	$15.8^{+3.9}_{-2.5}$	$22.1^{+12.4}_{-7.4}$	$30.7^{+7.7}_{-7.4}$
GW190521_074359	198^{+7}_{-7}	197^{+15}_{-15}	205^{+12}_{-12}	$5.4^{+0.4}_{-0.4}$	$7.7^{+6.4}_{-3.3}$	$5.3^{+1.5}_{-1.2}$
GW190602_175927	105^{+10}_{-9}	93^{+13}_{-22}	99^{+15}_{-15}	$10.0^{+2.0}_{-1.4}$	$10.0^{+17.2}_{-4.5}$	$8.8^{+5.4}_{-3.6}$
GW190706_222641	108^{+11}_{-10}	109^{+7}_{-12}	112^{+7}_{-8}	$10.9^{+2.4}_{-2.2}$	$20.4^{+25.2}_{-12.9}$	$19.4^{+7.2}_{-8.9}$
GW190708_232457	497^{+10}_{-46}	642^{+279}_{-596}	$\cdots$	$2.1^{+0.2}_{-0.1}$	$24.6^{+23.0}_{-22.6}$	$\cdots$
GW190727_060333	178^{+18}_{-16}	345^{+587}_{-267}	201^{+11}_{-21}	$6.1^{+1.1}_{-0.8}$	$21.1^{+25.6}_{-17.9}$	$15.4^{+5.3}_{-6.1}$
GW190828_063405	239^{+10}_{-11}	247^{+350}_{-15}	$\cdots$	$4.8^{+0.6}_{-0.5}$	$17.3^{+25.3}_{-10.4}$	$\cdots$
GW190910_112807	177^{+8}_{-8}	166^{+9}_{-8}	174^{+12}_{-8}	$5.9^{+0.8}_{-0.5}$	$13.2^{+17.1}_{-6.2}$	$9.5^{+3.1}_{-2.7}$
GW190915_235702	232^{+14}_{-18}	534^{+371}_{-493}	$\cdots$	$4.6^{+0.8}_{-0.6}$	$15.0^{+30.1}_{-13.1}$	$\cdots$

distributions. We only include events that have SNR > 8 in both the inspiral and postinspiral regimes, with cutoff frequencies as in Table IV. This is because, in order to make meaningful inferences about $\delta\hat{f}_{220}$ and $\delta\hat{\tau}_{220}$ with PSEOB in the absence of measurable HMs, the signal must contain sufficient information in the inspiral and merger stages to break the degeneracy between the binary total mass and the GR deviations. The fractional deviations obtained this way quantify the agreement between the pre- and postmerger portions of the waveform, and are thus not fully analogous to the PYRING quantities.

From Fig. 14, the frequency and the damping time of the 220 mode are consistent with the GR prediction ($\delta\hat{f}_{220} = \delta\hat{\tau}_{220} = 0$) for GW190519_153544 and GW190521_074359, while for GW190910_112807 it shows excellent agreement with GR for $\delta\hat{f}_{220}$ but the GR prediction has only little support in the marginalized posterior distribution of $\delta\hat{\tau}_{220}$.

In spite of the low number of events, we also apply the hierarchical framework to the marginal distributions in Fig. 14. The population-marginalized constraints are $\delta\hat{f}_{220} = 0.03^{+0.38}_{-0.35}$ and $\delta\hat{\tau}_{220} = 0.16^{+0.98}_{-0.98}$, which are consistent with GR for both parameters. The $\delta\hat{\tau}_{220}$ measurement is uninformative, which is not surprising given the spread of the GW190910_112807 result and the low number of events. The hyperparameters also reflect this, since they are constrained for $\delta\hat{f}_{220}$ ($\mu = 0.03^{+0.17}_{-0.18}$,

$\sigma < 0.37$) but uninformative for $\delta\hat{\tau}_{220}$ ($\mu = 0.16^{+0.47}_{-0.46}$, $\sigma < 0.88$). The bounds for the fractional deviation in frequency for the 220 mode, from the PSEOB analysis, and for the 221 mode, from the PYRING analysis, can be used to cast constraints on specific theories of modified gravity that predict non-zero values of these deviations [236,237], as well as to bound possible deviations in the ringdown spectrum caused by a non-Kerr-BH remnant object (see, e.g., [238]).

B. Echoes

It is hypothesized that there may be compact objects having a light ring and a reflective surface located between the light ring and the would-be event horizon. These compact objects are referred to as exotic compact objects (ECOs), for example gravastars [239] and fuzzballs [240,241]. When an ECO is formed as the remnant of a compact binary coalescence, a train of repeating pulses known as GW echoes are emitted from the ECO in the late postmerger stage in addition to the usual ringdown we expect from BHs. The effective potential barrier and the reflective surface act like a cavity trapping the GWs. Unlike BHs, which have a purely in-going boundary condition at the event horizon, the GWs trapped in the cavity will be reflected back and forth between the potential barrier and the surface, emitting pulses of waves towards infinity when some of the waves are transmitted
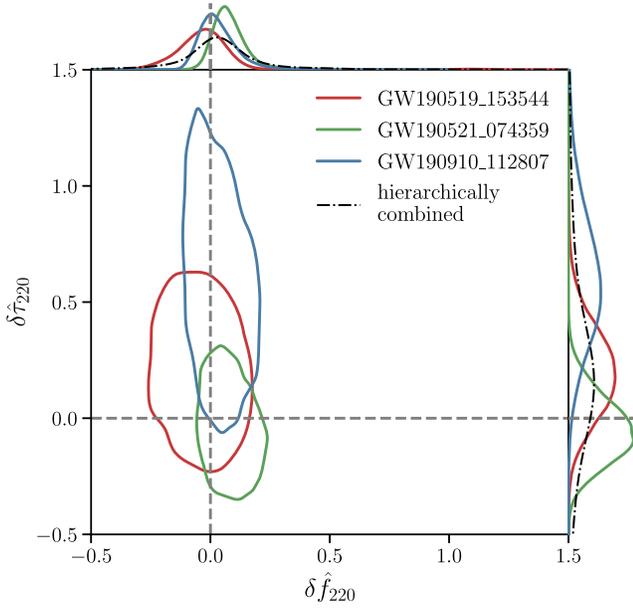
FIG. 14. The 90% credible region of the joint posterior distribution of the fractional deviations of the frequency $\delta\hat{f}_{220}$ and the damping time $\delta\hat{\tau}_{220}$, and their marginalized posterior distributions, for the $\ell = |m| = 2, n = 0$ mode from the PSEOBNRV4HM analysis. We only include events that have SNR > 8 in both the inspiral and postinspiral stage in this plot where we have sufficient information to break the degeneracy between the binary total mass and the fractional deviation parameters in the absence of measurable HMs. The measurements of the fractional deviations for individual events, and as a set of measurements, both show consistency with GR.

through the potential barrier and escape [242–247]. Detecting these GW echoes would be clear evidence of the existence of these proposed ECOs [248–250], though there are still no full and viable models of ECOs that produce echoes [247,251–254].

We employ a template-based approach [255] that uses the model proposed in [256] to search for GW echoes. The waveform model takes the ringdown part of an IMR waveform and repeats the modulated ringdown waveform according to five additional echo parameters which control the relative amplitude of the echoes, the damping factor between each echo, the start time of ringdown, the time of the first echo with respect to the merger, and the time delay between each echo. We adopt a uniform prior for each of the echo parameters. We used IMRPHENOMPV2 as the IMR waveform approximant for all the events we analyzed except for GW190521 where NRSUR7DQ4 was used instead. The pipeline computes the log Bayes factor $\log_{10}\mathcal{B}_{\mathrm{IMR}}^{\mathrm{IMRE}}$ of the data being describable by an inspiral-merger-ringdown-echoes (IMRE) waveform versus an IMR waveform and uses it as the detection statistic to identify the existence of echoes in the data.

We analyze 31 BBH signals from GWTC-2 passing our false-alarm rate threshold (see Sec. II and Table I) and

TABLE X. Results of search for GW echoes. A positive value of the log Bayes factor $\log_{10}\mathcal{B}_{\mathrm{IMR}}^{\mathrm{IMRE}}$ indicates a preference for the IMRE model over the IMR model, while a negative value of the log Bayes factor suggests instead a preference for the IMR model over the IMRE model.

Event	$\log_{10}\mathcal{B}_{\mathrm{IMR}}^{\mathrm{IMRE}}$	Event	$\log_{10}\mathcal{B}_{\mathrm{IMR}}^{\mathrm{IMRE}}$
GW150914	−0.57	GW170809	−0.22
GW151226	−0.08	GW170814	−0.49
GW170104	−0.53	GW170818	−0.62
GW170608	−0.44	GW170823	−0.34
GW190408_181802	−0.93	GW190706_222641	−0.10
GW190412	−1.30	GW190707_093326	0.08
GW190421_213856	−0.11	GW190708_232457	−0.87
GW190503_185404	−0.36	GW190720_000836	−0.45
GW190512_180714	−0.56	GW190727_060333	0.01
GW190513_205428	−0.03	GW190728_064510	0.01
GW190517_055101	0.16	GW190828_063405	0.10
GW190519_153544	−0.10	GW190828_065509	−0.01
GW190521	−1.82	GW190910_112807	−0.22
GW190521_074359	−0.72	GW190915_235702	0.17
GW190602_175927	0.13	GW190924_021846	−0.03
GW190630_185205	0.08		

report the search results of GW echoes in Table X.[11] No statistically significant evidence of echoes was found in the data; it was reported in [255] that for detector noise fluctuations typical for O1, a detection threshold for $\log_{10}\mathcal{B}_{\mathrm{IMR}}^{\mathrm{IMRE}}$ was found to be roughly 2.48 by empirically constructing the background distribution of the Bayes factor if we require the false-alarm probability to be $\lesssim 3 \times 10^{-7}$. The event GW190915_235702 has the highest $\log_{10}\mathcal{B}_{\mathrm{IMR}}^{\mathrm{IMRE}}$ of merely 0.17, which indicates negligible support for the presence of GW echoes in the data. While we did not present the Bayes factor for GW151012 and GW170729 here as their corresponding FARs are above the threshold, the results are consistent with no significant evidence of echoes being found in the data. The null results for O1 and O2 events are consistent with what was reported in [255,257–261]. The posterior distributions of the extra echo parameters mostly recover their corresponding prior distributions, consistent with the fact that we did not detect any echoes in the data.

VIII. POLARIZATIONS

Generic metric theories of gravity may allow up to six GW polarizations [262,263]. These correspond to the two tensor modes (helicity ± 2) allowed in GR, plus two additional vector modes (helicity ± 1), and two scalar modes (helicity 0). The polarization content of a GW is imprinted in the relative amplitudes of the outputs at

---

[11]We do not analyze GW190814 because the long data segment and high sampling rate it requires makes the analysis prohibitively expensive.

different detectors, as determined by the corresponding antenna patterns [1,264–267]. This fact can be used to reconstruct the GW polarization content from the data, although a five-detector network would be needed to do this optimally with transient signals. The existing three-detector network may be used to distinguish between some specific subsets of all the possible polarization combinations.

We previously reported constraints on extreme polarization alternatives (full tensor versus full vector, and full tensor versus full scalar) in [13–15], using a simplified analysis that relied on GR templates [267]. None of the events analyzed (GW170814, GW170817, and GW170818) disfavored the tensorial hypothesis. Because the source sky location was known from electromagnetic observations [268], the results were strongest for GW170817, which we found to be highly inconsistent with the full-vector and full-scalar hypotheses with (base ten) log Bayes factors $\gtrsim 20$ [14]. Although this is strong evidence against vector or scalar being the only possible GW polarization, it does not strictly preclude scenarios in which only some sources produce vector-only or scalar-only GWs.

Here we probe the same extreme polarization hypotheses as in previous studies, but through a different technique that does not rely on specific waveform models. This null-stream based polarization test is a Bayesian implementation of the null stream construct proposed in [269], generalized to vector and scalar antenna patterns [88,264]. A null stream is a linear combination of the data streams from different detectors that is known to be free of true GWs with a given helicity and sky location, irrespective of the GW waveform. Any excess power remaining in the null stream must have been produced by a GW signal whose helicity or sky location is not what was assumed. We quantify such excess power by means of the null energy, as defined in [87]. If the polarization modes and the sky location of the GW signal are correctly specified, this quantity will fluctuate solely due to instrumental noise and will follow a chi-squared distribution [87]. This provides a likelihood function for the hypothesis that the data contain a signal with a given helicity and sky location. By marginalizing over the source location, we may obtain the evidences of different polarization hypotheses and compute Bayes factors comparing them. We take a uniform distribution over the celestial sphere as our sky-location prior and compute evidences through an extended version of the BANTAM pipeline presented in [88].

In Table XI, we present the resulting Bayes factors for full-tensor versus full-vector $\mathcal{B}_V^T$, and full-tensor versus full-scalar $\mathcal{B}_S^T$. None of the signals analyzed favor either of the non-GR hypotheses (full-vector, or full-scalar) to any significant degree. The Bayes factors in Table XI are less informative than those in [13–15] because the present method does not attempt to track the signal phase across time, relying only on signal power added incoherently

TABLE XI. Base-ten logarithms of Bayes factors for different polarization hypotheses: full-tensor versus full-vector ($\log_{10} \mathcal{B}_V^T$), and full-tensor versus full-scalar ($\log_{10} \mathcal{B}_S^T$). These results were obtained with the waveform independent method described in Sec. VIII. They are less informative than those in [13–15] because the present method does not attempt to track the signal phase across time.

Event	$\log_{10} \mathcal{B}_V^T$	$\log_{10} \mathcal{B}_S^T$
GW170809	0.078	0.421
GW170814	−0.032	0.740
GW170818	0.002	0.344
GW190408_181802	0.076	0.480
GW190412	0.079	0.539
GW190503_185404	−0.072	1.245
GW190512_180714	−0.024	0.346
GW190513_205428	0.139	1.380
GW190517_055101	0.008	0.730
GW190519_153544	0.067	0.799
GW190521	0.093	1.156
GW190602_175927	−0.064	0.373
GW190706_222641	0.052	0.771
GW190720_000836	0.034	0.074
GW190727_060333	0.087	1.024
GW190728_064510	−0.024	0.083
GW190828_063405	0.063	0.851
GW190828_065509	−0.034	0.084
GW190915_235702	0.020	1.238
GW190924_021846	−0.051	0.384

across time–frequency pixels of the null stream [87]. The events yielding the lowest Bayes factors are GW190503_185404 and GW190720_000836, with $\log_{10} \mathcal{B}_V^T = -0.072$ and $\log_{10} \mathcal{B}_S^T = -0.074$ respectively; on the other hand, the event yielding the highest Bayes
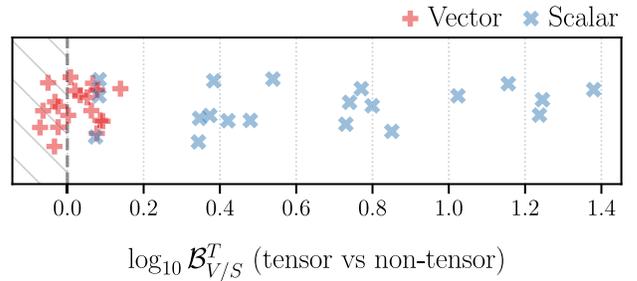

FIG. 15. Distribution of $\log_{10}$ Bayes factors for different polarization hypotheses: full-tensor versus full-vector (red), and full-tensor versus full-scalar (blue). The horizontal axis of this strip plot represents the logarithm of $\mathcal{B}_{V/S}^T$ in Table XI, with each red/blue marker corresponding to a single event; the vertical axis carries no meaning. Values of $\log_{10} \mathcal{B}_{V/S}^T < 0$ indicate a preference for the nontensor hypothesis (hatched region). The different spreads of the sets of markers are as expected for GR signals, and no event reaches large negative values of $\log_{10} \mathcal{B}_{V/S}^T$, meaning all signals are consistent with tensor polarizations.

factors is GW190513_205428 for both vector and scalar, with $\log_{10}\mathcal{B}_V^T = 0.139$ and $\log_{10}\mathcal{B}_S^T = 1.380$ respectively.

The distributions of $\log_{10}\mathcal{B}_V^T$ and $\log_{10}\mathcal{B}_S^T$ are as expected from GR signals with the observed SNRs [270]. As is clear from Fig. 15, the scalar results more decisively favor the tensor hypothesis than the vector ones. The asymmetry between the vector and scalar results is explained by the intrinsic geometries of the LIGO–Virgo antenna patterns, which make scalar waves easier to distinguish [270]. As in previous studies, we conclude there is no evidence for pure vector or pure scalar polarizations.

IX. CONCLUSIONS AND OUTLOOK

GWs give us an opportunity to observationally probe the nature of gravity in its strong-field, dynamical regime, which is difficult to access by other means. With an ever-growing number of detections, we are now able to put GR to the test with increasing precision and in qualitatively new ways. In this paper, we presented eight tests of GR and the nature of BHs using signals from the latest LIGO-Virgo catalog, GWTC-2 [16]. These tests leverage different aspects of GW physics to constrain the null hypothesis that our signals were produced by merging Kerr BHs in agreement with Einstein's theory, and that our GR-based models are sufficient to capture their behavior. We find that all of the LIGO-Virgo detections analyzed are consistent with GR, and do not find any evidence for deviations from theoretical expectations, or unknown systematics.

We began by checking the consistency of the data with the GR prediction in a generic way through the residuals and IMR consistency tests (Sec. IV). We found that, for all events, residual data obtained after subtracting a best-fit GR waveform are consistent with instrumental noise (Sec. IV A) and confirmed that events return compatible parameter estimates when the low- and high-frequency regimes are analyzed separately (Sec. IV B).

Next we focused on controlled deviations away from the GR prediction for the GW waveform (Sec. V A). Allowing for corrections to the GW phasing through inspiral PN parameters, as well as phenomenological merger-ringdown coefficients, we found no evidence for GR deviations, and improved previous constraints in [15] by a factor of ~2. We also targeted specific deviations in the GW phasing due to modifications to the spin-induced quadrupole moment of the binary components, obtaining broad constraints in agreement with the Kerr hypothesis (Sec. V B). Through a generalized dispersion relation, we tested GR's prediction that GWs propagate without dispersion and that the graviton is massless (Sec. VI). We found no evidence for GW dispersion, and tightened previous constraints on Lorentz-violating dispersion parameters by a factor of ~2.6. Notably, we constrained the mass of the graviton to be $m_g \lesssim 1.76 \times 10^{-23}$ eV/c^2 with 90% credibility—an

improvement of a factor of 2.7 over the GWTC-1 measurement [15], and of 1.8 over Solar System bounds [197].

The detection of relatively high-mass events, coupled with the development of novel analysis techniques, allowed us to probe the properties of the merger remnant through targeted studies of the signal after merger. We validated the expectation that the remnants were Kerr BHs, constraining QNM frequencies and damping times (Sec. VII A). The results show agreement with Kerr remnants: the population-marginalized constraint on the fractional deviation away from the Kerr frequency is $\delta\hat{f}_{220} = 0.03^{+0.38}_{-0.35}$ for the 220 mode, and $\delta\hat{f}_{221} = 0.04^{+0.27}_{-0.32}$ for the 221 mode at 90% credibility. In addition, we considered the existence of GW echoes—repetitions of the postmerger signal that could signal the presence of some reflective structure near the presumed event horizon of the remnant object, absent for classical BHs (Sec. VII B). A search for such excess power after the main signal using periodic templates yielded no significant evidence for echoes.

Finally, we studied the polarization content of GWs with a new approach that does not make use of templates to reconstruct the signal power (Sec. VIII). With only three active detectors, we cannot simultaneously constrain all the six possible GW polarizations allowed in generic metric theories of gravity (scalar, vector, and tensor). Instead, as in previous studies, we compared the likelihood of having purely scalar or purely vector polarizations against the pure tensor case, predicted by GR. We found no evidence in favor of nontensor GWs.

Our conclusions come from the analysis of multiple BBH signals, studied individually and collectively. To understand our measurements holistically, we made use of a variety of statistical techniques, including hierarchical Bayesian inference, to evaluate the agreement of our set of measurements with the expectation from GR. As the number of GW detections continues to grow, these strategies will become increasingly indispensable as tools to properly interpret our data and their agreement with theory, as well as to tease out potential disagreements that would be indiscernible from individual signals. With constantly improving detectors and analysis capabilities, we will continue to expand the scope and sensitivity of our tests of GR and our probes of the nature of BHs when analyzing data from O3b and future observing runs.

APPENDIX A: RESIDUALS p-VALUE UNCERTAINTY

The light-blue band in Fig. 2 represents the 90%-credible band on the cumulative distribution of p-values from the residuals analysis (Sec. IV A). This incorporates two types of uncertainty [284]:

(i) uncertainty in the true p-value for any specific event, due to the finite number of noise instantiations used to compute the background SNR_{90};

(ii) uncertainty in the fraction of events yielding a p-value below any given benchmark, due to the finite number of events observed.

These two types of ignorance translate into uncertainty in the abscissa and ordinate values in Fig. 2, respectively. We compute the corresponding credible band as explained below.

The true (unknown) p-value for a given event is estimated by counting the number of noise instances n that yield an SNR_{90} greater than or equal to the on-source threshold SNR_{90}^{thr}, out of a total $N = 193$ trials. We denote the true p-value by $p = P(SNR_{90}^{thr} \leq SNR_{90})$, and the estimate from finite noise instances as $\hat{p} = n/N$. For a given true value of p, the expected likelihood of observed $\hat{p}$ will be given by the binomial distribution,

$$P(n, N|p) = \binom{N}{n} p^n (1 - p)^{N-n}, \qquad (A1)$$

by definition of the p-value. Under the null hypothesis, we expect p to be uniformly distributed, so we may set this as our prior and obtain a posterior distribution on p functionally identical to the likelihood. With p as the variable, this is a beta distribution,

$$p \sim \text{Beta}(n + 1, N - n + 1), \qquad (A2)$$

which has mean $\langle p \rangle = (n + 1)/(N + 2) \approx \hat{p}$. The central blue line in Fig. 2 corresponds to $\hat{p}$, rather than $\langle p \rangle$, but the two are effectively equivalent.

To produce the credible band in Fig. 2, we further need to understand the expected distribution of $\hat{p}$'s for a set of $N_e = 34$ events. To do this, we produce a large number of synthetic p-value sets by drawing each of the N_e elements from Eq. (A2), with n and N corresponding to the measured values for each event. Each individual simulation produces a PP curve akin to the central line in Fig. 2. These curves are contained within the light blue band 90% of the time.

APPENDIX B: INSPIRAL-MERGER-RINGDOWN CONSISTENCY TEST SYSTEMATICS

1. Redshifted total mass

From the study of simulated signals, it is known that the IMR consistency test of Sec. IV B may be strongly biased for heavy BBHs. This is because sources with high redshifted mass lead to short signals in the detectors and do not contain sufficient information about the inspiral regime. For this reason, most of the results discussed in the main text (namely, Figs. 3 and 4) imposed a criterion on the median redshifted total mass so that $(1 + z)M < 100 \, M_\odot$.

Here we discuss the results for the events that did not make that cut.

Excessively high redshifted masses can lead to strong systematic biases in $\Delta M_f / \bar{M}_f$. This is evident in Fig. 16, which is the equivalent of Fig. 3 for the heavy events with median $(1 + z)M > 100 \, M_\odot$ that we excluded in the main text. In spite of this, the joint posterior obtained by multiplying the individual results is hardly affected by the inclusion of the biased events (cf. gray and black distributions in Fig. 16). This is because the joint posterior is driven by the individual events whose distributions have the narrowest support: the deviations towards high $\Delta M_f / \bar{M}_f$ get washed out, and the combined result thus fails to identify that a significant fraction of the signals do not conform to the null hypothesis.

The hierarchical results are, on the other hand, sensitive to this sort of effect. This can be seen most clearly in the posterior for the $\Delta M_f / \bar{M}_f$ hyperdistribution mean μ and standard deviation σ, as defined in Sec. III B. Figure 17 shows the marginal distributions for these parameters as obtained when including (excluding) the events with $(1 + z)M > 100 \, M_\odot$ in red (blue). The subpopulation of biased events manifests itself in anomalous distributions for the hyperparameters that disfavor $\mu = \sigma = 0$. Removing the heavy events, which are known to be biased, restores support for $\mu = \sigma = 0$, and yields the nominal observed distribution shown in Fig. 4.
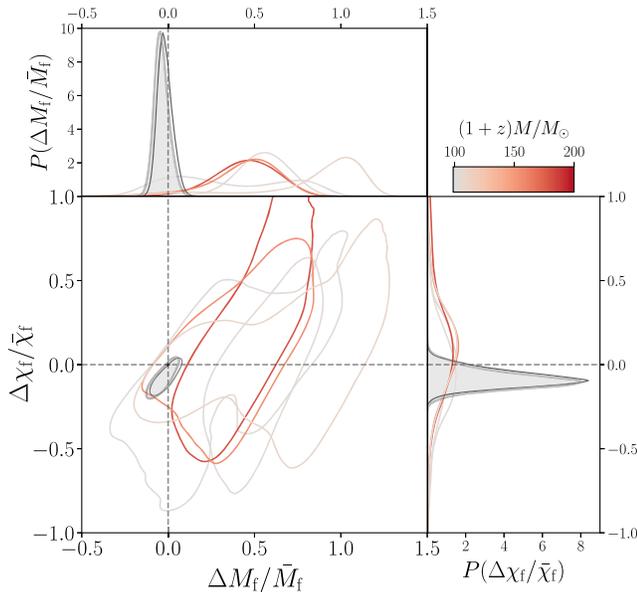

FIG. 17. Marginal posteriors for the hyperdistribution mean μ and standard deviation σ for the $\Delta M_f / \bar{M}_f$ measurements in GWTC-2. If the biased events with median $(1 + z)M > 100 \, M_\odot$ are included (red) the analysis mildly suggests a deviation from the null-hypothesis ($\mu = \sigma = 0$); as expected, this goes away if the heavy events are excluded (blue). The nominal blue posteriors correspond to the population distribution presented in Fig. 4.

2. Waveform modeling

In order to gauge systematic errors arising from imperfect waveform modeling, we perform the IMR consistency test using both IMRPHENOMPV2 and SEOBNRV4_ROM. Although SEOBNRV4_ROM is a nonprecessing waveform approximant, we find that the posteriors are in broad agreement with no qualitative differences between the

FIG. 16. As in Fig. 3 of the main text, but for the events excluded for having median $(1 + z)M > 100 \, M_\odot$ (Table IV). These events present a systematic bias in $\Delta M_f / \bar{M}_f$. The gray distribution corresponds to the same joint posterior as in Fig. 3, while the thin black one is obtained if the heavy events are also included.
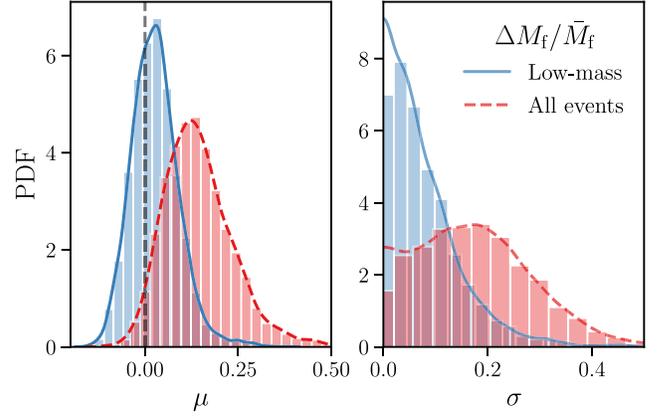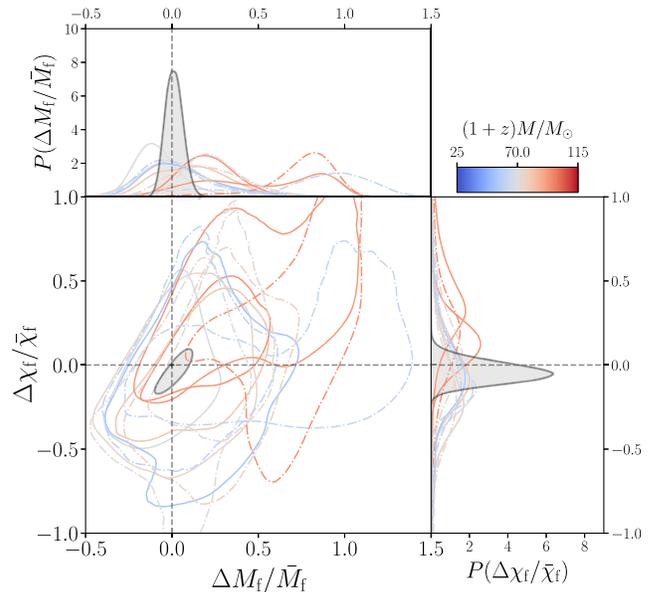

FIG. 18. As per Fig. 3 but using the nonprecessing SEOBNRV4_-ROM waveform model. Posteriors for the heavier events in Fig. 17 are not shown here, but are included in the data release for this paper [53]. Results for GW190412 and GW190814 are not included due to the relative importance of HMs, as discussed in Sec. IV B.

results (Fig. 18). Assuming that the fractional deviations take the same value for all events, at 90% credibility we find $\Delta M_{\rm f}/\bar{M}_{\rm f} = 0.01^{+0.09}_{-0.08}$ and $\Delta\chi_{\rm f}/\bar{\chi}_{\rm f} = -0.05^{+0.11}_{-0.09}$ when using SEOBNRV4_ROM, consistent with the GR values.

The differences in individual posteriors are expected due to differing physics and modeling of the final state between the approximants. For the two events in the IMR test where HMs are important, GW190412 [111] and GW190814 [66], we use IMRPHENOMPV3HM as the preferred waveform approximant. As systematic errors are demonstrably larger when neglecting HMs for these two events, they are excluded when constructing the joint posteriors for the SEOBNRV4_ROM analysis.

APPENDIX C: IMPACT OF HIGHER MOMENTS ON PARAMETRIZED TESTS

For the tests detailed in Sec. VA, the majority of events were analyzed using IMRPHENOMPV2 and SEOBNRV4_ROM, which only model the dominant $\ell = 2$ modes and neglect subdominant spherical harmonic multipoles. However, two of the BBHs considered in our analysis, GW190412 [111] and GW190814 [66], have asymmetric component masses and detailed investigations show strong evidence for the presence of HMs. Using approximants that only capture the dominant $\ell = 2$ multipole moments could therefore lead to systematic errors and biases that present as false deviations of GR. In order to mitigate such systematics, we analyzed both these events using IMRPHENOMPV3HM, a precessing waveform approximant incorporating HMs, and GW190814 with SEOBNRV4HM_ROM, an aligned-spin approximant with HMs, as described in Sec. III.

In Fig. 19 we show the marginalized 1D posteriors for the parametrized violations of GR using IMRPHENOMPV3HM and SEOBNRV4HM_ROM. As this is the first time that constraints are obtained using approximants with HMs, we explicitly show the marginalized 1D posteriors for the deviation coefficients. As mentioned in the main text, it is not necessarily surprising that we find some events for which the GR values fall in the tail of the posterior, as is the case for GW190814. The fact that this takes place for several GW190814 coefficients is also not necessarily abnormal, since these are not statistically independent measurements. In addition, due to the way in which the parametrized tests are implemented, certain regions of the parameter space can lead to unphysical and pathological features in the waveform, potentially leading to multimodal posteriors and poor convergence of the posterior samples. Such features are observed in the $\delta\varphi_6$ and $\delta\varphi_7$ posteriors for the IMRPHENOMPV3HM analysis of GW190814, as in Fig. 19, and pathologies were found to occur when $\delta\varphi_6$ ($\delta\varphi_7$) becomes too negative (positive). We urge caution about the use and interpretation of these two coefficients in further studies, but find that these GW190814 results do not have any notable impact on the combined posteriors and the resulting hierarchical analysis. GW190814 is highly asymmetric and occurs in a region of the parameter space in which parametrized tests have not been systematically studied. For future analyses, detailed studies across the parameter space will be important in characterizing systematic errors, biases, and waveform pathologies as well as their impact on parameter estimation.
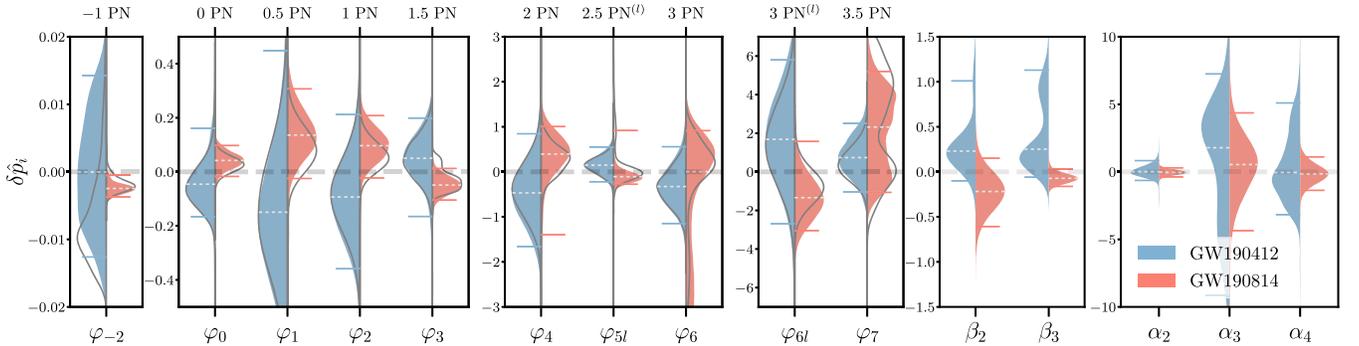

FIG. 19.   Posteriors for parametrized violations of GR inferred using IMRPHENOMPV3HM and SEOBNRV4HM_ROM (black solid lines). The horizontal solid lines indicate the 90% credible intervals and the white dashed line marks the median. The horizontal dashed line at $\delta\hat{p}_i = 0$ denote the GR values. Posteriors for GW190412 are shown in blue and for GW190814 in red.

[1] C. M. Will, Living Rev. Relativity **17,** 4 (2014).
[2] N. Wex, in *Frontiers in Relativistic Celestial Mechanics Volume 2: Applications and Experiments*, edited by S. M. Kopeikin (De Gruyter, Berlin, Boston, 2014), pp. 39–102.
[3] T. Clifton, P. G. Ferreira, A. Padilla, and C. Skordis, Phys. Rep. **513,** 1 (2012).
[4] P. G. Ferreira, Annu. Rev. Astron. Astrophys. **57,** 335 (2019).
[5] B. P. Abbott *et al.* (LIGO Scientific and Virgo Collaborations), Phys. Rev. Lett. **116,** 221101 (2016); **121,** 129902 (E) (2018).
[6] B. P. Abbott *et al.* (LIGO Scientific and Virgo Collaborations), Phys. Rev. X **6,** 041015 (2016); **8,** 039903(E) (2018).
[7] N. Yunes, K. Yagi, and F. Pretorius, Phys. Rev. D **94,** 084002 (2016).
[8] B. P. Abbott *et al.* (LIGO Scientific and Virgo Collaborations), Phys. Rev. Lett. **118,** 221101 (2017); **121,** 129901 (E) (2018).
[9] J. M. Ezquiaga and M. Zumalacárregui, Phys. Rev. Lett. **119,** 251304 (2017).
[10] J. Sakstein and B. Jain, Phys. Rev. Lett. **119,** 251303 (2017).
[11] P. Creminelli and F. Vernizzi, Phys. Rev. Lett. **119,** 251302 (2017).
[12] T. Baker, E. Bellini, P. G. Ferreira, M. Lagos, J. Noller, and I. Sawicki, Phys. Rev. Lett. **119,** 251301 (2017).
[13] B. P. Abbott *et al.* (LIGO Scientific and Virgo Collaborations), Phys. Rev. Lett. **119,** 141101 (2017).
[14] B. P. Abbott *et al.* (LIGO Scientific and Virgo Collaborations), Phys. Rev. Lett. **123,** 011102 (2019).
[15] B. P. Abbott *et al.* (LIGO Scientific and Virgo Collaborations), Phys. Rev. D **100,** 104036 (2019).
[16] R. Abbott *et al.* (LIGO Scientific and Virgo Collaborations), GWTC-2: Compact Binary Coalescences Observed by LIGO and Virgo During the First Half of the Third Observing Run (2020).
[17] B. P. Abbott *et al.* (LIGO Scientific and Virgo Collaborations), Phys. Rev. X **9,** 031040 (2019).
[18] L. Blanchet and B. S. Sathyaprakash, Phys. Rev. Lett. **74,** 1067 (1995).
[19] L. Blanchet and B. S. Sathyaprakash, Classical Quantum Gravity **11,** 2807 (1994).
[20] K. G. Arun, B. R. Iyer, M. S. S. Qusailah, and B. S. Sathyaprakash, Phys. Rev. D **74,** 024006 (2006).
[21] K. G. Arun, B. R. Iyer, M. S. S. Qusailah, and B. S. Sathyaprakash, Classical Quantum Gravity **23,** L37 (2006).
[22] N. Yunes and F. Pretorius, Phys. Rev. D **80,** 122003 (2009).
[23] C. K. Mishra, K. G. Arun, B. R. Iyer, and B. S. Sathyaprakash, Phys. Rev. D **82,** 064010 (2010).
[24] T. G. F. Li, W. Del Pozzo, S. Vitale, C. Van Den Broeck, M. Agathos, J. Veitch, K. Grover, T. Sidery, R. Sturani, and A. Vecchio, Phys. Rev. D **85,** 082003 (2012).
[25] T. G. F. Li, W. Del Pozzo, S. Vitale, C. Van Den Broeck, M. Agathos, J. Veitch, K. Grover, T. Sidery, R. Sturani, and A. Vecchio, J. Phys. Conf. Ser. **363,** 012028 (2012).
[26] M. Agathos, W. Del Pozzo, T. G. F. Li, C. Van Den Broeck, J. Veitch, and S. Vitale, Phys. Rev. D **89,** 082001 (2014).
[27] J. Meidam *et al.*, Phys. Rev. D **97,** 044033 (2018).
[28] T. Islam, A. K. Mehta, A. Ghosh, V. Varma, P. Ajith, and B. S. Sathyaprakash, Phys. Rev. D **101,** 024032 (2020).
[29] C. D. Capano and A. H. Nitz, Phys. Rev. D **102,** 124070 (2020).
[30] M. Okounkova, L. C. Stein, M. A. Scheel, and D. A. Hemberger, Phys. Rev. D **96,** 044020 (2017).
[31] E. W. Hirschmann, L. Lehner, S. L. Liebling, and C. Palenzuela, Phys. Rev. D **97,** 064032 (2018).
[32] H. Witek, L. Gualtieri, P. Pani, and T. P. Sotiriou, Phys. Rev. D **99,** 064035 (2019).
[33] M. Okounkova, L. C. Stein, J. Moxon, M. A. Scheel, and S. A. Teukolsky, Phys. Rev. D **101,** 104016 (2020).
[34] M. Okounkova, Phys. Rev. D **102,** 084046 (2020).
[35] T. P. Sotiriou and E. Barausse, Phys. Rev. D **75,** 084007 (2007).
[36] K. Yagi, L. C. Stein, N. Yunes, and T. Tanaka, Phys. Rev. D **85,** 064022 (2012); **93,** 029902(E) (2016).
[37] S. Mirshekari and C. M. Will, Phys. Rev. D **87,** 084070 (2013).
[38] R. N. Lang, Phys. Rev. D **89,** 084014 (2014).
[39] R. N. Lang, Phys. Rev. D **91,** 084027 (2015).
[40] N. Sennett, S. Marsat, and A. Buonanno, Phys. Rev. D **94,** 084003 (2016).
[41] N. Sennett and A. Buonanno, Phys. Rev. D **93,** 124004 (2016).
[42] F.-L. Julié, J. Cosmol. Astropart. Phys. 01 (2018) 026.
[43] M. Khalil, N. Sennett, J. Steinhoff, J. Vines, and A. Buonanno, Phys. Rev. D **98,** 104010 (2018).
[44] F.-L. Julié, J. Cosmol. Astropart. Phys. 10 (2018) 033.
[45] L. Bernard, Phys. Rev. D **98,** 044004 (2018).
[46] L. Bernard, Phys. Rev. D **99,** 044047 (2019).
[47] F.-L. Julié and E. Berti, Phys. Rev. D **100,** 104061 (2019).
[48] N. Sennett, R. Brito, A. Buonanno, V. Gorbenko, and L. Senatore, Phys. Rev. D **102,** 044056 (2020).
[49] R. Nair, S. Perkins, H. O. Silva, and N. Yunes, Phys. Rev. Lett. **123,** 191101 (2019).
[50] A. Zimmerman, C.-J. Haster, and K. Chatziioannou, Phys. Rev. D **99,** 124044 (2019).
[51] M. Isi, K. Chatziioannou, and W. M. Farr, Phys. Rev. Lett. **123,** 121101 (2019).
[52] B. P. Abbott *et al.* (LIGO Scientific and Virgo Collaborations), Classical Quantum Gravity **34,** 104002 (2017).
[53] LIGO Scientific and Virgo Collaborations, Data release for Tests of General Relativity with GWTC-2, LIGO-P2000438 (2020).
[54] R. Abbott *et al.* (LIGO Scientific and Virgo Collaborations), Open data from the first and second observing runs of Advanced LIGO and Advanced Virgo, arXiv:1912.11716.
[55] LIGO Scientific and Virgo Collaborations, Gravitational Wave Open Science Center, https://www.gw-openscience.org (2018).
[56] J. Aasi *et al.* (LIGO Scientific Collaboration), Classical Quantum Gravity **32,** 115012 (2015).
[57] F. Acernese *et al.* (Virgo Collaboration), Classical Quantum Gravity **32,** 024001 (2015).
[58] S. Karki *et al.*, Rev. Sci. Instrum. **87,** 114503 (2016).
[59] C. Cahillane *et al.*, Phys. Rev. D **96,** 102001 (2017).
[60] A. Viets *et al.*, Classical Quantum Gravity **35,** 095015 (2018).

[61] L. Sun *et al.*, Classical Quantum Gravity **37**, 225008 (2020).

[62] J. C. Driggers *et al.* (LIGO Scientific Collaboration Instrument Science Authors), Phys. Rev. D **99**, 042001 (2019).

[63] D. Davis, T. J. Massinger, A. P. Lundgren, J. C. Driggers, A. L. Urban, and L. K. Nuttall, Classical Quantum Gravity **36**, 055011 (2019).

[64] G. Vajente, Y. Huang, M. Isi, J. C. Driggers, J. S. Kissel, M. J. Szczepanczyk, and S. Vitale, Phys. Rev. D **101**, 042003 (2020).

[65] N. J. Cornish and T. B. Littenberg, Classical Quantum Gravity **32**, 135012 (2015).

[66] R. Abbott *et al.* (LIGO Scientific and Virgo Collaborations), Astrophys. J. Lett. **896**, L44 (2020).

[67] B. P. Abbott *et al.* (LIGO Scientific and Virgo Collaborations), Astrophys. J. Lett. **892**, L3 (2020).

[68] A. H. Nitz *et al.*, PyCBC software, https://github.com/ligo-cbc/pycbc (2018).

[69] T. Dal Canton *et al.*, Phys. Rev. D **90**, 082004 (2014).

[70] S. A. Usman *et al.*, Classical Quantum Gravity **33**, 215004 (2016).

[71] S. Sachdev *et al.*, arXiv:1901.08580.

[72] C. Messick *et al.*, Phys. Rev. D **95**, 042001 (2017).

[73] B. S. Sathyaprakash and S. V. Dhurandhar, Phys. Rev. D **44**, 3819 (1991).

[74] L. Blanchet, T. Damour, B. R. Iyer, C. M. Will, and A. G. Wiseman, Phys. Rev. Lett. **74**, 3515 (1995).

[75] L. Blanchet, T. Damour, G. Esposito-Farèse, and B. R. Iyer, Phys. Rev. D **71**, 124004 (2005).

[76] A. Buonanno, B. R. Iyer, E. Ochsner, Y. Pan, and B. S. Sathyaprakash, Phys. Rev. D **80**, 084043 (2009).

[77] A. Bohé *et al.*, Phys. Rev. D **95**, 044028 (2017).

[78] S. Klimenko, I. Yakushin, A. Mercer, and G. Mitselmakher, Classical Quantum Gravity **25**, 114029 (2008).

[79] S. Klimenko *et al.*, Phys. Rev. D **93**, 042004 (2016).

[80] B. P. Abbott *et al.* (LIGO Scientific and Virgo Collaborations), Phys. Rev. D **93**, 122004 (2016).

[81] H. S. Chia and T. D. P. Edwards, J. Cosmol. Astropart. Phys. 11 (2020) 033.

[82] R. Abbott *et al.* (LIGO Scientific and Virgo Collaborations), Phys. Rev. Lett. **125**, 101102 (2020).

[83] R. Abbott *et al.* (LIGO Scientific and Virgo Collaborations), Astrophys. J. Lett. **900**, L13 (2020).

[84] T. J. Loredo, AIP Conf. Proc. **735**, 195 (2004).

[85] I. Mandel, W. M. Farr, and J. R. Gair, Mon. Not. R. Astron. Soc. **486**, 1086 (2019).

[86] R. Abbott *et al.* (LIGO Scientific and Virgo Collaborations), Population properties of compact objects from the second LIGO–Virgo Gravitational-Wave Transient Catalog (2020).

[87] P. J. Sutton *et al.*, New J. Phys. **12**, 053034 (2010).

[88] P. T. Pang, R. K. Lo, I. C. Wong, T. G. Li, and C. Van Den Broeck, Phys. Rev. D **101**, 104055 (2020).

[89] I. M. Romero-Shaw *et al.*, Mon. Not. R. Astron. Soc. **499**, 3295 (2020).

[90] T. A. Apostolatos, C. Cutler, G. J. Sussman, and K. S. Thorne, Phys. Rev. D **49**, 6274 (1994).

[91] L. E. Kidder, Phys. Rev. D **52**, 821 (1995).

[92] A. Ramos-Buades, S. Husa, G. Pratten, H. Estellés, C. García-Quirós, M. Mateu, M. Colleoni, and R. Jaume, Phys. Rev. D **101**, 083015 (2020).

[93] B. Moore and N. Yunes, Classical Quantum Gravity **37**, 225015 (2020).

[94] I. M. Romero-Shaw, P. D. Lasky, and E. Thrane, Mon. Not. R. Astron. Soc. **490**, 5210 (2019).

[95] Y. Pan, A. Buonanno, A. Taracchini, L. E. Kidder, A. H. Mroué, H. P. Pfeiffer, M. A. Scheel, and B. Szilágyi, Phys. Rev. D **89**, 084006 (2014).

[96] S. Babak, A. Taracchini, and A. Buonanno, Phys. Rev. D **95**, 024010 (2017).

[97] S. Ossokine *et al.*, Phys. Rev. D **102**, 044055 (2020).

[98] S. Husa, S. Khan, M. Hannam, M. Pürrer, F. Ohme, X. J. Forteza, and A. Bohé, Phys. Rev. D **93**, 044006 (2016).

[99] S. Khan, S. Husa, M. Hannam, F. Ohme, M. Pürrer, X. Jiménez Forteza, and A. Bohé, Phys. Rev. D **93**, 044007 (2016).

[100] M. Hannam, P. Schmidt, A. Bohé, L. Haegel, S. Husa, F. Ohme, G. Pratten, and M. Pürrer, Phys. Rev. Lett. **113**, 151101 (2014).

[101] P. Schmidt, M. Hannam, S. Husa, and P. Ajith, Phys. Rev. D **84**, 024046 (2011).

[102] P. Schmidt, M. Hannam, and S. Husa, Phys. Rev. D **86**, 104063 (2012).

[103] P. Schmidt, F. Ohme, and M. Hannam, Phys. Rev. D **91**, 024043 (2015).

[104] A. Taracchini *et al.*, Phys. Rev. D **89**, 061502 (2014).

[105] R. Cotesta, A. Buonanno, A. Bohé, A. Taracchini, I. Hinder, and S. Ossokine, Phys. Rev. D **98**, 084028 (2018).

[106] V. Varma, S. E. Field, M. A. Scheel, J. Blackman, L. E. Kidder, and H. P. Pfeiffer, Phys. Rev. D **99**, 064045 (2019).

[107] R. Cotesta, S. Marsat, and M. Pürrer, Phys. Rev. D **101**, 124040 (2020).

[108] A. Ramos-Buades, P. Schmidt, G. Pratten, and S. Husa, Phys. Rev. D **101**, 103014 (2020).

[109] G. Pratten, S. Husa, C. Garcia-Quiros, M. Colleoni, A. Ramos-Buades, H. Estelles, and R. Jaume, Phys. Rev. D **102**, 064001 (2020).

[110] G. Pratten *et al.*, Phys. Rev. D **103**, 104056 (2021).

[111] R. Abbott *et al.* (LIGO Scientific and Virgo Collaboration), Phys. Rev. D **102**, 043015 (2020).

[112] S. Khan, K. Chatziioannou, M. Hannam, and F. Ohme, Phys. Rev. D **100**, 024059 (2019).

[113] S. Khan, F. Ohme, K. Chatziioannou, and M. Hannam, Phys. Rev. D **101**, 024056 (2020).

[114] V. Varma, S. E. Field, M. A. Scheel, J. Blackman, D. Gerosa, L. C. Stein, L. E. Kidder, and H. P. Pfeiffer, Phys. Rev. Research **1**, 033015 (2019).

[115] K. Chatziioannou, A. Klein, N. Yunes, and N. Cornish, Phys. Rev. D **95**, 104004 (2017).

[116] J. Veitch *et al.*, Phys. Rev. D **91**, 042003 (2015).

[117] LIGO Scientific and Virgo Collaborations, LALSuite Software, 2018.

[118] T. B. Littenberg and N. J. Cornish, Phys. Rev. D **91**, 084034 (2015).

[119] P. Welch, IEEE Trans. Audio Electroacoust. **15**, 70 (1967).

[120] G. Ashton *et al.*, Astrophys. J. Suppl. Ser. **241**, 27 (2019).

[121] R. Smith, G. Ashton, A. Vajpeyi, and C. Talbot, Mon. Not. R. Astron. Soc. **498**, 4492 (2020).

[122] G. Carullo, W. Del Pozzo, and J. Veitch, Phys. Rev. D **99**, 123029 (2019); **100**, 089903(E) (2019).

[123] M. Isi, M. Giesler, W. M. Farr, M. A. Scheel, and S. A. Teukolsky, Phys. Rev. Lett. **123**, 111102 (2019).

[124] P. A. R. Ade *et al.* (Planck Collaboration), Astron. Astrophys. **594**, A13 (2016).

[125] J. Bovy, D. W. Hogg, and S. T. Roweis, Astrophys. J. **700**, 1794 (2009).

[126] B. P. Abbott *et al.* (LIGO Scientific and Virgo Collaboration), Astrophys. J. Lett. **882**, L24 (2019).

[127] C. E. Shannon, Bell Syst. Tech. J. **27**, 379 (1948); **27**, 623 (E) (1948).

[128] B. Carpenter, A. Gelman, M. Hoffman, D. Lee, B. Goodrich, M. Betancourt, M. Brubaker, J. Guo, P. Li, and A. Riddell, J. Stat. Softw. **76**, 1 (2017).

[129] R. A. Fisher, Am. Stat. **2**, 30 (1948).

[130] B. P. Abbott *et al.* (LIGO Scientific and Virgo Collaborations), Classical Quantum Gravity **37**, 055002 (2020).

[131] M. Campanelli, C. O. Lousto, and Y. Zlochower, Phys. Rev. D **79**, 084012 (2009).

[132] R. Owen, Phys. Rev. D **80**, 084012 (2009).

[133] R. Owen, Phys. Rev. D **81**, 124042 (2010).

[134] S. Bhagwat, M. Okounkova, S. W. Ballmer, D. A. Brown, M. Giesler, M. A. Scheel, and S. A. Teukolsky, Phys. Rev. D **97**, 104065 (2018).

[135] S. A. Hughes and K. Menou, Astrophys. J. **623**, 689 (2005).

[136] A. Ghosh, W. Del Pozzo, and P. Ajith, Phys. Rev. D **94**, 104070 (2016).

[137] A. Ghosh, N. K. Johnson-McDaniel, A. Ghosh, C. K. Mishra, P. Ajith, W. Del Pozzo, C. P. L. Berry, A. B. Nielsen, and L. London, Classical Quantum Gravity **35**, 014002 (2018).

[138] J. Healy and C. O. Lousto, Phys. Rev. D **95**, 024037 (2017).

[139] F. Hofmann, E. Barausse, and L. Rezzolla, Astrophys. J. **825**, L19 (2016).

[140] X. Jiménez-Forteza, D. Keitel, S. Husa, M. Hannam, S. Khan, and M. Pürrer, Phys. Rev. D **95**, 064024 (2017).

[141] A. Bohé, M. Hannam, S. Husa, F. Ohme, M. Puerrer, and P. Schmidt, PhenomPv2—Technical Notes for LAL Implementation, Technical Report No. LIGO-T1500602, LIGO Project, 2016.

[142] N. K. Johnson-McDaniel *et al.*, Determining the final spin of a binary black hole system including in-plane spins: Method and checks of accuracy, Tech. Rep. LIGO-T1600168 (LIGO Project, 2016), https://dcc.ligo.org/LIGO-T1600168/public/main.

[143] T. Damour, P. Jaranowski, and G. Schaefer, Phys. Lett. B **513**, 147 (2001).

[144] L. Blanchet, A. Buonanno, and G. Faye, Phys. Rev. D **74**, 104034 (2006).

[145] K. G. Arun, A. Buonanno, G. Faye, and E. Ochsner, Phys. Rev. D **79**, 104023 (2009); **84**, 049901(E) (2011).

[146] A. Bohé, S. Marsat, G. Faye, and L. Blanchet, Classical Quantum Gravity **30**, 075017 (2013).

[147] S. Marsat, A. Bohé, G. Faye, and L. Blanchet, Classical Quantum Gravity **30**, 055007 (2013).

[148] A. Bohé, S. Marsat, and L. Blanchet, Classical Quantum Gravity **30**, 135009 (2013).

[149] L. Blanchet, Living Rev. Relativity **17**, 2 (2014).

[150] T. Damour, P. Jaranowski, and G. Schäfer, Phys. Rev. D **89**, 064058 (2014).

[151] A. Bohé, G. Faye, S. Marsat, and E. K. Porter, Classical Quantum Gravity **32**, 195010 (2015).

[152] M. Pürrer, Phys. Rev. D **93**, 064041 (2016).

[153] L. Sampson, N. Cornish, and N. Yunes, Phys. Rev. D **87**, 102001 (2013).

[154] C.-J. Haster, Pi from the sky—A null test of general relativity from a population of gravitational wave observations, arXiv:2005.05472.

[155] N. Yunes and S. A. Hughes, Phys. Rev. D **82**, 082002 (2010).

[156] A. J. K. Chua and M. Vallisneri, arXiv:2006.08918.

[157] E. Poisson, Phys. Rev. D **57**, 5287 (1998).

[158] W. G. Laarakkers and E. Poisson, Astrophys. J. **512**, 282 (1999).

[159] F. D. Ryan, Phys. Rev. D **52**, 5707 (1995).

[160] N. V. Krishnendu, K. G. Arun, and C. K. Mishra, Phys. Rev. Lett. **119**, 091101 (2017).

[161] R. O. Hansen, J. Math. Phys. (N.Y.) **15**, 46 (1974).

[162] B. Carter, Phys. Rev. Lett. **26**, 331 (1971).

[163] N. Gürlebeck, Phys. Rev. Lett. **114**, 151102 (2015).

[164] N. Uchikata and S. Yoshida, Classical Quantum Gravity **33**, 025005 (2016).

[165] G. Pappas and T. A. Apostolatos, arXiv:1211.6299.

[166] G. Pappas and T. A. Apostolatos, Phys. Rev. Lett. **108**, 231104 (2012).

[167] I. Harry and T. Hinderer, Classical Quantum Gravity **35**, 145010 (2018).

[168] F. D. Ryan, Phys. Rev. D **55**, 6081 (1997).

[169] C. A. R. Herdeiro and E. Radu, Phys. Rev. Lett. **112**, 221101 (2014).

[170] D. Baumann, H. S. Chia, and R. A. Porto, Phys. Rev. D **99**, 044001 (2019).

[171] C. K. Mishra, A. Kela, K. G. Arun, and G. Faye, Phys. Rev. D **93**, 084054 (2016).

[172] N. V. Krishnendu, M. Saleem, A. Samajdar, K. G. Arun, W. Del Pozzo, and C. K. Mishra, Phys. Rev. D **100**, 104019 (2019).

[173] D. A. Brown, H. Fang, J. R. Gair, C. Li, G. Lovelace, I. Mandel, and K. S. Thorne, Phys. Rev. Lett. **99**, 201102 (2007).

[174] C. L. Rodriguez, I. Mandel, and J. R. Gair, Phys. Rev. D **85**, 062002 (2012).

[175] L. Barack and C. Cutler, Phys. Rev. D **75**, 042003 (2007).

[176] S. Babak, J. Gair, A. Sesana, E. Barausse, C. F. Sopuerta, C. P. L. Berry, E. Berti, P. Amaro-Seoane, A. Petiteau, and A. Klein, Phys. Rev. D **95**, 103012 (2017).

[177] S. Laine *et al.*, Astrophys. J. Lett. **894**, L1 (2020).

[178] K. Akiyama *et al.* (Event Horizon Telescope Collaboration), Astrophys. J. Lett. **875**, L1 (2019).

[179] N. V. Krishnendu, C. K. Mishra, and K. G. Arun, Phys. Rev. D **99**, 064008 (2019).

[180] N. Sennett, T. Hinderer, J. Steinhoff, A. Buonanno, and S. Ossokine, Phys. Rev. D **96**, 024002 (2017).

[181] N. K. Johnson-McDaniel, A. Mukherjee, R. Kashyap, P. Ajith, W. Del Pozzo, and S. Vitale, Phys. Rev. D **102**, 123010 (2020).

[182] C. Pacilio, M. Vaglio, A. Maselli, and P. Pani, Phys. Rev. D **102**, 083002 (2020).

[183] V. Cardoso, E. Franzin, A. Maselli, P. Pani, and G. Raposo, Phys. Rev. D **95**, 084014 (2017).

[184] A. Maselli, P. Pani, V. Cardoso, T. Abdelsalhin, L. Gualtieri, and V. Ferrari, Phys. Rev. Lett. **120**, 081101 (2018).

[185] S. Datta, R. Brito, S. Bose, P. Pani, and S. A. Hughes, Phys. Rev. D **101**, 044004 (2020).

[186] S. Datta and S. Bose, Phys. Rev. D **99**, 084001 (2019).

[187] S. Datta, K. S. Phukon, and S. Bose, Recognizing black holes in gravitational-wave observations: Telling apart impostors in mass-gap binaries, arXiv:2004.05974.

[188] S. Datta, Phys. Rev. D **102**, 064040 (2020).

[189] S. Mirshekari, N. Yunes, and C. M. Will, Phys. Rev. D **85**, 024041 (2012).

[190] C. M. Will, Phys. Rev. D **57**, 2061 (1998).

[191] G. Calcagni, Phys. Rev. Lett. **104**, 251301 (2010).

[192] G. Amelino-Camelia, Nature (London) **418**, 34 (2002).

[193] P. Hořava, Phys. Rev. D **79**, 084008 (2009).

[194] A. S. Sefiedgar, K. Nozari, and H. R. Sepangi, Phys. Lett. B **696**, 119 (2011).

[195] V. A. Kostelecký and M. Mewes, Phys. Lett. B **757**, 510 (2016).

[196] D. B. Rubin, Ann. Stat. **9**, 130 (1981).

[197] L. Bernus, O. Minazzoli, A. Fienga, M. Gastineau, J. Laskar, P. Deram, and A. Di Ruscio, Phys. Rev. D **102**, 021501 (2020).

[198] R. Penrose, Riv. Nuovo Cimento **1**, 252 (1969).

[199] R. Penrose, Gen. Relativ. Gravit. **34**, 1141 (2002).

[200] S. Klainerman, in *The Ninth Marcel Grossmann Meeting*, edited by V. G. Gurzadyan, R. T. Jantzen, and R. Ruffini (2002), pp. 28–43.

[201] P. T. Chruściel, J. Lopes Costa, and M. Heusler, Living Rev. Relativity **15**, 7 (2012).

[202] A. G. Doroshkevic, Y. B. Zeldovich, and I. D. Novikov, Sov. Phys. JETP **22**, 122 (1966), http://www.jetp.ac.ru/cgi-bin/e/index/e/22/1/p122?a=list.

[203] W. Israel, Phys. Rev. **164**, 1776 (1967).

[204] S. W. Hawking, Commun. Math. Phys. **25**, 152 (1972).

[205] D. C. Robinson, Phys. Rev. Lett. **34**, 905 (1975).

[206] P. O. Mazur, J. Phys. A **15**, 3173 (1982).

[207] G. Bunting, Ph.D. thesis (to be published) University of New England, Armidale, N. S. W., 1983, https://une-edu-primo.hosted.exlibrisgroup.com/permalink/f/1ibn1hl/61UNE_ALMA2183087660002706.

[208] M. Dafermos and I. Rodnianski, Clay Math. Proc. **17**, 97 (2013), https://inspirehep.net/literature/801418.

[209] G. W. Gibbons, Commun. Math. Phys. **44**, 245 (1975).

[210] R. D. Blandford and R. L. Znajek, Mon. Not. R. Astron. Soc. **179**, 433 (1977).

[211] R. S. Hanni, Phys. Rev. D **25**, 2509 (1982).

[212] S. L. Detweiler, Astrophys. J. **239**, 292 (1980).

[213] O. Dreyer, B. J. Kelly, B. Krishnan, L. S. Finn, D. Garrison, and R. Lopez-Aleman, Classical Quantum Gravity **21**, 787 (2004).

[214] E. Berti, V. Cardoso, and C. M. Will, Phys. Rev. D **73**, 064030 (2006).

[215] S. Gossan, J. Veitch, and B. S. Sathyaprakash, Phys. Rev. D **85**, 124056 (2012).

[216] J. Meidam, M. Agathos, C. Van Den Broeck, J. Veitch, and B. S. Sathyaprakash, Phys. Rev. D **90**, 064009 (2014).

[217] G. Carullo *et al.*, Phys. Rev. D **98**, 104020 (2018).

[218] R. Brito, A. Buonanno, and V. Raymond, Phys. Rev. D **98**, 084038 (2018).

[219] S. Bhagwat, M. Cabero, C. D. Capano, B. Krishnan, and D. A. Brown, Phys. Rev. D **102**, 024023 (2020).

[220] S. Bhagwat, X. J. Forteza, P. Pani, and V. Ferrari, Phys. Rev. D **101**, 044033 (2020).

[221] M. Cabero, J. Westerweck, C. D. Capano, S. Kumar, A. B. Nielsen, and B. Krishnan, Phys. Rev. D **101**, 064044 (2020).

[222] C. V. Vishveshwara, Phys. Rev. D **1**, 2870 (1970).

[223] W. H. Press, Astrophys. J. **170**, L105 (1971).

[224] S. A. Teukolsky, Astrophys. J. **185**, 635 (1973).

[225] S. Chandrasekhar and S. L. Detweiler, Proc. R. Soc. A **344**, 441 (1975).

[226] I. Kamaretsos, M. Hannam, and B. Sathyaprakash, Phys. Rev. Lett. **109**, 141102 (2012).

[227] L. London, D. Shoemaker, and J. Healy, Phys. Rev. D **90**, 124032 (2014); **94**, 069902(E) (2016).

[228] L. T. London, Phys. Rev. D **102**, 084052 (2020).

[229] A. Buonanno, G. B. Cook, and F. Pretorius, Phys. Rev. D **75**, 124018 (2007).

[230] B. J. Kelly and J. G. Baker, Phys. Rev. D **87**, 084004 (2013).

[231] E. Berti and A. Klein, Phys. Rev. D **90**, 064012 (2014).

[232] M. Cabero, C. D. Capano, O. Fischer-Birnholtz, B. Krishnan, A. B. Nielsen, A. H. Nitz, and C. M. Biwer, Phys. Rev. D **97**, 124069 (2018).

[233] M. Giesler, M. Isi, M. A. Scheel, and S. Teukolsky, Phys. Rev. X **9**, 041060 (2019).

[234] I. Ota and C. Chirenti, Phys. Rev. D **101**, 104005 (2020).

[235] X. Jiménez Forteza, S. Bhagwat, P. Pani, and V. Ferrari, Phys. Rev. D **102**, 044053 (2020).

[236] V. Cardoso, M. Kimura, A. Maselli, E. Berti, C. F. B. Macedo, and R. McManus, Phys. Rev. D **99**, 104077 (2019).

[237] R. McManus, E. Berti, C. F. B. Macedo, M. Kimura, A. Maselli, and V. Cardoso, Phys. Rev. D **100**, 044061 (2019).

[238] E. Maggio, L. Buoninfante, A. Mazumdar, and P. Pani, Phys. Rev. D **102**, 064053 (2020).

[239] P. O. Mazur and E. Mottola, arXiv:gr-qc/0109035.

[240] O. Lunin and S. D. Mathur, Nucl. Phys. **B623**, 342 (2002).

[241] O. Lunin and S. D. Mathur, Phys. Rev. Lett. **88**, 211303 (2002), arXiv:hep-th/0202072.

[242] K. Kokkotas, in *Les Houches School of Physics: Astrophysical Sources of Gravitational Radiation* (1995), pp. 89–102.

[243] K. Tominaga, M. Saijo, and K.-i. Maeda, Phys. Rev. D **60**, 024004 (1999).

[244] V. Ferrari and K. Kokkotas, Phys. Rev. D **62**, 107504 (2000).

[245] S. H. Völkel and K. D. Kokkotas, Classical Quantum Gravity **34**, 175015 (2017).

[246] S. H. Völkel and K. D. Kokkotas, Classical Quantum Gravity **35**, 105018 (2018).

[247] V. Cardoso and P. Pani, Living Rev. Relativity **22**, 4 (2019).

[248] V. Cardoso, E. Franzin, and P. Pani, Phys. Rev. Lett. **116,** 171101 (2016).

[249] V. Cardoso, S. Hopper, C. F. B. Macedo, C. Palenzuela, and P. Pani, Phys. Rev. D **94,** 084031 (2016).

[250] A. Maselli, S. H. Völkel, and K. D. Kokkotas, Phys. Rev. D **96,** 064045 (2017).

[251] E. Maggio, V. Cardoso, S. R. Dolan, and P. Pani, Phys. Rev. D **99,** 064007 (2019).

[252] P. Pani and V. Ferrari, Classical Quantum Gravity **35,** 15LT01 (2018).

[253] B. Chen, Y. Chen, Y. Ma, K.-L. R. Lo, and L. Sun, arXiv:1902.08180.

[254] A. Coates, S. H. Völkel, and K. D. Kokkotas, Phys. Rev. Lett. **123,** 171104 (2019).

[255] R. K. L. Lo, T. G. F. Li, and A. J. Weinstein, Phys. Rev. D **99,** 084052 (2019).

[256] J. Abedi, H. Dykaar, and N. Afshordi, Phys. Rev. D **96,** 082004 (2017).

[257] G. Ashton, O. Birnholtz, M. Cabero, C. Capano, T. Dent, B. Krishnan, G. D. Meadors, A. B. Nielsen, A. Nitz, and J. Westerweck, arXiv:1612.05625.

[258] J. Westerweck, A. Nielsen, O. Fischer-Birnholtz, M. Cabero, C. Capano, T. Dent, B. Krishnan, G. Meadors, and A. H. Nitz, Phys. Rev. D **97,** 124037 (2018).

[259] A. B. Nielsen, C. D. Capano, O. Birnholtz, and J. Westerweck, Phys. Rev. D **99,** 104012 (2019).

[260] N. Uchikata, H. Nakano, T. Narikawa, N. Sago, H. Tagoshi, and T. Tanaka, Phys. Rev. D **100,** 062006 (2019).

[261] Y.-T. Wang and Y.-S. Piao, arXiv:2010.07663.

[262] D. M. Eardley, D. L. Lee, A. P. Lightman, R. V. Wagoner, and C. M. Will, Phys. Rev. Lett. **30,** 884 (1973).

[263] D. M. Eardley, D. L. Lee, and A. P. Lightman, Phys. Rev. D **8,** 3308 (1973).

[264] K. Chatziioannou, N. Yunes, and N. Cornish, Phys. Rev. D **86,** 022004 (2012); **95,** 129901(E) (2017).

[265] M. Isi, M. Pitkin, and A. J. Weinstein, Phys. Rev. D **96,** 042001 (2017).

[266] T. Callister, A. S. Biscoveanu, N. Christensen, M. Isi, A. Matas, O. Minazzoli, T. Regimbau, M. Sakellariadou, J. Tasson, and E. Thrane, Phys. Rev. X **7,** 041058 (2017).

[267] M. Isi and A. J. Weinstein, Technical Note, LIGO-P1700276 (2017), arXiv:1710.03794.

[268] B. P. Abbott et al. (LIGO Scientific, Virgo, Fermi-GBM, and INTEGRAL Collaborations), Astrophys. J. Lett. **848,** L13 (2017).

[269] Y. Guersel and M. Tinto, Phys. Rev. D **40,** 3884 (1989).

[270] I. C. F. Wong, P. T. H. Pang, and R. K. L. Lo, Technical notes on null stream polarization test, Technical Report No. LIGO-T2000405, LIGO Scientific Collaboration, 2020, https://dcc.ligo.org/LIGO-T2000405/public.

[271] C. R. Harris et al., Nature (London) **585,** 357 (2020).

[272] P. Virtanen et al., Nat. Methods **17,** 261 (2020).

[273] T. P. Robitaille et al. (Astropy Collaboration), Astron. Astrophys. **558,** A33 (2013).

[274] A. Price-Whelan et al., arXiv:1801.02634.

[275] F. Perez and B. E. Granger, Comput. Sci. Eng. **9,** 21 (2007).

[276] L. C. Stein, J. Open Source Softw. **4,** 1683 (2019).

[277] C. Hoy and V. Raymond, arXiv:2006.06639.

[278] D. Macleod et al., gwpy/gwpy: 2.0.1 (2020).

[279] J. D. Hunter, Comput. Sci. Eng. **9,** 90 (2007).

[280] M. Waskom et al., mwaskom/seaborn: v0.10.1 (2020).

[281] W. Del Pozzo and J. Veitch, CPNest: an efficient python parallelizable nested sampling algorithm, https://github.com/johnveitch/cpnest.

[282] F. Feroz, M. Hobson, and M. Bridges, Mon. Not. R. Astron. Soc. **398,** 1601 (2009).

[283] F. Feroz, M. Hobson, E. Cameron, and A. Pettitt, Open J. Astrophys. **2,** 10 (2019).

[284] S. Talts, M. Betancourt, D. Simpson, A. Vehtari, and A. Gelman, arXiv:1804.06788.

R. Abbott,[1] T. D. Abbott,[2] S. Abraham,[3] F. Acernese,[4,5] K. Ackley,[6] A. Adams,[7] C. Adams,[8] R. X. Adhikari,[1] V. B. Adya,[9] C. Affeldt,[10,11] M. Agathos,[12,13] K. Agatsuma,[14] N. Aggarwal,[15] O. D. Aguiar,[16] L. Aiello,[17,18] A. Ain,[19,20] P. Ajith,[21] S. Akcay,[13] G. Allen,[22] A. Allocca,[19] P. A. Altin,[9] A. Amato,[23] S. Anand,[1] A. Ananyeva,[1] S. B. Anderson,[1] W. G. Anderson,[24] S. V. Angelova,[25] S. Ansoldi,[26,27] J. M. Antelis,[28] S. Antier,[29] S. Appert,[1] K. Arai,[1] M. C. Araya,[1] J. S. Areeda,[30] M. Arène,[29] N. Arnaud,[31,32] S. M. Aronson,[33] K. G. Arun,[34] Y. Asali,[35] S. Ascenzi,[17,36] G. Ashton,[6] S. M. Aston,[8] P. Astone,[37] F. Aubin,[38] P. Aufmuth,[10,11] K. AultONeal,[28] C. Austin,[2] V. Avendano,[39] S. Babak,[29] F. Badaracco,[17,18] M. K. M. Bader,[40] S. Bae,[41] A. M. Baer,[7] S. Bagnasco,[42] J. Baird,[29] M. Ball,[43] G. Ballardin,[32] S. W. Ballmer,[44] A. Bals,[28] A. Balsamo,[7] G. Baltus,[45] S. Banagiri,[46] D. Bankar,[3] R. S. Bankar,[3] J. C. Barayoga,[1] C. Barbieri,[47,48,49] B. C. Barish,[1] D. Barker,[50] P. Barneo,[51] S. Barnum,[52] F. Barone,[53,5] B. Barr,[54] L. Barsotti,[52] M. Barsuglia,[29] D. Barta,[55] J. Bartlett,[50] I. Bartos,[33] R. Bassiri,[56] A. Basti,[20,19] M. Bawaj,[57,58] J. C. Bayley,[54] M. Bazzan,[59,60] B. R. Becher,[61] B. Bécsy,[62] V. M. Bedakihale,[63] M. Bejger,[64] I. Belahcene,[31] D. Beniwal,[65] M. G. Benjamin,[28] R. Benkel,[66] T. F. Bennett,[67] J. D. Bentley,[14] F. Bergamin,[10,11] B. K. Berger,[56] G. Bergmann,[10,11] S. Bernuzzi,[13] C. P. L. Berry,[15] D. Bersanetti,[68] A. Bertolini,[40] J. Betzwieser,[8] R. Bhandare,[69] A. V. Bhandari,[3] D. Bhattacharjee,[70] J. Bidler,[30] I. A. Bilenko,[71] G. Billingsley,[1] R. Birney,[72] O. Birnholtz,[73] S. Biscans,[1,52] M. Bischi,[74,75] S. Biscoveanu,[52] A. Bisht,[10,11] M. Bitossi,[32,19] M.-A. Bizouard,[76] J. K. Blackburn,[1] J. Blackman,[77] C. D. Blair,[78] D. G. Blair,[78] R. M. Blair,[50] O. Blanch,[79] F. Bobba,[80,81] N. Bode,[10,11] M. Boer,[76] Y. Boetzel,[82] G. Bogaert,[76] M. Boldrini,[83,37] F. Bondu,[84] E. Bonilla,[56] R. Bonnand,[38]

P. Booker,[10,11] B. A. Boom,[40] S. Borhanian,[85] R. Bork,[1] V. Boschi,[19] N. Bose,[86] S. Bose,[3] V. Bossilkov,[78] V. Boudart,[45] Y. Bouffanais,[59,60] A. Bozzi,[32] C. Bradaschia,[19] P. R. Brady,[24] A. Bramley,[8] M. Branchesi,[17,18] J. E. Brau,[43] M. Breschi,[13] T. Briant,[87] J. H. Briggs,[54] F. Brighenti,[74,75] A. Brillet,[76] M. Brinkmann,[10,11] R. Brito,[83,37,66] P. Brockill,[24] A. F. Brooks,[1] J. Brooks,[32] D. D. Brown,[65] S. Brunett,[1] G. Bruno,[88] R. Bruntz,[7] A. Buikema,[52] T. Bulik,[89] H. J. Bulten,[40,90] A. Buonanno,[66,91] D. Buskulic,[38] R. L. Byer,[56] M. Cabero,[10,11] L. Cadonati,[92] M. Caesar,[93] G. Cagnoli,[23] C. Cahillane,[1] J. Calderón Bustillo,[6] J. D. Callaghan,[54] T. A. Callister,[94] E. Calloni,[95,5] J. B. Camp,[96] M. Canepa,[97,68] K. C. Cannon,[98] H. Cao,[65] J. Cao,[99] G. Carapella,[80,81] F. Carbognani,[32] M. F. Carney,[15] M. Carpinelli,[100,101] G. Carullo,[20,19] T. L. Carver,[102] J. Casanueva Diaz,[32] C. Casentini,[103,36] S. Caudill,[40] M. Cavaglià,[70] F. Cavalier,[31] R. Cavalieri,[32] G. Cella,[19] P. Cerdá-Durán,[104] E. Cesarini,[36] W. Chaibi,[76] K. Chakravarti,[3] C.-L. Chan,[105] C. Chan,[98] K. Chandra,[106] P. Chanial,[32] S. Chao,[107] P. Charlton,[108] E. A. Chase,[15] E. Chassande-Mottin,[29] D. Chatterjee,[24] M. Chaturvedi,[69] K. Chatziioannou,[94] A. Chen,[105] H. Y. Chen,[109] X. Chen,[78] Y. Chen,[77] H.-P. Cheng,[33] C. K. Cheong,[105] H. Y. Chia,[33] F. Chiadini,[110,81] R. Chierici,[111] A. Chincarini,[68] A. Chiummo,[32] G. Cho,[112] H. S. Cho,[113] M. Cho,[91] S. Choate,[93] N. Christensen,[76] Q. Chu,[78] S. Chua,[87] K. W. Chung,[114] S. Chung,[78] G. Ciani,[59,60] P. Ciecielag,[64] M. Cieślar,[64] M. Cifaldi,[103,36] A. A. Ciobanu,[65] R. Ciolfi,[115,60] F. Cipriano,[76] A. Cirone,[97,68] F. Clara,[50] E. N. Clark,[116] J. A. Clark,[92] L. Clarke,[117] P. Clearwater,[118] S. Clesse,[88] F. Cleva,[76] E. Coccia,[17,18] P.-F. Cohadon,[87] D. E. Cohen,[31] M. Colleoni,[119] C. G. Collette,[120] C. Collins,[14] M. Colpi,[47,48] M. Constancio Jr.,[16] L. Conti,[60] S. J. Cooper,[14] P. Corban,[8] T. R. Corbitt,[2] I. Cordero-Carrión,[121] S. Corezzi,[58,57] K. R. Corley,[35] N. Cornish,[62] D. Corre,[31] A. Corsi,[122] S. Cortese,[32] C. A. Costa,[16] R. Cotesta,[66] M. W. Coughlin,[46,1] S. B. Coughlin,[15,102] J.-P. Coulon,[76] S. T. Countryman,[35] P. Couvares,[1] P. B. Covas,[119] D. M. Coward,[78] M. J. Cowart,[8] D. C. Coyne,[1] R. Coyne,[123] J. D. E. Creighton,[24] T. D. Creighton,[124] M. Croquette,[87] S. G. Crowder,[125] J. R. Cudell,[45] T. J. Cullen,[2] A. Cumming,[54] R. Cummings,[54] L. Cunningham,[54] E. Cuoco,[32,126] M. Curylo,[89] T. Dal Canton,[31,66] G. Dálya,[127] A. Dana,[56] L. M. DaneshgaranBajastani,[67] B. D'Angelo,[97,68] S. L. Danilishin,[128] S. D'Antonio,[36] K. Danzmann,[10,11] C. Darsow-Fromm,[129] A. Dasgupta,[63] L. E. H. Datrier,[54] V. Dattilo,[32] I. Dave,[69] M. Davier,[31] G. S. Davies,[130] D. Davis,[1] E. J. Daw,[131] R. Dean,[93] D. DeBra,[56] M. Deenadayalan,[3] J. Degallaix,[132] M. De Laurentis,[95,5] S. Deléglise,[87] V. Del Favero,[133] F. De Lillo,[88] N. De Lillo,[54] W. Del Pozzo,[20,19] L. M. DeMarchi,[15] F. De Matteis,[103,36] V. D'Emilio,[102] N. Demos,[52] T. Denker,[10,11] T. Dent,[130] A. Depasse,[88] R. De Pietri,[134,135] R. De Rosa,[95,5] C. De Rossi,[32] R. DeSalvo,[136,81] O. de Varona,[10,11] A. Dhani,[85] S. Dhurandhar,[3] M. C. Díaz,[124] M. Diaz-Ortiz Jr.,[33] N. A. Didio,[44] T. Dietrich,[40] L. Di Fiore,[5] C. DiFronzo,[14] C. Di Giorgio,[80,81] F. Di Giovanni,[104] M. Di Giovanni,[137,138] T. Di Girolamo,[95,5] A. Di Lieto,[20,19] B. Ding,[120] S. Di Pace,[83,37] I. Di Palma,[83,37] F. Di Renzo,[20,19] A. K. Divakarla,[33] A. Dmitriev,[14] Z. Doctor,[43] L. D'Onofrio,[95,5] F. Donovan,[52] K. L. Dooley,[102] S. Doravari,[3] I. Dorrington,[102] T. P. Downes,[24] M. Drago,[17,18] J. C. Driggers,[50] Z. Du,[99] J.-G. Ducoin,[31] R. Dudi,[66] P. Dupej,[54] O. Durante,[80,81] D. D'Urso,[100,101] P.-A. Duverne,[31] S. E. Dwyer,[50] P. J. Easter,[6] G. Eddolls,[54] B. Edelman,[43] T. B. Edo,[131] O. Edy,[139] A. Effler,[8] J. Eichholz,[9] S. S. Eikenberry,[33] M. Eisenmann,[38] R. A. Eisenstein,[52] A. Ejlli,[102] L. Errico,[95,5] R. C. Essick,[109] H. Estellés,[119] D. Estevez,[38] Z. B. Etienne,[140] T. Etzel,[1] M. Evans,[52] T. M. Evans,[8] B. E. Ewing,[85] V. Fafone,[103,36,17] H. Fair,[44] S. Fairhurst,[102] X. Fan,[99] A. M. Farah,[109] S. Farinon,[68] B. Farr,[43] W. M. Farr,[141,94] E. J. Fauchon-Jones,[102] M. Favata,[39] M. Fays,[45,131] M. Fazio,[142] J. Feicht,[1] M. M. Fejer,[56] F. Feng,[29] E. Fenyvesi,[55,143] D. L. Ferguson,[92] A. Fernandez-Galiana,[52] I. Ferrante,[20,19] T. A. Ferreira,[16] F. Fidecaro,[20,19] P. Figura,[89] I. Fiori,[32] D. Fiorucci,[17,18] M. Fishbach,[109] R. P. Fisher,[7] J. M. Fishner,[52] R. Fittipaldi,[144,81] M. Fitz-Axen,[46] V. Fiumara,[145,81] R. Flaminio,[38,146] E. Floden,[46] E. Flynn,[30] H. Fong,[98] J. A. Font,[104,147] P. W. F. Forsyth,[9] J.-D. Fournier,[76] S. Frasca,[83,37] F. Frasconi,[19] Z. Frei,[127] A. Freise,[14] R. Frey,[43] V. Frey,[31] P. Fritschel,[52] V. V. Frolov,[8] G. G. Fronzé,[42] P. Fulda,[33] M. Fyffe,[8] H. A. Gabbard,[54] B. U. Gadre,[66] S. M. Gaebel,[14] J. R. Gair,[66] J. Gais,[105] S. Galaudage,[6] R. Gamba,[13] D. Ganapathy,[52] A. Ganguly,[21] S. G. Gaonkar,[3] B. Garaventa,[68,97] C. García-Quirós,[119] F. Garufi,[95,5] B. Gateley,[50] S. Gaudio,[28] V. Gayathri,[33] G. Gemme,[68] A. Gennai,[19] D. George,[22] J. George,[69] R. N. George,[148] L. Gergely,[149] S. Ghonge,[92] Abhirup Ghosh,[66] Archisman Ghosh,[40,150–152] S. Ghosh,[24,39] B. Giacomazzo,[47,48,49] L. Giacoppo,[83,37] J. A. Giaime,[2,8] K. D. Giardina,[8] D. R. Gibson,[72] C. Gier,[25] K. Gill,[35] P. Giri,[19,20] J. Glanzer,[2] A. E. Gleckl,[30] P. Godwin,[85] E. Goetz,[153] R. Goetz,[33] N. Gohlke,[10,11] B. Goncharov,[6] G. González,[2] A. Gopakumar,[154] S. E. Gossan,[1] M. Gosselin,[20,19] R. Gouaty,[38] B. Grace,[9] A. Grado,[155,5] M. Granata,[132] V. Granata,[80] A. Grant,[54] S. Gras,[52] P. Grassia,[1] C. Gray,[50] R. Gray,[54] G. Greco,[74,75] A. C. Green,[33] R. Green,[102] E. M. Gretarsson,[28] H. L. Griggs,[92] G. Grignani,[58,57] A. Grimaldi,[137,138] E. Grimes,[28] S. J. Grimm,[17,18] H. Grote,[102] S. Grunewald,[66] P. Gruning,[31] J. G. Guerrero,[30] G. M. Guidi,[74,75] A. R. Guimaraes,[2] G. Guixé,[51] H. K. Gulati,[63] Y. Guo,[40] Anchal Gupta,[1] Anuradha Gupta,[85] P. Gupta,[40,156] E. K. Gustafson,[1] R. Gustafson,[157] F. Guzman,[116] L. Haegel,[29] O. Halim,[18,17] E. D. Hall,[52]

E. Z. Hamilton,[102] G. Hammond,[54] M. Haney,[82] M. M. Hanke,[10,11] J. Hanks,[50] C. Hanna,[85] M. D. Hannam,[102]
O. A. Hannuksela,[105] O. Hannuksela,[156,40] H. Hansen,[50] T. J. Hansen,[28] J. Hanson,[8] T. Harder,[76] T. Hardwick,[2]
K. Haris,[40,156,21] J. Harms,[17,18] G. M. Harry,[158] I. W. Harry,[139] D. Hartwig,[129] R. K. Hasskew,[8] C.-J. Haster,[52] K. Haughian,[54]
F. J. Hayes,[54] J. Healy,[133] A. Heidmann,[87] M. C. Heintze,[8] J. Heinze,[10,11] J. Heinzel,[159] H. Heitmann,[76] F. Hellman,[160]
P. Hello,[31] A. F. Helmling-Cornell,[43] G. Hemming,[32] M. Hendry,[54] I. S. Heng,[54] E. Hennes,[40] J. Hennig,[10,11]
M. H. Hennig,[10,11] F. Hernandez Vivanco,[6] M. Heurs,[10,11] S. Hild,[128] P. Hill,[25] A. S. Hines,[116] S. Hochheim,[10,11]
E. Hofgard,[56] D. Hofman,[132] J. N. Hohmann,[129] A. M. Holgado,[22] N. A. Holland,[9] I. J. Hollows,[131] Z. J. Holmes,[65] K. Holt,[8]
D. E. Holz,[109] P. Hopkins,[102] C. Horst,[24] J. Hough,[54] E. J. Howell,[78] C. G. Hoy,[102] D. Hoyland,[14] Y. Huang,[52] M. T. Hübner,[6]
A. D. Huddart,[117] E. A. Huerta,[22] B. Hughey,[28] V. Hui,[38] S. Husa,[119] S. H. Huttner,[54] B. M. Hutzler,[2] R. Huxford,[85]
T. Huynh-Dinh,[8] B. Idzkowski,[89] A. Iess,[103,36] S. Imperato,[15] H. Inchauspe,[33] C. Ingram,[65] G. Intini,[83,37] M. Isi,[52]
B. R. Iyer,[21] V. JaberianHamedan,[78] T. Jacqmin,[87] S. J. Jadhav,[161] S. P. Jadhav,[3] A. L. James,[102] K. Jani,[92] K. Janssens,[162]
N. N. Janthalur,[161] P. Jaranowski,[163] D. Jariwala,[33] R. Jaume,[119] A. C. Jenkins,[114] M. Jeunon,[46] J. Jiang,[33] G. R. Johns,[7]
N. K. Johnson-McDaniel,[12] A. W. Jones,[14] D. I. Jones,[164] J. D. Jones,[50] P. Jones,[14] R. Jones,[54] R. J. G. Jonker,[40] L. Ju,[78]
J. Junker,[10,11] C. V. Kalaghatgi,[102] V. Kalogera,[15] B. Kamai,[1] S. Kandhasamy,[3] G. Kang,[41] J. B. Kanner,[1] S. J. Kapadia,[21]
D. P. Kapasi,[9] C. Karathanasis,[79] S. Karki,[70] R. Kashyap,[85] M. Kasprzack,[1] W. Kastaun,[10,11] S. Katsanevas,[32]
E. Katsavounidis,[52] W. Katzman,[8] K. Kawabe,[50] F. Kéfélian,[76] D. Keitel,[119] J. S. Key,[165] S. Khadka,[56] F. Y. Khalili,[71]
I. Khan,[17,36] S. Khan,[102] E. A. Khazanov,[166] N. Khetan,[17,18] M. Khursheed,[69] N. Kijbunchoo,[9] C. Kim,[167] G. J. Kim,[92]
J. C. Kim,[168] K. Kim,[169] W. S. Kim,[170] Y.-M. Kim,[171] C. Kimball,[15] P. J. King,[50] M. Kinley-Hanlon,[54] R. Kirchhoff,[10,11]
J. S. Kissel,[50] L. Kleybolte,[129] S. Klimenko,[33] T. D. Knowles,[140] E. Knyazev,[52] P. Koch,[10,11] S. M. Koehlenbeck,[10,11]
G. Koekoek,[40,172] S. Koley,[40] M. Kolstein,[79] K. Komori,[52] V. Kondrashov,[1] A. Kontos,[61] N. Koper,[10,11] M. Korobko,[129]
W. Z. Korth,[1] M. Kovalam,[78] D. B. Kozak,[1] C. Krämer,[10,11] V. Kringel,[10,11] N. V. Krishnendu,[10,11] A. Królak,[173,174]
G. Kuehn,[10,11] A. Kumar,[161] P. Kumar,[175] Rahul Kumar,[50] Rakesh Kumar,[63] K. Kuns,[52] S. Kwang,[24] B. D. Lackey,[66]
D. Laghi,[20,19] E. Lalande,[176] T. L. Lam,[105] A. Lamberts,[76,177] M. Landry,[50] B. B. Lane,[52] R. N. Lang,[52] J. Lange,[133]
B. Lantz,[56] R. K. Lanza,[52] I. La Rosa,[38] A. Lartaux-Vollard,[31] P. D. Lasky,[6] M. Laxen,[8] A. Lazzarini,[1] C. Lazzaro,[60,59]
P. Leaci,[83,37] S. Leavey,[10,11] Y. K. Lecoeuche,[50] H. M. Lee,[169] H. W. Lee,[168] J. Lee,[112] K. Lee,[56] J. Lehmann,[10,11] E. Leon,[30]
N. Leroy,[31] N. Letendre,[38] Y. Levin,[6] A. Li,[1] J. Li,[99] K. J. L. Li,[105] T. G. F. Li,[105] X. Li,[77] F. Linde,[178,40] S. D. Linker,[67]
J. N. Linley,[54] T. B. Littenberg,[179] J. Liu,[10,11] X. Liu,[24] M. Llorens-Monteagudo,[104] R. K. L. Lo,[1] A. Lockwood,[180]
L. T. London,[52] A. Longo,[181,182] M. Lorenzini,[103,36] V. Loriette,[183] M. Lormand,[8] G. Losurdo,[19] J. D. Lough,[10,11]
C. O. Lousto,[133] G. Lovelace,[30] H. Lück,[10,11] D. Lumaca,[103,36] A. P. Lundgren,[139] Y. Ma,[77] R. Macas,[102] M. MacInnis,[52]
D. M. Macleod,[102] I. A. O. MacMillan,[1] A. Macquet,[76] I. Magaña Hernandez,[24] F. Magaña-Sandoval,[33] C. Magazzù,[19]
R. M. Magee,[85] E. Majorana,[37] I. Maksimovic,[183] S. Maliakal,[1] A. Malik,[69] N. Man,[76] V. Mandic,[46] V. Mangano,[83,37]
G. L. Mansell,[50,52] M. Manske,[24] M. Mantovani,[32] M. Mapelli,[59,60] F. Marchesoni,[184,57] F. Marion,[38] S. Márka,[35] Z. Márka,[35]
C. Markakis,[12] A. S. Markosyan,[56] A. Markowitz,[1] E. Maros,[1] A. Marquina,[121] S. Marsat,[29] F. Martelli,[74,75] I. W. Martin,[54]
R. M. Martin,[39] M. Martinez,[79] V. Martinez,[23] D. V. Martynov,[14] H. Masalehdan,[129] K. Mason,[52] E. Massera,[131]
A. Masserot,[38] T. J. Massinger,[52] M. Masso-Reid,[54] S. Mastrogiovanni,[29] A. Matas,[66] M. Mateu-Lucena,[119] F. Matichard,[1,52]
M. Matiushechkina,[10,11] N. Mavalvala,[52] E. Maynard,[2] J. J. McCann,[78] R. McCarthy,[50] D. E. McClelland,[9] S. McCormick,[8]
L. McCuller,[52] S. C. McGuire,[185] C. McIsaac,[139] J. McIver,[153] D. J. McManus,[9] T. McRae,[9] S. T. McWilliams,[140]
D. Meacher,[24] G. D. Meadors,[6] M. Mehmet,[10,11] A. K. Mehta,[66] A. Melatos,[118] D. A. Melchor,[30] G. Mendell,[50]
A. Menendez-Vazquez,[79] R. A. Mercer,[24] L. Mereni,[132] K. Merfeld,[43] E. L. Merilh,[50] J. D. Merritt,[43] M. Merzougui,[76]
S. Meshkov,[1] C. Messenger,[54] C. Messick,[148] R. Metzdorff,[87] P. M. Meyers,[118] F. Meylahn,[10,11] A. Mhaske,[3] A. Miani,[137,138]
H. Miao,[14] I. Michaloliakos,[33] C. Michel,[132] H. Middleton,[118] L. Milano,[95,5] A. L. Miller,[33,88] M. Millhouse,[118] J. C. Mills,[102]
E. Milotti,[186,27] M. C. Milovich-Goff,[67] O. Minazzoli,[76,187] Y. Minenkov,[36] Ll. M. Mir,[79] A. Mishkin,[33] C. Mishra,[188]
T. Mistry,[131] S. Mitra,[3] V. P. Mitrofanov,[71] G. Mitselmakher,[33] R. Mittleman,[52] G. Mo,[52] K. Mogushi,[70] S. R. P. Mohapatra,[52]
S. R. Mohite,[24] I. Molina,[30] M. Molina-Ruiz,[160] M. Mondin,[67] M. Montani,[74,75] C. J. Moore,[14] D. Moraru,[50] F. Morawski,[64]
G. Moreno,[50] S. Morisaki,[98] B. Mours,[189] C. M. Mow-Lowry,[14] S. Mozzon,[139] F. Muciaccia,[83,37] Arunava Mukherjee,[54]
D. Mukherjee,[85] Soma Mukherjee,[124] Subroto Mukherjee,[63] N. Mukund,[10,11] A. Mullavey,[8] J. Munch,[65] E. A. Muñiz,[44]
P. G. Murray,[54] S. L. Nadji,[10,11] A. Nagar,[190,42,191] I. Nardecchia,[103,36] L. Naticchioni,[37] R. K. Nayak,[192] B. F. Neil,[78]
J. Neilson,[136,81] G. Nelemans,[193] T. J. N. Nelson,[8] M. Nery,[10,11] A. Neunzert,[165] K. Y. Ng,[52] S. Ng,[65] C. Nguyen,[29]
P. Nguyen,[43] T. Nguyen,[52] S. A. Nichols,[2] S. Nissanke,[150,40] F. Nocera,[32] M. Noh,[153] C. North,[102] D. Nothard,[194]

L. K. Nuttall,[139] J. Oberling,[50] B. D. O'Brien,[33] J. O'Dell,[117] G. Oganesyan,[17,18] G. H. Ogin,[195] J. J. Oh,[170] S. H. Oh,[170] F. Ohme,[10,11] H. Ohta,[98] M. A. Okada,[16] C. Olivetto,[32] P. Oppermann,[10,11] R. J. Oram,[8] B. O'Reilly,[8] R. G. Ormiston,[46] N. Ormsby,[7] L. F. Ortega,[33] R. O'Shaughnessy,[133] S. Ossokine,[66] C. Osthelder,[1] D. J. Ottaway,[65] H. Overmier,[8] B. J. Owen,[122] A. E. Pace,[85] G. Pagano,[20,19] M. A. Page,[78] G. Pagliaroli,[17,18] A. Pai,[106] S. A. Pai,[69] J. R. Palamos,[43] O. Palashov,[166] C. Palomba,[37] H. Pan,[107] P. K. Panda,[161] T. H. Pang,[40,156] C. Pankow,[15] F. Pannarale,[83,37] B. C. Pant,[69] F. Paoletti,[19] A. Paoli,[32] A. Paolone,[37,196] W. Parker,[8,185] D. Pascucci,[40] A. Pasqualetti,[32] R. Passaquieti,[20,19] D. Passuello,[19] M. Patel,[7] B. Patricelli,[20,19] E. Payne,[6] T. C. Pechsiri,[33] M. Pedraza,[1] M. Pegoraro,[60] A. Pele,[8] S. Penn,[197] A. Perego,[137,138] C. J. Perez,[50] C. Périgois,[38] A. Perreca,[137,138] S. Perriès,[111] J. Petermann,[129] D. Petterson,[1] H. P. Pfeiffer,[66] K. A. Pham,[46] K. S. Phukon,[40,178,3] O. J. Piccinni,[83,37] M. Pichot,[76] M. Piendibene,[20,19] F. Piergiovanni,[74,75] L. Pierini,[83,37] V. Pierro,[136,81] G. Pillant,[32] F. Pilo,[19] L. Pinard,[132] I. M. Pinto,[136,81,190] K. Piotrzkowski,[88] M. Pirello,[50] M. Pitkin,[198] E. Placidi,[83] W. Plastino,[181,182] C. Pluchar,[116] R. Poggiani,[20,19] E. Polini,[38] D. Y. T. Pong,[105] S. Ponrathnam,[3] P. Popolizio,[32] E. K. Porter,[29] A. Poverman,[61] J. Powell,[199] M. Pracchia,[38] A. K. Prajapati,[63] K. Prasai,[56] R. Prasanna,[161] G. Pratten,[14] T. Prestegard,[24] M. Principe,[136,190,81] G. A. Prodi,[200,138] L. Prokhorov,[14] P. Prosposito,[103,36] A. Puecher,[40,156] M. Punturo,[57] F. Puosi,[19,20] P. Puppo,[37] M. Pürrer,[66] H. Qi,[102] V. Quetschke,[124] P. J. Quinonez,[28] R. Quitzow-James,[70] F. J. Raab,[50] G. Raaijmakers,[150,40] H. Radkins,[50] N. Radulesco,[76] P. Raffai,[127] H. Rafferty,[201] S. X. Rail,[176] S. Raja,[69] C. Rajan,[69] B. Rajbhandari,[122] M. Rakhmanov,[124] K. E. Ramirez,[124] T. D. Ramirez,[30] A. Ramos-Buades,[119] J. Rana,[85] K. Rao,[15] P. Rapagnani,[83,37] U. D. Rapol,[202] B. Ratto,[28] V. Raymond,[102] M. Razzano,[20,19] J. Read,[30] T. Regimbau,[38] L. Rei,[68] S. Reid,[25] D. H. Reitze,[1,33] P. Rettegno,[203,42] F. Ricci,[83,37] C. J. Richardson,[28] J. W. Richardson,[1] L. Richardson,[116] P. M. Ricker,[22] G. Riemenschneider,[203,42] K. Riles,[157] M. Rizzo,[15] N. A. Robertson,[1,54] F. Robinet,[31] A. Rocchi,[36] J. A. Rocha,[30] S. Rodriguez,[30] R. D. Rodriguez-Soto,[28] L. Rolland,[38] J. G. Rollins,[1] V. J. Roma,[43] M. Romanelli,[84] R. Romano,[4,5] C. L. Romel,[50] A. Romero,[79] I. M. Romero-Shaw,[6] J. H. Romie,[8] S. Ronchini,[17,18] C. A. Rose,[24] D. Rose,[30] K. Rose,[194] D. Rosińska,[89] S. G. Rosofsky,[22] M. P. Ross,[180] S. Rowan,[54] S. J. Rowlinson,[14] Santosh Roy,[3] Soumen Roy,[204] P. Ruggi,[32] K. Ryan,[50] S. Sachdev,[85] T. Sadecki,[50] M. Sakellariadou,[114] O. S. Salafia,[49,48,47] L. Salconi,[32] M. Saleem,[34] A. Samajdar,[40,156] E. J. Sanchez,[1] J. H. Sanchez,[30] L. E. Sanchez,[1] N. Sanchis-Gual,[205] J. R. Sanders,[206] K. A. Santiago,[39] E. Santos,[76] T. R. Saravanan,[3] N. Sarin,[6] B. Sassolas,[132] B. S. Sathyaprakash,[85,102] O. Sauter,[38] R. L. Savage,[50] V. Savant,[3] D. Sawant,[106] S. Sayah,[132] D. Schaetzl,[1] P. Schale,[43] M. Scheel,[77] J. Scheuer,[15] A. Schindler-Tyka,[33] P. Schmidt,[14] R. Schnabel,[129] R. M. S. Schofield,[43] A. Schönbeck,[129] E. Schreiber,[10,11] B. W. Schulte,[10,11] B. F. Schutz,[102,10] O. Schwarm,[195] E. Schwartz,[102] J. Scott,[54] S. M. Scott,[9] M. Seglar-Arroyo,[38] E. Seidel,[22] D. Sellers,[8] A. S. Sengupta,[204] N. Sennett,[66] D. Sentenac,[32] V. Sequino,[95,5] A. Sergeev,[166] Y. Setyawati,[10,11] T. Shaffer,[50] M. S. Shahriar,[15] S. Sharifi,[2] A. Sharma,[17,18] P. Sharma,[69] P. Shawhan,[91] H. Shen,[22] M. Shikauchi,[98] R. Shink,[176] D. H. Shoemaker,[52] D. M. Shoemaker,[92] K. Shukla,[160] S. ShyamSundar,[69] M. Sieniawska,[64] D. Sigg,[50] L. P. Singer,[96] D. Singh,[85] N. Singh,[89] A. Singha,[128] A. Singhal,[17,37] A. M. Sintes,[119] V. Sipala,[100,101] V. Skliris,[102] B. J. J. Slagmolen,[9] T. J. Slaven-Blair,[78] J. Smetana,[14] J. R. Smith,[30] R. J. E. Smith,[6] S. N. Somala,[207] E. J. Son,[170] S. Soni,[2] B. Sorazu,[54] V. Sordini,[111] F. Sorrentino,[68] N. Sorrentino,[20,19] R. Soulard,[76] T. Souradeep,[202,3] E. Sowell,[122] A. P. Spencer,[54] M. Spera,[59,60,15] A. K. Srivastava,[63] V. Srivastava,[44] K. Staats,[15] C. Stachie,[76] D. A. Steer,[29] J. Steinhoff,[66] M. Steinke,[10,11] J. Steinlechner,[128,54] S. Steinlechner,[128] D. Steinmeyer,[10,11] G. Stolle-McAllister,[194] D. J. Stops,[14] M. Stover,[194] K. A. Strain,[54] G. Stratta,[208,75] A. Strunk,[50] R. Sturani,[209] A. L. Stuver,[93] S. Südbeck,[129] S. Sudhagar,[3] V. Sudhir,[52] H. G. Suh,[24] T. Z. Summerscales,[210] H. Sun,[78] L. Sun,[1] S. Sunil,[63] A. Sur,[64] J. Suresh,[98] P. J. Sutton,[102] B. L. Swinkels,[40] M. J. Szczepańczyk,[33] M. Tacca,[40] S. C. Tait,[54] C. Talbot,[6] A. J. Tanasijczuk,[88] D. B. Tanner,[33] D. Tao,[1] A. Tapia,[30] E. N. Tapia San Martin,[40] J. D. Tasson,[159] R. Taylor,[1] R. Tenorio,[119] L. Terkowski,[129] M. P. Thirugnanasambandam,[3] L. M. Thomas,[14] M. Thomas,[8] P. Thomas,[50] J. E. Thompson,[102] S. R. Thondapu,[69] K. A. Thorne,[8] E. Thrane,[6] Shubhanshu Tiwari,[82] Srishti Tiwari,[154] V. Tiwari,[102] K. Toland,[54] A. E. Tolley,[139] M. Tonelli,[20,19] Z. Tornasi,[54] A. Torres-Forné,[66] C. I. Torrie,[1] I. Tosta e Melo,[100,101] D. Töyrä,[9] A. T. Tran,[125] A. Trapananti,[184,57] F. Travasso,[57,184] G. Traylor,[8] M. C. Tringali,[89] A. Tripathee,[157] A. Trovato,[29] R. J. Trudeau,[1] D. S. Tsai,[107] K. W. Tsang,[40,211,156] M. Tse,[52] R. Tso,[77] L. Tsukada,[98] D. Tsuna,[98] T. Tsutsui,[98] M. Turconi,[76] A. S. Ubhi,[14] R. P. Udall,[92] K. Ueno,[98] D. Ugolini,[201] C. S. Unnikrishnan,[154] A. L. Urban,[2] S. A. Usman,[109] A. C. Utina,[128] H. Vahlbruch,[10,11] G. Vajente,[1] A. Vajpeyi,[6] G. Valdes,[2] M. Valentini,[137,138] V. Valsan,[24] N. van Bakel,[40] M. van Beuzekom,[40] J. F. J. van den Brand,[172,90,40] C. Van Den Broeck,[156,40] D. C. Vander-Hyde,[44] L. van der Schaaf,[40] J. V. van Heijningen,[78] M. Vardaro,[178,40] A. F. Vargas,[118] V. Varma,[77] S. Vass,[1] M. Vasúth,[55] A. Vecchio,[14] G. Vedovato,[60] J. Veitch,[54] P. J. Veitch,[65] K. Venkateswara,[180] J. Venneberg,[10,11] G. Venugopalan,[1] D. Verkindt,[38] Y. Verma,[69] D. Veske,[35] F. Vetrano,[74] A. Viceré,[74,75]

A. D. Viets,[212] A. Vijaykumar,[21] V. Villa-Ortega,[130] J.-Y. Vinet,[76] S. Vitale,[52] T. Vo,[44] H. Vocca,[58,57] C. Vorvick,[50] S. P. Vyatchanin,[71] A. R. Wade,[9] L. E. Wade,[194] M. Wade,[194] R. M. Wald,[109] R. C. Walet,[40] M. Walker,[7] G. S. Wallace,[25] L. Wallace,[1] S. Walsh,[24] J. Z. Wang,[157] S. Wang,[22] W. H. Wang,[124] Y. F. Wang,[105] R. L. Ward,[9] J. Warner,[50] M. Was,[38] N. Y. Washington,[1] J. Watchi,[120] B. Weaver,[50] L. Wei,[10,11] M. Weinert,[10,11] A. J. Weinstein,[1] R. Weiss,[52] F. Wellmann,[10,11] L. Wen,[78] P. Weßels,[10,11] J. W. Westhouse,[28] K. Wette,[9] J. T. Whelan,[133] D. D. White,[30] L. V. White,[44] B. F. Whiting,[33] C. Whittle,[52] D. M. Wilken,[10,11] D. Williams,[54] M. J. Williams,[54] A. R. Williamson,[139] J. L. Willis,[1] B. Willke,[10,11] D. J. Wilson,[116] M. H. Wimmer,[10,11] W. Winkler,[10,11] C. C. Wipf,[1] G. Woan,[54] J. Woehler,[10,11] J. K. Wofford,[133] I. C. F. Wong,[105] J. Wrangel,[10,11] J. L. Wright,[54] D. S. Wu,[10,11] D. M. Wysocki,[133] L. Xiao,[1] H. Yamamoto,[1] L. Yang,[142] Y. Yang,[33] Z. Yang,[46] M. J. Yap,[9] D. W. Yeeles,[102] A. Yoon,[7] Hang Yu,[77] Haocun Yu,[52] S. H. R. Yuen,[105] A. Zadrożny,[174] M. Zanolin,[28] T. Zelenova,[32] J.-P. Zendri,[60] M. Zevin,[15] J. Zhang,[78] L. Zhang,[1] R. Zhang,[33] T. Zhang,[14] C. Zhao,[78] G. Zhao,[120] M. Zhou,[15] Z. Zhou,[15] X. J. Zhu,[6] A. B. Zimmerman,[148] M. E. Zucker,[1,52] and J. Zweizig[1]

(LIGO Scientific Collaboration and Virgo Collaboration)

[1]*LIGO, California Institute of Technology, Pasadena, California 91125, USA*
[2]*Louisiana State University, Baton Rouge, Louisiana 70803, USA*
[3]*Inter-University Centre for Astronomy and Astrophysics, Pune 411007, India*
[4]*Dipartimento di Farmacia, Università di Salerno, I-84084 Fisciano, Salerno, Italy*
[5]*INFN, Sezione di Napoli, Complesso Universitario di Monte S.Angelo, I-80126 Napoli, Italy*
[6]*OzGrav, School of Physics & Astronomy, Monash University, Clayton 3800, Victoria, Australia*
[7]*Christopher Newport University, Newport News, Virginia 23606, USA*
[8]*LIGO Livingston Observatory, Livingston, Louisiana 70754, USA*
[9]*OzGrav, Australian National University, Canberra, Australian Capital Territory 0200, Australia*
[10]*Max Planck Institute for Gravitational Physics (Albert Einstein Institute), D-30167 Hannover, Germany*
[11]*Leibniz Universität Hannover, D-30167 Hannover, Germany*
[12]*University of Cambridge, Cambridge CB2 1TN, United Kingdom*
[13]*Theoretisch-Physikalisches Institut, Friedrich-Schiller-Universität Jena, D-07743 Jena, Germany*
[14]*University of Birmingham, Birmingham B15 2TT, United Kingdom*
[15]*Center for Interdisciplinary Exploration and Research in Astrophysics (CIERA),*
Northwestern University, Evanston, Illinois 60208, USA
[16]*Instituto Nacional de Pesquisas Espaciais, 12227-010 São José dos Campos, São Paulo, Brazil*
[17]*Gran Sasso Science Institute (GSSI), I-67100 L'Aquila, Italy*
[18]*INFN, Laboratori Nazionali del Gran Sasso, I-67100 Assergi, Italy*
[19]*INFN, Sezione di Pisa, I-56127 Pisa, Italy*
[20]*Università di Pisa, I-56127 Pisa, Italy*
[21]*International Centre for Theoretical Sciences, Tata Institute of Fundamental Research,*
Bengaluru 560089, India
[22]*NCSA, University of Illinois at Urbana-Champaign, Urbana, Illinois 61801, USA*
[23]*Université de Lyon, Université Claude Bernard Lyon 1, CNRS, Institut Lumière Matière,*
F-69622 Villeurbanne, France
[24]*University of Wisconsin-Milwaukee, Milwaukee, Wisconsin 53201, USA*
[25]*SUPA, University of Strathclyde, Glasgow G1 1XQ, United Kingdom*
[26]*Dipartimento di Matematica e Informatica, Università di Udine, I-33100 Udine, Italy*
[27]*INFN, Sezione di Trieste, I-34127 Trieste, Italy*
[28]*Embry-Riddle Aeronautical University, Prescott, Arizona 86301, USA*
[29]*Université de Paris, CNRS, Astroparticule et Cosmologie, F-75013 Paris, France*
[30]*California State University Fullerton, Fullerton, California 92831, USA*
[31]*Université Paris-Saclay, CNRS/IN2P3, IJCLab, 91405 Orsay, France*
[32]*European Gravitational Observatory (EGO), I-56021 Cascina, Pisa, Italy*
[33]*University of Florida, Gainesville, Florida 32611, USA*
[34]*Chennai Mathematical Institute, Chennai 603103, India*
[35]*Columbia University, New York, New York 10027, USA*
[36]*INFN, Sezione di Roma Tor Vergata, I-00133 Roma, Italy*
[37]*INFN, Sezione di Roma, I-00185 Roma, Italy*
[38]*Laboratoire d'Annecy de Physique des Particules (LAPP), Univ. Grenoble Alpes,*
Université Savoie Mont Blanc, CNRS/IN2P3, F-74941 Annecy, France
[39]*Montclair State University, Montclair, New Jersey 07043, USA*

[40]*Nikhef, Science Park 105, 1098 XG Amsterdam, Netherlands*

[41]*Korea Institute of Science and Technology Information, Daejeon 34141, South Korea*

[42]*INFN Sezione di Torino, I-10125 Torino, Italy*

[43]*University of Oregon, Eugene, Oregon 97403, USA*

[44]*Syracuse University, Syracuse, New York 13244, USA*

[45]*Université de Liège, B-4000 Liège, Belgium*

[46]*University of Minnesota, Minneapolis, Minnesota 55455, USA*

[47]*Università degli Studi di Milano-Bicocca, I-20126 Milano, Italy*

[48]*INFN, Sezione di Milano-Bicocca, I-20126 Milano, Italy*

[49]*INAF, Osservatorio Astronomico di Brera sede di Merate, I-23807 Merate, Lecco, Italy*

[50]*LIGO Hanford Observatory, Richland, Washington 99352, USA*

[51]*Institut de Ciències del Cosmos, Universitat de Barcelona, C/Martí i Franquès 1,
Barcelona, 08028, Spain*

[52]*LIGO, Massachusetts Institute of Technology, Cambridge, Massachusetts 02139, USA*

[53]*Dipartimento di Medicina, Chirurgia e Odontoiatria "Scuola Medica Salernitana,"
Università di Salerno, I-84081 Baronissi, Salerno, Italy*

[54]*SUPA, University of Glasgow, Glasgow G12 8QQ, United Kingdom*

[55]*Wigner RCP, RMKI, H-1121 Budapest, Konkoly Thege Miklós út 29-33, Hungary*

[56]*Stanford University, Stanford, California 94305, USA*

[57]*INFN, Sezione di Perugia, I-06123 Perugia, Italy*

[58]*Università di Perugia, I-06123 Perugia, Italy*

[59]*Università di Padova, Dipartimento di Fisica e Astronomia, I-35131 Padova, Italy*

[60]*INFN, Sezione di Padova, I-35131 Padova, Italy*

[61]*Bard College, 30 Campus Rd, Annandale-On-Hudson, New York 12504, USA*

[62]*Montana State University, Bozeman, Montana 59717, USA*

[63]*Institute for Plasma Research, Bhat, Gandhinagar 382428, India*

[64]*Nicolaus Copernicus Astronomical Center, Polish Academy of Sciences, 00-716, Warsaw, Poland*

[65]*OzGrav, University of Adelaide, Adelaide, South Australia 5005, Australia*

[66]*Max Planck Institute for Gravitational Physics (Albert Einstein Institute),
D-14476 Potsdam-Golm, Germany*

[67]*California State University, Los Angeles, 5151 State University Dr, Los Angeles, California 90032, USA*

[68]*INFN, Sezione di Genova, I-16146 Genova, Italy*

[69]*RRCAT, Indore, Madhya Pradesh 452013, India*

[70]*Missouri University of Science and Technology, Rolla, Missouri 65409, USA*

[71]*Faculty of Physics, Lomonosov Moscow State University, Moscow 119991, Russia*

[72]*SUPA, University of the West of Scotland, Paisley PA1 2BE, United Kingdom*

[73]*Bar-Ilan University, Ramat Gan, 5290002, Israel*

[74]*Università degli Studi di Urbino "Carlo Bo", I-61029 Urbino, Italy*

[75]*INFN, Sezione di Firenze, I-50019 Sesto Fiorentino, Firenze, Italy*

[76]*Artemis, Université Côte d'Azur, Observatoire Côte d'Azur, CNRS, F-06304 Nice, France*

[77]*Caltech CaRT, Pasadena, California 91125, USA*

[78]*OzGrav, University of Western Australia, Crawley, Western Australia 6009, Australia*

[79]*Institut de Física d'Altes Energies (IFAE), Barcelona Institute of Science and Technology,
and ICREA, E-08193 Barcelona, Spain*

[80]*Dipartimento di Fisica "E.R. Caianiello," Università di Salerno, I-84084 Fisciano, Salerno, Italy*

[81]*INFN, Sezione di Napoli, Gruppo Collegato di Salerno, Complesso Universitario di Monte S. Angelo,
I-80126 Napoli, Italy*

[82]*Physik-Institut, University of Zurich, Winterthurerstrasse 190, 8057 Zurich, Switzerland*

[83]*Università di Roma "La Sapienza", I-00185 Roma, Italy*

[84]*Univ Rennes, CNRS, Institut FOTON—UMR6082, F-3500 Rennes, France*

[85]*The Pennsylvania State University, University Park, Pennsylvania 16802, USA*

[86]*Indian Institute of Technology Bombay, Mumbai, Maharashtra 400076, India*

[87]*Laboratoire Kastler Brossel, Sorbonne Université, CNRS, ENS-Université PSL, Collège de France,
F-75005 Paris, France*

[88]*Université catholique de Louvain, B-1348 Louvain-la-Neuve, Belgium*

[89]*Astronomical Observatory Warsaw University, 00-478 Warsaw, Poland*

[90]*VU University Amsterdam, 1081 HV Amsterdam, Netherlands*

[91]*University of Maryland, College Park, Maryland 20742, USA*

[92]*School of Physics, Georgia Institute of Technology, Atlanta, Georgia 30332, USA*

[93]*Villanova University, 800 Lancaster Ave, Villanova, Pennsylvania 19085, USA*

[94]*Center for Computational Astrophysics, Flatiron Institute, New York, New York 10010, USA*

[95]*Università di Napoli "Federico II", Complesso Universitario di Monte S.Angelo, I-80126 Napoli, Italy*

[96]*NASA Goddard Space Flight Center, Greenbelt, Maryland 20771, USA*

[97]*Dipartimento di Fisica, Università degli Studi di Genova, I-16146 Genova, Italy*

[98]*RESCEU, University of Tokyo, Tokyo, 113-0033, Japan*

[99]*Tsinghua University, Beijing 100084, China*

[100]*Università degli Studi di Sassari, I-07100 Sassari, Italy*

[101]*INFN, Laboratori Nazionali del Sud, I-95125 Catania, Italy*

[102]*Gravity Exploration Institute, Cardiff University, Cardiff CF24 3AA, United Kingdom*

[103]*Università di Roma Tor Vergata, I-00133 Roma, Italy*

[104]*Departamento de Astronomía y Astrofísica, Universitat de València, E-46100 Burjassot, València, Spain*

[105]*The Chinese University of Hong Kong, Shatin, NT, Hong Kong*

[106]*Indian Institute of Technology Bombay, Powai, Mumbai 400 076, India*

[107]*National Tsing Hua University, Hsinchu City, 30013 Taiwan, Republic of China*

[108]*Charles Sturt University, Wagga Wagga, New South Wales 2678, Australia*

[109]*University of Chicago, Chicago, Illinois 60637, USA*

[110]*Dipartimento di Ingegneria Industriale (DIIN), Università di Salerno, I-84084 Fisciano, Salerno, Italy*

[111]*Institut de Physique des 2 Infinis de Lyon, CNRS/IN2P3, Université de Lyon, Université Claude Bernard Lyon 1, F-69622 Villeurbanne, France*

[112]*Seoul National University, Seoul 08826, South Korea*

[113]*Pusan National University, Busan 46241, South Korea*

[114]*King's College London, University of London, London WC2R 2LS, United Kingdom*

[115]*INAF, Osservatorio Astronomico di Padova, I-35122 Padova, Italy*

[116]*University of Arizona, Tucson, Arizona 85721, USA*

[117]*Rutherford Appleton Laboratory, Didcot OX11 0DE, United Kingdom*

[118]*OzGrav, University of Melbourne, Parkville, Victoria 3010, Australia*

[119]*Universitat de les Illes Balears, IAC3—IEEC, E-07122 Palma de Mallorca, Spain*

[120]*Université Libre de Bruxelles, Brussels 1050, Belgium*

[121]*Departamento de Matemáticas, Universitat de València, E-46100 Burjassot, València, Spain*

[122]*Texas Tech University, Lubbock, Texas 79409, USA*

[123]*University of Rhode Island, Kingston, Rhode Island 02881, USA*

[124]*The University of Texas Rio Grande Valley, Brownsville, Texas 78520, USA*

[125]*Bellevue College, Bellevue, Washington 98007, USA*

[126]*Scuola Normale Superiore, Piazza dei Cavalieri, 7—56126 Pisa, Italy*

[127]*MTA-ELTE Astrophysics Research Group, Institute of Physics, Eötvös University, Budapest 1117, Hungary*

[128]*Maastricht University, 6200 MD, Maastricht, Netherlands*

[129]*Universität Hamburg, D-22761 Hamburg, Germany*

[130]*IGFAE, Campus Sur, Universidade de Santiago de Compostela, 15782 Santiago de Compostela, Galicia, Spain*

[131]*The University of Sheffield, Sheffield S10 2TN, United Kingdom*

[132]*Laboratoire des Matériaux Avancés (LMA), Institut de Physique des 2 Infinis de Lyon, CNRS/IN2P3, Université de Lyon, F-69622 Villeurbanne, France*

[133]*Rochester Institute of Technology, Rochester, New York 14623, USA*

[134]*Dipartimento di Scienze Matematiche, Fisiche e Informatiche, Università di Parma, I-43124 Parma, Italy*

[135]*INFN, Sezione di Milano Bicocca, Gruppo Collegato di Parma, I-43124 Parma, Italy*

[136]*Dipartimento di Ingegneria, Università del Sannio, I-82100 Benevento, Italy*

[137]*Università di Trento, Dipartimento di Fisica, I-38123 Povo, Trento, Italy*

[138]*INFN, Trento Institute for Fundamental Physics and Applications, I-38123 Povo, Trento, Italy*

[139]*University of Portsmouth, Portsmouth PO1 3FX, United Kingdom*

[140]*West Virginia University, Morgantown, West Virginia 26506, USA*

[141]*Stony Brook University, Stony Brook, New York 11794, USA*

[142]*Colorado State University, Fort Collins, Colorado 80523, USA*

[143]*Institute for Nuclear Research, Hungarian Academy of Sciences, Bem t'er 18/c, H-4026 Debrecen, Hungary*

[144]*CNR-SPIN, c/o Università di Salerno, I-84084 Fisciano, Salerno, Italy*

[145]*Scuola di Ingegneria, Università della Basilicata, I-85100 Potenza, Italy*

[146]National Astronomical Observatory of Japan, 2-21-1 Osawa, Mitaka, Tokyo 181-8588, Japan

[147]Observatori Astronòmic, Universitat de València, E-46980 Paterna, València, Spain

[148]Department of Physics, University of Texas, Austin, Texas 78712, USA

[149]University of Szeged, Dóm tér 9, Szeged 6720, Hungary

[150]GRAPPA, Anton Pannekoek Institute for Astronomy and Institute for High-Energy Physics, University of Amsterdam, Science Park 904, 1098 XH Amsterdam, Netherlands

[151]Delta Institute for Theoretical Physics, Science Park 904, 1090 GL Amsterdam, Netherlands

[152]Lorentz Institute, Leiden University, Niels Bohrweg 2, 2333 CA Leiden, Netherlands

[153]University of British Columbia, Vancouver, British Columbia V6T 1Z4, Canada

[154]Tata Institute of Fundamental Research, Mumbai 400005, India

[155]INAF, Osservatorio Astronomico di Capodimonte, I-80131 Napoli, Italy

[156]Department of Physics, Utrecht University, Princetonplein 1, 3584 CC Utrecht, Netherlands

[157]University of Michigan, Ann Arbor, Michigan 48109, USA

[158]American University, Washington, D.C. 20016, USA

[159]Carleton College, Northfield, Minnesota 55057, USA

[160]University of California, Berkeley, California 94720, USA

[161]Directorate of Construction, Services & Estate Management, Mumbai 400094 India

[162]Universiteit Antwerpen, Prinsstraat 13, 2000 Antwerpen, Belgium

[163]University of Bialystok, 15-424 Bialystok, Poland

[164]University of Southampton, Southampton SO17 1BJ, United Kingdom

[165]University of Washington Bothell, Bothell, Washington 98011, USA

[166]Institute of Applied Physics, Nizhny Novgorod, 603950, Russia

[167]Ewha Womans University, Seoul 03760, South Korea

[168]Inje University Gimhae, South Gyeongsang 50834, South Korea

[169]Korea Astronomy and Space Science Institute, Daejeon 34055, South Korea

[170]National Institute for Mathematical Sciences, Daejeon 34047, South Korea

[171]Ulsan National Institute of Science and Technology, Ulsan 44919, South Korea

[172]Maastricht University, P.O. Box 616, 6200 MD Maastricht, Netherlands

[173]Institute of Mathematics, Polish Academy of Sciences, 00656 Warsaw, Poland

[174]National Center for Nuclear Research, 05-400 Świerk-Otwock, Poland

[175]Cornell University, Ithaca, New York 14850, USA

[176]Université de Montréal/Polytechnique, Montreal, Quebec H3T 1J4, Canada

[177]Laboratoire Lagrange, Université Côte d'Azur, Observatoire Côte d'Azur, CNRS, F-06304 Nice, France

[178]Institute for High-Energy Physics, University of Amsterdam, Science Park 904, 1098 XH Amsterdam, Netherlands

[179]NASA Marshall Space Flight Center, Huntsville, Alabama 35811, USA

[180]University of Washington, Seattle, Washington 98195, USA

[181]Dipartimento di Matematica e Fisica, Università degli Studi Roma Tre, I-00146 Roma, Italy

[182]INFN, Sezione di Roma Tre, I-00146 Roma, Italy

[183]ESPCI, CNRS, F-75005 Paris, France

[184]Università di Camerino, Dipartimento di Fisica, I-62032 Camerino, Italy

[185]Southern University and A&M College, Baton Rouge, Louisiana 70813, USA

[186]Dipartimento di Fisica, Università di Trieste, I-34127 Trieste, Italy

[187]Centre Scientifique de Monaco, 8 quai Antoine Ier, MC-98000, Monaco

[188]Indian Institute of Technology Madras, Chennai 600036, India

[189]Institut Pluridisciplinaire Hubert CURIEN, 23 rue du loess—BP28 67037 Strasbourg cedex 2, France

[190]Museo Storico della Fisica e Centro Studi e Ricerche "Enrico Fermi", I-00184 Roma, Italy

[191]Institut des Hautes Etudes Scientifiques, F-91440 Bures-sur-Yvette, France

[192]Indian Institute of Science Education and Research, Kolkata, Mohanpur, West Bengal 741252, India

[193]Department of Astrophysics/IMAPP, Radboud University Nijmegen, P.O. Box 9010, 6500 GL Nijmegen, Netherlands

[194]Kenyon College, Gambier, Ohio 43022, USA

[195]Whitman College, 345 Boyer Avenue, Walla Walla, Washington 99362, USA

[196]Consiglio Nazionale delle Ricerche—Istituto dei Sistemi Complessi, Piazzale Aldo Moro 5, I-00185 Roma, Italy

[197]Hobart and William Smith Colleges, Geneva, New York 14456, USA

[198]Lancaster University, Lancaster LA1 4YW, United Kingdom

[199]OzGrav, Swinburne University of Technology, Hawthorn Victoria 3122, Australia

[200]Università di Trento, Dipartimento di Matematica, I-38123 Povo, Trento, Italy

[201]*Trinity University, San Antonio, Texas 78212, USA*

[202]*Indian Institute of Science Education and Research, Pune, Maharashtra 411008, India*

[203]*Dipartimento di Fisica, Università degli Studi di Torino, I-10125 Torino, Italy*

[204]*Indian Institute of Technology, Palaj, Gandhinagar, Gujarat 382355, India*

[205]*Centro de Astrofísica e Gravitação (CENTRA), Departamento de Física, Instituto Superior Técnico,*
Universidade de Lisboa, 1049-001 Lisboa, Portugal

[206]*Marquette University, 11420 W. Clybourn St., Milwaukee, Wisconsin 53233, USA*

[207]*Indian Institute of Technology Hyderabad, Sangareddy, Khandi, Telangana 502285, India*

[208]*INAF, Osservatorio di Astrofisica e Scienza dello Spazio, I-40129 Bologna, Italy*

[209]*International Institute of Physics, Universidade Federal do Rio Grande do Norte,*
Natal RN 59078-970, Brazil

[210]*Andrews University, Berrien Springs, Michigan 49104, USA*

[211]*Van Swinderen Institute for Particle Physics and Gravity, University of Groningen, Nijenborgh 4, 9747*
AG Groningen, Netherlands

[212]*Concordia University Wisconsin, Mequon, Wisconsin 53097, USA*